Fibrin Networks Infected by Staphylococcal Biofilms:

Mechanics, Structure and Instability

by

Tianhui Ma

A dissertation submitted in partial fulfillment
of the requirements for the degree of
Doctor of Philosophy
(Chemical Engineering)
in the University of Michigan
2018

Doctoral Committee:

Professor Michael J. Solomon, Chair
Professor Chuanwu Xi
Professor Mark A. Burns
Professor Ronald G. Larson
Assistant Professor J. Scott VanEpps

Tianhui M. Ma

tianhui@umich.edu

ORCID iD： 0000-0001-5735-5150

Dedication

To my beloved soul mate Leon Chengwei Zhai
and
my wonderful baby Lucas Qianyu Zhai
who came back to life after resuscitation

Acknowledgement

As I'm completing this awesome experience, I'd like to take time to pen down my gratitude to the people who have supported and encouraged me throughout the duration of my PhD.

First, I would like to thank my advisor, Mike Solomon. It is hard to describe how fortunate and grateful I am to have had the honor to work with Mike. Mike has spent countless hours with me on advice related to research, career and life. As a diligent researcher, he turned my sloppiness into stringency with great patience; as a caring mentor, he offered me great mental support in the most difficult times.

J.Scott VanEpps, my co-advisor, is one of the most energetic and enthusiastic researchers I know. The clinical perspective he brought as an emergency medicine doctor has offered me both excitement and inspirations. His ability to bring in collaborations and his eagerness to try new things has always encouraged me to do the same. He is also a great mentor and a wonderful friend, who shared my highs and helped me through my lows.

I would also like to thank John Younger, who advised me for my first year of PhD. His passion brought me into the wonderland of science. I still remember his words – "try more, worry less", which gives me courage in front of challenges (although sometimes you need to do the opposite

as a researcher). One year might be short, but he has such a great influence on me as he showed me how to live a life with passion, courage and curiosity.

I would like to thank my committee members. Mark Burns, who I admire for his style as a professor and speaker, has been offering great suggestions to my dissertation. Ron Larson, who I first met when taking his fluid mechanics course, has impressed me as an extremely wise and kind man. He has helped me with random questions throughout all my four years here and his questions for me have always helped me clarify the complications in my research. Chuanwu Xi, as a cognate professor from the School of Public Health, has been brought in new perspectives that makes my dissertation complete. I thank for their serves as my committee members.

I would like to thank my collaborators and lab mates. Usha Kadiyala, who shared most of my experience throughout my pursuing of PhD, has become like family and a real soulmate of mine. Words cannot express how grateful I am to be able to meet you here. Carolyn Vitale is pediatrician and a fellow researcher in the VanEpps lab. We have been working together on the Chapter three in my dissertation. She has been offering great ideas and made countless efforts towards the competition of this work. I extend my gratitude to the members of the Solomon lab and the VanEpps lab for their friendship during all my years here. I would also like to thank my Ann Arbor friends with whom I shared laughter and tears. Thank you all for being fun, kind, caring and supportive.

Finally, I would like to thank my family. To my parents and grandparents, thank you for supporting my life decisions and offering help whenever needed. To Leon, my soul mate and

partner of life, thank you for sitting next to me on the flight ten years ago, thank you for loving me, always being with me and making a lifetime memory together with me. To my newborn son, thank you for coming into my life, Lucas! When I was doing experiments early in the mornings and late at nights and there was no one in the building, I had your companion for the whole time. You were so little but you made me so strong. And I didn't forget Tamaki, my cat, who has been bringing so much joy to us. Thank you, Leon, Lucas and Tamaki – my little family. You are the ultimate reason I wake up every morning and everything I do in the rest of the day. I love you.

Table of Contents

List of Figures

Abstract

In this dissertation, we study a new model of medical device infection – that of a fibrin infected with the common blood borne pathogen *Staphylococcus epidermidis,* which is shown to influence fibrin mechanically and structurally on both microscopic and macroscopic scales. *S. epidermidis* present during clot formation produces a visibly disorganized microstructure that increases clot stiffness and triggers mechanical instability over time.

We also noticed that the capacity for *S. epidermidis* to modulate fibrin formation kinetics, mechanics and microstructure is a function of bacterial growth phase. We continued to find that the bacteria-fibrinogen interaction is also growth phase dependent: stationary-phase (biofilm-like) *S. epidermidis* has an increased and stronger adhesion to fibrinogen as compared to exponential-phase (planktonic) ones. Furthermore, the gene expression for SdrG – the protein that adheres *S. epidermidis* cells to fibrinogen was significantly increased in the stationary phase.

We extended our understanding on the effect of *S. epidermidis* on fibrin by investigating a specific protein – *IcaB,* a cell surface-attached protein that has a key role in staphylococcal biofilm formation and immune evasion. It deacetylates and introduces positive charge to polysaccharide intercellular adhesin (PIA) molecules; these charges facilitate adhesion of bacterial cells within a biofilm cluster. Using an *icaB* deletion strain, we evaluated the effects of

PIA deacetylation on staphylococcal interaction with a fibrin network and the resulting structural and mechanical changes to the network. We find that the Δ$icaB$ strain degrades fibrin networks to a higher degree than the wild-type, both structurally and mechanically. Structurally, the connected branches in a fibrin network infected with the Δ$icaB$ strain become disconnected patches. Mechanically, a fibrin network infected with the Δ$icaB$ strain becomes more liquid-like and deformative. Indeed, the Δ$icaB$ produce more *sspA*, a protease that putatively degrades fibrin. We further demonstrate that the Δ$icaB$ cells, which are more diffusive than the wild type cells, co-localize with the fibrin fibers. This co-localization is correlated with fibrin network degradation.

In our study of infected fibrin, we noticed some limitations in the mechanical characterization using rheometers, e.g. the challenge of delivering additives *in situ*. This inspired us to develop a rheometer tooling comprised of a porous hydrogel. The tooling allows additives to be dosed through a rheometer plate or cone, and the consequent effect of these additives on a material's mechanical response measured. We demonstrated that the tooling can be used to study the kinetics of material property variation due to the diffusion of molecular additives into the soft material though the hydrogel plate.

Overall, our understanding of fibrin infected with *S. epidermidis* aids in understanding of medical device infections and infection-induced thromboembolism.

Chapter 1: Introduction

While lives have been improved by indwelling medical devices such as heart valves, endovascular stents, joint prostheses, ventricular assist devices, artificial hearts, etc., they are causing problems at the same time. Indwelling medical devices contribute to 50 to 70% of the nearly two million healthcare-associated infections[1, 2], ranking as the fifth leading cause of death in US acute-care hospitals[3]. Causes for indwelling medical device infections include surgical sterility and abiotic device materials [4 5 6]. While the former has been improving and shown some infection rate decreases [4], research on the latter has failed in many clinical experiments [7] and therefore has not been widely embraced [8].

A surgical wound generated by device implantation allows exposure of the abiotic material to extracellular fluids, bacteria and blood. This then leads to bacterial adhesion and the activation of host immune and coagulation systems [9]. Besides the bio-incompatibility of the device materials, bacteria also activate inflammation, triggering the formation of blood clots which, in turn, promote bacterial adhesion [9]. This bidirectional relationship also contributes to the co-existence of bacteria and host, with the host being mostly blood clots and bacteria stay as biofilms – surface-attached cellular communities encapsulated in matrix materials [10]. Motivated by medical device infections, isolated biofilms have been widely researched with an increasing attention[11]. However, little is know about the co-existence of biofilms and blood clots –the interactions between them and the properties of the complex. Thus, a study of the biofilm-host complex would contribute to the current understanding of indwelling medical device infection.

1.1 Blood Clots and Fibrin

Clots, the result of blood coagulation, are critical to the control of bleeding and the healing of the wound. A clot forms when platelets are activated and the coagulation cascade is triggered by the exposure of collagen and tissue factors to blood [12]. Clots form through fibrinogen (Fg) polymerization into fibrin (Fn) as catalyzed by thrombin [13] [14]. During this process, blood cells and platelets are trapped by fibrin (Fn) fibers in the fibrin network. Fibrin is the fundamental structural component of a clot [15] [16] [17]; it is a primary determinant of clot mechanical properties, stability and strength [18] [19] [20]. Artificial fibrin system has been therefore widely studied to discuss its rheological and microstructural properties [15] [16].

Clot mechanics can be qualitatively characterized by many methods including rheometers [15] [16], light scattering [21], ultrasound [22], etc. For small deformations, a fibrin clot behaves as a nearly perfect elastic gel on the macroscopic scale [16]. One the microscopic scale, microrheology has been applied to study fibrin mechanics [23] [24] [25]. The premise of microrheology is that the motion of a probe particle reflects its local mechanical environment [23] [26] [27]. Techniques include microscopic multiple-particle tracking (MPT), light scattering, magnetic tweezers, etc.[28]. Such research suggests that the macroscopic elasticity of fibrin arise from single fibrin fibers [23], especially their bending motion [25].

The structure of the fibrin network, including its porosity, fiber thickness, and branch point density, determine clot mechanics. Mesh size – the average distance between fibers – is a widely used structural parameter that plays an important role in fibrin mechanics [16]. Confocal scanning laser microscopy (CLSM) is a great tool to study fibrin network structure and characterize fibrin mesh size [16] [23]. CLSM can be used to study the structure at the same time apply microrheology

by MPT with the help of image processing techniques based on the Crocker and Grier algorithm [29]. In addition, electron microscopes can provide clear images of dried fibrin, showing fiber length, diameter, branch point density, etc. [15].

1.2 Staphylococcus epidermidis biofilms

S.epidermidis is a gram-positive, non-motile bacterial strain that dominates the human skin flora [30 31]. It is coagulase-negative; that is, it does not produce coagulase, an enzyme that enables the conversion of fibrinogen to fibrin in blood or plasma by reacting with prothrombin. The selection of a coagulase negative pathogen is parsimonious as it removes the potential confounder of bacterial enzyme-mediated clot formation and focuses solely on the co-localization of bacteria and thrombus. In addition, despite the ubiquitous presence of coagulase negative species such as *S. epidermidis* in bloodstream and medical device infections, prior studies of the interaction between bacteria and fibrin has been more focused on coagulase-positive strains (*e.g.*, *Staphylococcus aureus*) [32 33].

Though harmless to the skin, *S.epidermidis* can be dangerous when it gets into the bloodstream for its primary virulence of forming a biofilm [34]. A biofilm is a bacterial community that occurs when bacteria attach to a surface, alter their phenotype and produce a protective layer of extracellular polymeric substance (EPS). A significant cause of clinical infections, biofilms present a significant obstacle to treatment with traditional antimicrobials and physical shear [30]. The life cycle of a biofilm begins when bacteria adhere to a surface followed by colonization where bacteria multiply rapidly with exponential growth and produce EPS. The densely populated biofilm bacteria slow their growth to a stationary phase. Finally, some bacteria must detach as planktonic bacteria to attach and start a new biofilm colony elsewhere. Each life cycle

stage requires different proteins and mechanisms to be most effective and the bacteria display phenotypic changes as they progress from planktonic to biofilm stages [9] [35]. While the change in phenotype is key in biofilm formation, little attention is paid to the differences in the exponential *versus* stationary growth phase of biofilm formers [35] [36] [37].

The EPS is crucial to the survival of a biofilm: 1) it's important for biofilm formation: the adhesive property of EPS polymers facilitates the tight packing of the biofilm bacteria [38] [39] [40] [41] [42]; 2) it determines the mechanical properties of a biofilm: the polysaccharides in the matrix mediates the reversible and irreversible deformation of a mature biofilm and it resists the premature fragmentation under shear stress [43] [44] [45]; 3) it protects the biofilm from antibiotics by largely reducing the diffusion rate of antibiotics in biofilms [46] [47] [48] and trapping and/or deactivating the antibiotics through interactions[46, 49]. In *S. epidermidis*, the EPS contains polysaccharide intercellular adhesin (PIA) [50, 51], matrix binding proteins[52], accumulation associated proteins, extracellular proteins and nucleic acids[53, 54]. PIA is attracting a great amount of interests for its crucial role in biofilm formation[55], mechanics[56] and persistence *in vivo*[55].

1.3 Bacterial interaction with fibrin

A fibrin network covering a biofilm can be both advantageous and disadvantageous to a biofilm. It reinforces the structure and strength of a biofilm[33] [32] while limiting its growth and preventing it from infecting other places [57]. Coagulase-positive bacteria generate and incorporate fibrin network into their biofilm structure to protect them from the immune evasion and antibiotics [58] [32]. On the other hand, clots generated by the immune system can inhibit pathogen dissemination and survival [57].

Bacterial infection is a significant risk factor for thrombosis and thromboembolism [59, 60 61]. An important virulence factor of many bacterial strains is their ability to develop biofilms, especially on implanted medical devices. Clinically, thrombosis and bacterial biofilms often present simultaneously, especially on implanted medical devices[62,63]. Indeed, Lordick et al. found that 12 of 14 patients with central venous catheter (CVC) related infection had a preceding CVC related venous thrombosis[64]. Also, in patients with recent infection compared with patients without infection, cardioembolic stroke was more frequent (34% versus 19%; $P<0.05$)[61].

1.4 Bacterial gene expression and surface properties

Cell surface properties play an important role in bacterial interaction with fibrin. First of all, under physiological conditions, *S.epidermidis* bacterial cells are negatively charged whereas the clotting agents – fibrinogen, fibrin and thrombin are all positively charged. This coulomb interaction may have an impact on the structure, mechanics and instability of the fibrin network[23].

Second, there are receptors on bacterial cell surfaces. For example, *S.epidermidis* has a gene called *sdrG* (also known as *fbe*) that encodes the production of the well described surface protein SdrG (also known as Fbe which binds fibrinogen in a "lock, dock and latch" mechanism [65 66]. As another example, a gene called *sspA* is involved in the production of glutamyl endopeptidase and serine protease that putatively degrades fibrin [67 30]. Moreover, there could also be other genes that indirectly influence the bacterial interaction with fibrin. For instance, a surface protein IcaB deacetylates and introduces positive charges in the PIA polymer chain and controls whether PIA stays on cell walls [55]. It therefore influences cell surface properties, which may play an important role in cell-fibrin interaction.

1.5 Rheological Measurement during the delivery of a second agent

In the study of the mechanics of fibrin infected by staphylococcal biofilms, rheometry is one of the key techniques for its important role in characterizing the macroscopic mechanical properties of soft matter materials, such as fibrin and biofilms. However, current rheological methods have limited capabilities to study the transient rheology that results from the dosing with molecular additives. Currently, to conduct such measurements, all components must be mixed together *ex situ*. The mixture is then loaded onto the rheometer. In some cases, this process is inadequate. Potential problems include: difficulty in establishing an initial time point for the additive dosing; uncontrolled deformation during the loading of the material – to which the additive performs its function – onto the rheometer; difficulties in mimicking physiological or industrial conditions, etc. For example, to study the mechanics of fibrin formation, fibrinogen and thrombin may need to be loaded onto a cold rheometer plate and the temperature is then increased to body temperature after the preparation[23]. In this case, the temperature effect is ignored in the study. The development of a rheology tooling that could measure mechanics while delivering an addictive to the sample can aid such study: the fibrinogen solution can be loaded first before thrombin is diffused into it. This would better mimic the physiological scenarios.

The feasibility of developing a rheometer tooling that allows diffusion during measurements would not only benefit the above example, but a lot more of both scientific and technological research. In biological systems, for example, there is interest in studying the transient rheology of blood clot fibrinolysis as plasmin diffuses into and dissolves clots [68] and the interactions between blood clots and continuously growing bacterial biofilms[69]. There is also interest in studying the transient rheology of colloidal suspensions during gelation [70]. Industrial examples

where transient measurements are important include the addition of thickeners, gelling agents, and emulsifiers to food products [71], the use of reactive polymeric materials as rheology modifiers of lubricating greases in the oil industry [72], and the control over ionic strength in micelle solutions to change the flow properties in consumer products [73].

1.6 Research goals and organization of the dissertation

The overarching goal of this dissertation is to investigate the bacterial interaction with a fibrin network and determine the impact of bacteria on fibrin mechanics, structure and instability. The studies include two limits of a spectrum of possibilities: In one limit, the role of bacterial cell growth is minimized by direct introduction of the physiologically relevant concentration of bacterial cells and then study of the effect of these cells on fibrin network formation. In the second limit, the role of fibrin network formation kinetics is minimized by pre-assembly of a fibrin network in which bacterial cells are then introduced and allowed to proliferate. Experimental models are built to mimic these two scenarios as shown in Figure 1-1. The molecular mechanisms are also explored to aid in the understanding of the characterized phenomena. Overall, this study will contribute to the current understanding of medical device contaminations and motivate relevant future *in vivo* and clinical studies.

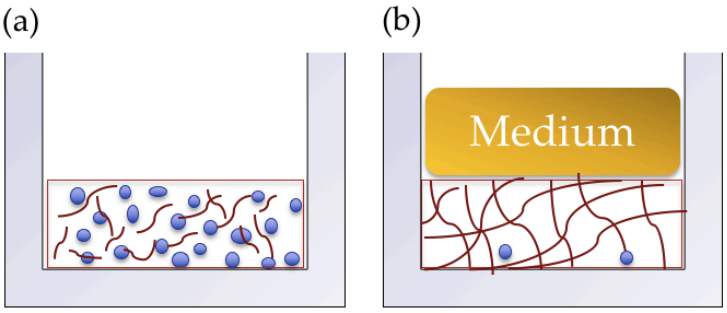

Figure 1-1 | Sketches of experimental models of the two limits of a spectrum of possibilities.

A sketch of (a) fibrin formation at fixed bacterial concentration and (b) pre-assembled fibrin network with proliferating bacterial biofilms inside a confocal microscope coverslip well. Red lines indicate fibrin oligomers, blue circles indicate bacteria, orange rectangle indicates a volume of bacteria culturing medium.

In Chapter 2, we built an *in vitro* new model for medical device infection – that of a fibrin clot infected with the common blood borne pathogen *Staphylococcus epidermidis*. To do this, we directly introduced the physiologically relevant concentration of bacterial cells to a forming fibrin clot with the role of bacterial growth minimized as indicated in Figure 1-1(a). We characterized the infected fibrin's formation kinetics, mechanics, structure and instability on both the macroscopic and microscopic scale. We applied rheology and photography to study the behaviors on the macroscopic scale and confocal laser scanning microscopy (CLSM), image analysis, particle tracking and microrheology to study the microscopic phenomena.

In Chapter 3, we explained potential mechanisms that leads to the phenomena noticed in Chapter 2 on a molecular level. We hypothesized that stationary-phase (biofilm-like) *S. epidermidis* will have a more robust effect on clot kinetics and elasticity than exponential-phase (planktonic) ones. Rheology and confocal microscopy is used to evaluate the difference in the mechanics and structure, respectively, of the fibrin network infected by the exponential and stationary phase *S. epidermidis*. We then evaluated the capacity for *S. epidermidis* to bind to fibrinogen as a function of its growth phase. We first tested the relevant gene expressions, especially for SdrG – the protein that adheres *S.epidermidis* cells. A functional *in vitro* model was developed to evaluate adhesion of *S. epidermidis* to a fibrinogen coated surface in a continuously flowing environment. The bacterial deposition rate onto fibrinogen and the residence time are characterized. Flow cytometry is also applied to determine the amount of

fibrinogen molecules attracted to cell walls. We correlated the growth-dependent SdrG expressions and fibrinogen-binding capacities to the growth-dependent effects on fibrin network to offer a potential explanation of the noticed phenomena in Chapter 2.

In Chapter 4, we pre-assembly of a fibrin network in which bacterial cells are then introduced and allowed to proliferate to study the scenario where a very small amount of bacteria grow inside an established fibrin network with the effect of the kinetics of the fibrin formation minimized as indicated in Figure 1-1 (b). With this model, we investigated the effect of IcaB, or, the role of the deacetylation and the introduction of positive charges to PIA molecules, on the bacterial interaction with fibrin. We first characterized structural and mechanical changes of the infected fibrin networks during the bacterial proliferation using confocal microscopy and microrheology. We then correlated the characterized phenomena with cell location relative to fibrin, cell mobility, cell surface charges and *sspA* expression by applying image processing, particle tracking zeta potential measurements, RNA extraction and reverse transcription polymerase chain reaction (RT-PCR), respectively.

In Chapter 5, we developed rheometer tooling comprised of a porous hydrogel that allows us to dose solvents and other additives to materials as their mechanical response is measured. We synthesized a disposable hydrogel rheometer plate through photopolymerization of an aqueous polyethylene glycol (PEG) diacrylate solution. We controlled the precision of the tooling by fixing the mold to a five-axis optomechanical stage. We demonstrated the performance of the tooling by measuring viscoelastic properties of aqueous polyethylene oxide (PEO) solutions and comparing the values to those obtained using standard fixtures. We further offered examples of

self-assembled and gel soft matter that demonstrate that the tooling can be used to study the kinetics of material property variation due to the diffusion of molecular additives though the hydrogel plate.

Finally, we discuss the overall conclusions and future work that could be investigated as a result of the body of work included in this dissertation.

1.7 References

1. Darouiche RO. Treatment of infections associated with surgical implants. *New England Journal of Medicine* **350**, 1422-1429 (2004).

2. Bryers JD. Medical biofilms. *Biotechnology and bioengineering* **100**, 1-18 (2008).

3. Klevens RM*, et al.* Estimating health care-associated infections and deaths in US hospitals, 2002. *Public health reports* **122**, 160-166 (2007).

4. Control CfD, Prevention. Reduction in central line-associated bloodstream infections among patients in intensive care units--Pennsylvania, April 2001-March 2005. *MMWR Morbidity and mortality weekly report* **54**, 1013 (2005).

5. Cox EG*, et al.* A randomized, controlled trial of catheter-related infectious event rates using antibiotic-impregnated catheters versus conventional catheters in pediatric cardiovascular surgery patients. *Journal of the Pediatric Infectious Diseases Society* **2**, 67-70 (2012).

6. Weber JM, Sheridan RL, Fagan S, Ryan CM, Pasternack MS, Tompkins RG. Incidence of catheter-associated bloodstream infection after introduction of minocycline and rifampin antimicrobial-coated catheters in a pediatric burn population. *Journal of Burn Care & Research* **33**, 539-543 (2012).

7. Malani PN. *Device Associated Infections, An Issue of Infectious Disease Clinics-E-Book*. Elsevier Health Sciences (2012).

8. Darouiche RO. Antimicrobial-modified vascular catheters. In: *Biomaterials Associated Infection* (ed^(eds). Springer (2013).

9. VanEpps JS, Younger JG. Implantable Device-Related Infection. *Shock (Augusta, Ga)* **46**, 597-608 (2016).

10. Hall-Stoodley L, Costerton JW, Stoodley P. Bacterial biofilms: from the natural environment to infectious diseases. *Nature reviews microbiology* **2**, 95 (2004).

11. Costerton JW, Stewart PS, Greenberg EP. Bacterial biofilms: a common cause of persistent infections. *Science (New York, NY)* **284**, 1318-1322 (1999).

12. Furie B, Furie BC. Mechanisms of thrombus formation. *New England Journal of Medicine* **359**, 938-949 (2008).

13. Evans P, Hawkins K, Williams P. Rheometry for blood coagulation studies. *Rheology Reviews* **2006**, 255 (2006).

14. Blombäck B. Fibrinogen and fibrin-proteins with complex roles in hemostasis and thrombosis. *Thrombosis research* **83**, 1-75 (1996).

15. Ryan EA, Mockros LF, Weisel JW, Lorand L. Structural origins of fibrin clot rheology. *Biophysical journal* **77**, 2813-2826 (1999).

16. Piechocka IK, Bacabac RG, Potters M, MacKintosh FC, Koenderink GH. Structural hierarchy governs fibrin gel mechanics. *Biophysical journal* **98**, 2281-2289 (2010).

17. Jansen KA, Bacabac RG, Piechocka IK, Koenderink GH. Cells actively stiffen fibrin networks by generating contractile stress. *Biophysical journal* **105**, 2240-2251 (2013).

18. Bridge KI, Philippou H, Ariëns RA. Clot properties and cardiovascular disease. *Thrombosis and haemostasis* **111**, 901-908 (2014).

19. Janmey PA, Winer JP, Weisel JW. Fibrin gels and their clinical and bioengineering applications. *Journal of the Royal Society Interface* **6**, 1-10 (2009).

20. Falvo MR, Gorkun OV, Lord ST. The molecular origins of the mechanical properties of fibrin. *Biophysical chemistry* **152**, 15-20 (2010).

21. Tripathi MM, Hajjarian Z, Van Cott EM, Nadkarni SK. Assessing blood coagulation status with laser speckle rheology. *Biomedical optics express* **5**, 817-831 (2014).

22. Huang C-C, Lin Y-H, Liu T-Y, Lee P-Y, Wang S-H. Study of the blood coagulation by ultrasound. *J Med Biol Eng* **31**, 79-86 (2011).

23. Ma TM, VanEpps JS, Solomon MJ. Structure, Mechanics, and Instability of Fibrin Clot Infected with Staphylococcus epidermidis. *Biophysical journal* **113**, 2100-2109 (2017).

24. Valentine M*, et al.* Colloid surface chemistry critically affects multiple particle tracking measurements of biomaterials. *Biophysical journal* **86**, 4004-4014 (2004).

25. Roska FJ, Ferry JD. Studies of fibrin film. I. Stress relaxation and birefringence. *Biopolymers* **21**, 1811-1832 (1982).

26. Fitzgerald JR, Foster TJ, Cox D. The interaction of bacterial pathogens with platelets. *Nature Reviews Microbiology* **4**, 445 (2006).

27. Xu L-C, Siedlecki CA. Effects of plasma proteins on Staphylococcus epidermidis RP62A adhesion and interaction with platelets on polyurethane biomaterial surfaces. *Journal of Biomaterials and Nanobiotechnology* **3**, 487 (2012).

28. Cicuta P, Donald AM. Microrheology: a review of the method and applications. *Soft Matter* **3**, 1449-1455 (2007).

29. Crocker JC, Grier DG. Methods of digital video microscopy for colloidal studies. *Journal of colloid and interface science* **179**, 298-310 (1996).

30. Otto M. Staphylococcus epidermidis--the 'accidental' pathogen. *Nat Rev Microbiol* **7**, 555-567 (2009).

31. Ziebuhr W, Hennig S, Eckart M, Kränzler H, Batzilla C, Kozitskaya S. Nosocomial infections by Staphylococcus epidermidis: how a commensal bacterium turns into a pathogen. *International journal of antimicrobial agents* **28**, 14-20 (2006).

32. Prasad JM*, et al.* Mice expressing a mutant form of fibrinogen that cannot support fibrin formation exhibit compromised antimicrobial host defense. *Blood* **126**, 2047-2058 (2015).

33. Loof TG*, et al.* Staphylococcus aureus-induced clotting of plasma is an immune evasion mechanism for persistence within the fibrin network. *Microbiology* **161**, 621-627 (2015).

34. Fey PD, Olson ME. Current concepts in biofilm formation of Staphylococcus epidermidis. *Future microbiology* **5**, 917-933 (2010).

35. Watnick P, Kolter R. Biofilm, city of microbes. *Journal of Bacteriology* **182**, 2675-2679 (2000).

36. Parsek MR, Fuqua C. Biofilms 2003: emerging themes and challenges in studies of surface-associated microbial life. *Journal of Bacteriology* **186**, 4427-4440 (2004).

37. Webb JS, Givskov M, Kjelleberg S. Bacterial biofilms: prokaryotic adventures in multicellularity. *Current opinion in microbiology* **6**, 578-585 (2003).

38. Sutherland IW. Biofilm exopolysaccharides: a strong and sticky framework. *Microbiology* **147**, 3-9 (2001).

39. Cogan N, Keener JP. The role of the biofilm matrix in structural development. *Mathematical medicine and biology: a journal of the IMA* **21**, 147-166 (2004).

40. Flemming H-C. The perfect slime. *Colloids and Surfaces B: Biointerfaces* **86**, 251-259 (2011).

41. Vilain S, Pretorius JM, Theron J, Brözel VS. DNA as an adhesin: Bacillus cereus requires extracellular DNA to form biofilms. *Applied and environmental microbiology* **75**, 2861-2868 (2009).

42. Das T, Sharma PK, Busscher HJ, van der Mei HC, Krom BP. Role of extracellular DNA in initial bacterial adhesion and surface aggregation. *Applied and environmental microbiology* **76**, 3405-3408 (2010).

43. Peterson BW, Busscher HJ, Sharma PK, Van Der Mei HC. Visualization of microbiological processes underlying stress relaxation in Pseudomonas aeruginosa biofilms. *Microscopy and Microanalysis* **20**, 912-915 (2014).

44. He Y*, et al.* Stress relaxation analysis facilitates a quantitative approach towards antimicrobial penetration into biofilms. *PLoS One* **8**, e63750 (2013).

45. Klapper I, Rupp CJ, Cargo R, Purvedorj B, Stoodley P. Viscoelastic fluid description of bacterial biofilm material properties. *Biotechnology and Bioengineering* **80**, 289-296 (2002).

46. Hall- Stoodley L, Stoodley P. Evolving concepts in biofilm infections. *Cellular microbiology* **11**, 1034-1043 (2009).

47. Doroshenko N*, et al.* Extracellular DNA impedes the transport of vancomycin in Staphylococcus epidermidis biofilms preexposed to subinhibitory concentrations of vancomycin. *Antimicrobial agents and chemotherapy* **58**, 7273-7282 (2014).

48. Rani SA, Pitts B, Stewart PS. Rapid diffusion of fluorescent tracers into Staphylococcus epidermidis biofilms visualized by time lapse microscopy. *Antimicrobial agents and chemotherapy* **49**, 728-732 (2005).

49. Bagge N, Hentzer M, Andersen JB, Ciofu O, Givskov M, Høiby N. Dynamics and spatial distribution of β-lactamase expression in Pseudomonas aeruginosa biofilms. *Antimicrobial agents and chemotherapy* **48**, 1168-1174 (2004).

50. Otto M. Molecular basis of Staphylococcus epidermidis infections. In: *Seminars in immunopathology* (ed^(eds). Springer (2012).

51. Rohde H, Frankenberger S, Zähringer U, Mack D. Structure, function and contribution of polysaccharide intercellular adhesin (PIA) to Staphylococcus epidermidis biofilm formation and pathogenesis of biomaterial-associated infections. *European journal of cell biology* **89**, 103-111 (2010).

52. Christner M*, et al.* The giant extracellular matrix- binding protein of Staphylococcus epidermidis mediates biofilm accumulation and attachment to fibronectin. *Molecular microbiology* **75**, 187-207 (2010).

53. Qin Z*, et al.* Role of autolysin-mediated DNA release in biofilm formation of Staphylococcus epidermidis. *Microbiology* **153**, 2083-2092 (2007).

54. Hussain M, Herrmann M, von Eiff C, Perdreau-Remington F, Peters G. A 140-kilodalton extracellular protein is essential for the accumulation of Staphylococcus epidermidis strains on surfaces. *Infection and immunity* **65**, 519-524 (1997).

55. Vuong C*, et al.* A crucial role for exopolysaccharide modification in bacterial biofilm formation, immune evasion, and virulence. *Journal of Biological Chemistry* **279**, 54881-54886 (2004).

56. Stewart EJ, Ganesan M, Younger JG, Solomon MJ. Artificial biofilms establish the role of matrix interactions in staphylococcal biofilm assembly and disassembly. *Sci Rep* **5**, 13081 (2015).

57. Engelmann B, Massberg S. Thrombosis as an intravascular effector of innate immunity. *Nature Reviews Immunology* **13**, 34 (2013).

58. Kwiecinski J*, et al.* Staphylokinase control of Staphylococcus aureus biofilm formation and detachment through host plasminogen activation. *The Journal of infectious diseases* **213**, 139-148 (2015).

59. Samama MM. An epidemiologic study of risk factors for deep vein thrombosis in medical outpatients: the Sirius study. *Archives of internal medicine* **160**, 3415-3420 (2000).

60. Dalager-Pedersen M, Sogaard M, Schonheyder HC, Thomsen RW, Baron JA, Nielsen H. Venous thromboembolism after community-acquired bacteraemia: a 20-year danish cohort study. *PLoS One* **9**, e86094 (2014).

61. Grau AJ*, et al.* Clinical and biochemical analysis in infection-associated stroke. *Stroke; a journal of cerebral circulation* **26**, 1520-1526 (1995).

62. Raad, II, Luna M, Khalil SA, Costerton JW, Lam C, Bodey GP. The relationship between the thrombotic and infectious complications of central venous catheters. *Jama* **271**, 1014-1016 (1994).

63. Brackman G, De Meyer L, Nelis HJ, Coenye T. Biofilm inhibitory and eradicating activity of wound care products against Staphylococcus aureus and Staphylococcus epidermidis biofilms in an in vitro chronic wound model. *Journal of applied microbiology* **114**, 1833-1842 (2013).

64. Lordick F*, et al.* Ultrasound screening for internal jugular vein thrombosis aids the detection of central venous catheter-related infections in patients with haemato-oncological diseases: a prospective observational study. *British journal of haematology* **120**, 1073-1078 (2003).

65. Davis SL, Gurusiddappa S, McCrea KW, Perkins S, Höök M. SdrG, a fibrinogen-binding bacterial adhesin of the microbial surface components recognizing adhesive matrix molecules subfamily from Staphylococcus epidermidis, targets the thrombin cleavage site in the Bβ chain. *Journal of Biological Chemistry* **276**, 27799-27805 (2001).

66. Nilsson M, Frykberg L, Flock J-I, Pei L, Lindberg M, Guss B. A fibrinogen-binding protein ofStaphylococcus epidermidis. *Infection and immunity* **66**, 2666-2673 (1998).

67. Nickerson NN, Prasad L, Jacob L, Delbaere LT, McGavin MJ. Activation of the SspA serine protease zymogen of Staphylococcus aureus proceeds through unique variations of a trypsinogen-like mechanism and is dependent on both autocatalytic and metalloprotease-specific processing. *Journal of Biological Chemistry* **282**, 34129-34138 (2007).

68. Kane KK. Fibrinolysis--a review. *Annals of clinical and laboratory science* **14**, 443-449 (1984).

69. Ma TM, VanEpps JS, Solomon MJ. Structure, Mechanics, and Instability of Fibrin Clot Infected with Staphylococcus epidermidis. *Biophysical Journal* **113**, 2100-2109.

70. Zaccarelli E. Colloidal gels: equilibrium and non-equilibrium routes. *Journal of Physics: Condensed Matter* **19**, 323101 (2007).

71. Savage R. Effects of rheology modifiers on the flow curves of idealised and food suspensions. *Food Hydrocolloids* **14**, 209-215 (2000).

72. Moreno G, Valencia C, de Paz MV, Franco JM, Gallegos C. Use of Reactive Diisocyanate-Terminated Polymers as Rheology Modifiers of Lubricating Greases. *Industrial & Engineering Chemistry Research* **45**, 4001-4010 (2006).

73. Adams AA, Solomon MJ, Larson RG, Xia X. Concentration, salt and temperature dependence of strain hardening of step shear in CTAB/NaSal surfactant solutions. *Journal of Rheology* **61**, 967-977 (2017).

Chapter 2: Structure, mechanics, and instability of fibrin clot infected with *Staphylococcus epidermidis*[1]

2.1 Abstract

Health care associated infection, over half of which can be attributed to indwelling medical devices, is a strong risk factor for thromboembolism. Although most experimental models of medical device infection draw upon isolated bacterial biofilms, in fact there is no infection without host protein contribution. Here we study a new model for medical device infection – that of an infected fibrin clot – and show that the common blood borne pathogen *Staphylococcus epidermidis* influences this *in vitro* model of a blood clot mechanically and structurally on both microscopic and macroscopic scales. Bacteria present during clot formation produce a visibly disorganized microstructure that increases clot stiffness and triggers mechanical instability over time. Our results provide insight into the observed correlation between medical device infection and thromboembolism; the increase in model clot heterogeneity shows that *S. epidermidis* can rupture a fibrin clot. The resultant embolization of the infected clot can contribute to the systemic dissemination of the pathogen.

[1] The work of Chapter 2 is published as "Structure, mechanics, and instability of fibrin clot infected with *Staphylococcus epidermidis"* by **Tianhui Ma**, J. Scott VanEpps, and Michael Solomon. Biophysical Journal (2017)

2.2 Introduction:

Clotting, the result of blood coagulation, is critical to hemostasis (*i.e.*, the control of bleeding). Clots normally appear at a site of injury to prevent bleeding, restore barrier function, and promote wound healing. However, abnormal clot conditions (*i.e.*, thrombosis) can lead to disease. For example, if a thrombus embolizes, it can circulate and block downstream arteries in the lung (pulmonary embolism) or brain (stroke)[1,2].

Bacterial infection is a significant risk factor for thromboembolism[3,4 5]. An important virulence factor of many bacterial strains is their ability to develop biofilms, especially on implanted medical devices. Biofilms are bacterial communities embedded in a protective extracellular polymeric substance comprised of polysaccharide, proteins, and DNA[6]. Clinically, thrombosis and bacterial biofilms often present simultaneously, especially on implanted medical devices[7,8]. Indeed, Lordick et al. found that 12 of 14 patients with central venous catheter (CVC) related infection had a preceding CVC related venous thrombosis[9].

Most experimental models of bacterial biofilm infection on implanted medical devices utilize isolated, single-species bacterial biofilms generated on a variety of biomaterials[10 11]. However, bacterial contamination of medical devices involves the co-localization of bacteria as biofilms and host proteins as clot. For example, implanted abiotic materials provide a niche for attachment and development of bacterial biofilms while also activating host inflammatory and coagulation cascades which lead to fibrin clots[12]. In this paper, we develop an experimental model of medical device infection that combines biofilm-forming bacteria and host clot. The *in vitro* model of clot in this report is a fibrin network, as polymerized by thrombin. Fibrin is the

fundamental structural component of a clot[13,14,15]; it is the primary determinant of clot mechanical properties, stability, and strength[16].

To research infected clots, two limits of a spectrum of possibilities are available for study design. In one limit, the role of bacterial cell growth is minimized by direct introduction of the physiologically relevant concentration of bacterial cells and then study of the effect of these cells on fibrin network formation. In the second limit, the role of fibrin network formation kinetics is minimized by pre-assembly of a fibrin network in which bacterial cells are then introduced and allowed to proliferate. Realistically, infected clots fall within these two limits. In the present work, we have selected the former study design, because it produces direct information about bacterial-fibrin interactions, albeit with the understanding that both limits are of research interest.

We therefore introduce *Staphylococcus epidermidis* cells during the thrombin-induced polymerization of fibrinogen to mimic host clot forming on device surfaces in the presence of this pathogen. *S.epidermidis* is an innocuous commensal microorganism on human skin but can be pathogenic once introduced to the bloodstream or colonized on implanted devices[17]. Specifically, it is the leading cause of indwelling medical device contaminations/infection[18] and is commonly associated with infective thrombosis[19]. It is coagulase-negative; that is, it does not produce coagulase, an enzyme that enables the conversion of fibrinogen to fibrin in blood or plasma by reacting with prothrombin. The selection of a coagulase negative pathogen is parsimonious as it removes the potential confounder of bacterial enzyme-mediated clot formation and focuses solely on the co-localization of bacteria and thrombus. In addition, despite the ubiquitous presence of coagulase negative species such as *S. epidermidis* in

bloodstream and medical device infections, prior studies of the interaction between bacteria and fibrin has been more focused on coagulase-positive strains (*e.g.*, *Staphylococcus aureus*)[20,21]. The bacterial concentrations applied in this study are similar to the biofilm cell density found in a rabbit model of central venous catheter infection[22].

In this work the structure, mechanics, and instability of the infected clot is compared to cell-free clot. The structure of the fibrin network is characterized by its fiber thickness and mesh size, the latter being the average distance between neighboring strands of fibers. These structural properties determine clot mechanical properties that are critical to both normal function and pathology[15]. Clinically, clot elasticity – that is, clot stiffness – is measured to diagnose hemostatic defects, such as abnormalities in clot formation/dissolution kinetics and clot strength[23,]. Moreover, clot instability – that is, propensity for rupture and embolization – and the effectiveness of medical treatments are a function of clot mechanics. The viscoelastic properties of a thrombus determine whether blood flow causes deformation, rupture, or embolization of the clot[24,15,25].

In this study we first use rheometry to show the mechanical influence of *S. epidermidis* on fibrin clot formation and its elasticity. Second, using confocal microscopy, we evaluate changes in the microstructure of fibrin clots after the addition of *S. epidermidis* cells. Third, we connect the changes in infected clot elasticity to the changes in fibrin network structure using multiple particle tracking (MPT) microrheology. Fourth, through microscopic image analysis, we describe the time variation of fibrin filament area, bacteria-fibrin overlap, and network mesh size in an

infected fibrin clot. Finally, by combining microscopy and time-lapse photography, we show mesoscopic and macroscopic instability of the infected clot structure at long times.

2.3 Materials and Methods

2.3.1 Bacterial strain and culture conditions.

S.epidermidis RP62A, a biofilm-forming strain was obtained from American Type Culture Collection (ATCC 35984). One colony from a Lysogeny broth (LB) plate was inoculated in a flask (125 ml) containing 32 ml tryptic soy broth with 1 wt. % glucose (TSB_G) and cultured at 37 ℃ at 200 rpm of continuous shaking for approximately nine hours to an optical density at 600nm (OD_{600}) = 1.35±0.1.

2.3.2 Fibrin Clot and Infected Fibrin Clot Constitution.

Citrate-free thrombin from human plasma (605206-100U) and fibrinogen (Fg) from human plasma (341576-100MG) were purchased from EMD Millipore Corporation (Billerica, MA, USA). Fibrinogen solutions were made by diluting the stock solution with Hank's Balanced Salt Solution (HBSS) (1X) (with Calcium, Magnesium, no phenol red, 1g/L D-Glucose, Thermo Fisher Scientific, Waltham, MA, USA) at 37℃.

After reaching the prescribed OD_{600}, the bacterial suspension was allowed to stand quiescently at room temperature for one hour so large cell clusters could sediment. A INCYTO™ C-Chip™ Disposable Hemacytometer (Thermo Fisher Scientific, Waltham, MA, USA) was used to determine the cell concentration. A target number of cells were re-suspended in the Fg solution so as to achieve the desired final cell concentration. The introduced cell concentrations for bulk

rheology measurements were 1×10^9cells/ml, 2×10^9cells/ml, 4×10^9cells/ml and 6×10^9cells/ml. These values are similar to the 10^5 CFU/cm^2 cell density found in a rabbit model of central venous catheter infection[22]. A cell concentration of 4×10^9cells/ml was used for the remaining experiments. Specifically, a volume of the bacterial culture was centrifuged (15000g, 40s) and washed twice with HBSS; the resulting bacterial pellet was suspended in Fg solution. The Fg solution or the cell-Fg mixture was kept on ice for 3 minutes before clot initiation by adding thrombin (0.5U/ml as final concentration). Then the samples were loaded to either the rheometer (5°C) or to a Nunc™ Lab-Tek™ II Chambered Coverglass dish (Thermo Scientific, USA) (kept on ice). The rheometer temperature was increased to 37°C after loading and the chambered coverglass was held in a 37°C incubator. The chamber coverglass was sealed with parafilm to prevent desiccation. The effect of cold fibrin initiation is discussed in Figure 2-1.

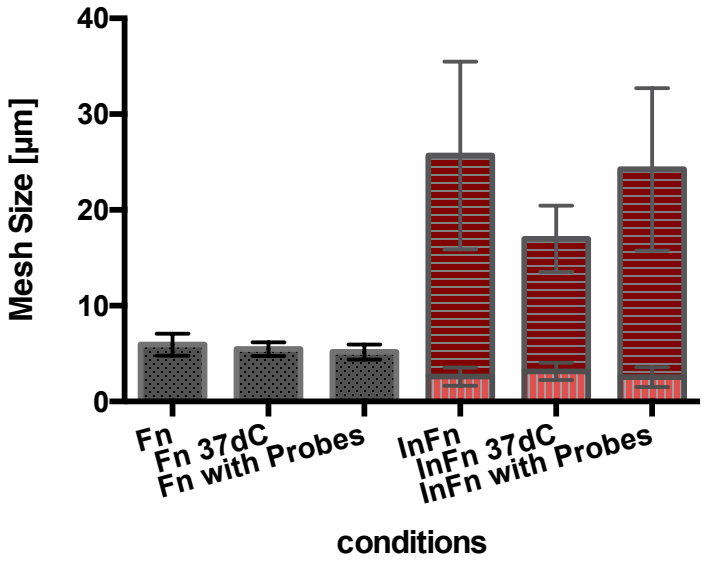

Figure 2-1 | Influence of initial temperature and probes on fibrin structures

Mesh size characterization of pure fibrin and infected fibrin clot under different conditions. Error bars denote standard deviations of all the stacks in n = 3. The "37dC" protocol is the following: The fibrinogen (Fg) solution, the cell-Fg mixture and the chamber coverglass dishes were kept in a 37°C dry bath incubator for temperature to reach 37°C. Solutions were loaded to the chamber

coverglass dishes and 0.5U/ml thrombin (final concentration) was added to initiate the polymerization. Chamber coverglass dishes were kept in a 37℃ incubator afterwards.

2.3.3 Clot Elasticity

Clot elasticity was characterized by measuring the linear elastic modulus, G', on a mechanical rheometer (TA Instruments AR-G2, cone and plate fixture with a 2° cone angle and a 40 mm diameter). All tests were performed at a frequency $\omega = 0.1$ Hz under an imposed strain $\gamma = 0.01$ at 37℃ in a humid atmosphere. Clot desiccation was further prevented by coating the sample edge with a thin layer of mineral oil[14]. Loading the sample in the rheometer at 5°C delayed clotting until the instrument was prepared for measurement. After loading, the rheometer reached 37℃ in about one minute; measurements were initiated 30 s later. Experiments were stopped after steady-state was reached, defined as the variability in G' in any 2 min interval being no more than 0.5% for 20 minutes. The steady-state elastic modulus was taken as the average of all the data within the steady-state region with error bars denoting standard deviation of all replicates.

2.3.4 Microstructure visualization and multiple particle tracking.

Image volumes (3D) and time series (2D) of fibrin and bacterial cell microstructure were acquired using a Nikon A1Rsi confocal laser scanning microscope with a 100x, 1.45 NA, oil immersion objective. Specimens were prepared in a Nunc™ Lab-Tek™ II Chambered Coverglass dish. Image volumes for microstructure visualization and analysis were obtained by axially scanning from the coverslip to 50 μm above the coverslip in increments of 1 μm. The image size was 127.45×127.45 μm^2 (at either 512×512 pixel or 1019×1019 pixel resolution). For multiple-particle tracking, two-dimensional time series of 900 images with size 42.48×42.48μm^2

(512×512pixels) were collected at 15 frames per second at a distance of 20±5μm above coverslip. Both z-stacks and time series were captured randomly with in the specimen dish. Images projections of corresponding height and renderings of 3D volumes were made in ImageJ (http://rsbweb.nih. gov/ij/).

Stains used were Alexa Fluor 647 (650/668nm) or Alexa Fluor 546 (~558/573 nm) conjugate human Fg (Thermo Fisher Scientific, Waltham, MA, USA), which was mixed with unlabeled fibrinogen in a molar ratio of 1:4 in HBSS. The non-fluorescent Fg concentration was kept constant in all experiments and the extra dyed fibrinogen did not affect pure fibrin clot mechanical properties (see Figure 2-2). Bacterial cells were stained for 30 minutes with 20μM SYTO® 40 (420/441) (Thermo Fisher Scientific, Waltham, MA, USA) and washed twice with HBSS before re-suspension in Fg solutions.

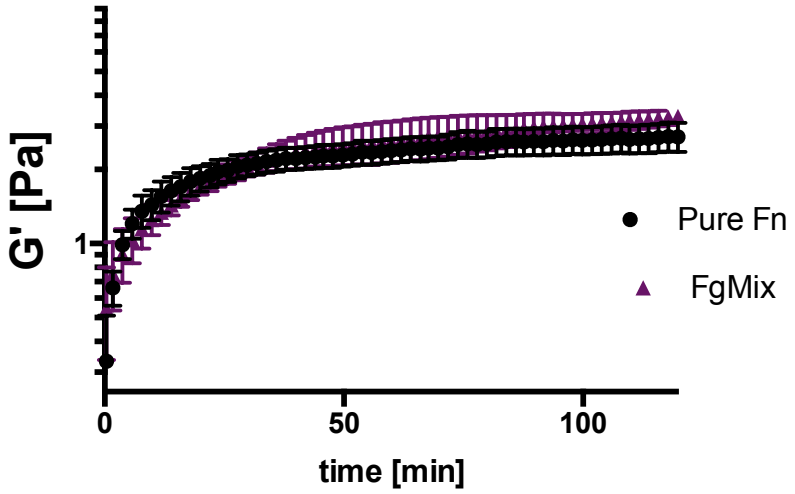

Figure 2-2 | Influence of fluorescent Fg on fibrin formation and mechanical properties

Elastic modulus G' variance over time of fibrin with and without fluorescent Fg. Error bars denote standard error of the mean of n = 3.

Carboxylate-Modified Polystyrene Microspheres, 1.0 μm, red fluorescent (FluoSpheres® 580/605), 2% solids and Sulfate Microspheres, 1.0 μm, yellow-green fluorescent (FluoSpheres® 505/515), 2% solids (Thermo Fisher Scientific Waltham, MA, USA) were used for particle tracking microrheology..

Bovine Serum Albumin (BSA, Sigma-Aldrich St. Louis, MO, USA) was adsorbed to the microsphere surface to control the microsphere's propensity for adsorption to fibrin. BSA was dissolved in filtered deionizing (DI) water. The two different probes (0.1% solids as the final concentration) were incubated with 1 wt.% and 15 wt.% BSA solutions, respectively, on a roller at room temperature for 24 hours. Different probes were washed separately with DI water and re-suspended into Fg or bacterial/Fg solution before clotting with the following concentration: 0.04% solids for 1wt% BSA incubated probes and 0.02% solids for 15wt% BSA incubated ones. In pure fibrin, the former adsorbed to fibers, while the latter diffused freely in the voids of the network. In the infected clot, however, initially free probes become bound to fibrin after about 30 minutes.

2.3.5 Network structure quantification

Fiber Area, bacteria-fibrin overlap percentage and mesh size – the average distance between neighboring strands of fibers – were calculated from binary images, derived from a threshold equal to the image mean intensity of every image, as described by Bendix et al [26]. After thresholding, fibers and bacteria cells are on-pixels and voids are off-pixels in their respective channels. The fiber area was computed by counting the number of fiber on-pixels. Fiber area was normalized by the largest value in the reported time range. Bacteria-fibrin overlap pixels are on-pixels in both the bacteria and fiber channels (c.f Figure 2-3). The overlap percentage of every

image was computed by dividing the overlap area by the fiber area. Image analysis was done in Matlab R2014b (The MathWorks, Natick, MA).

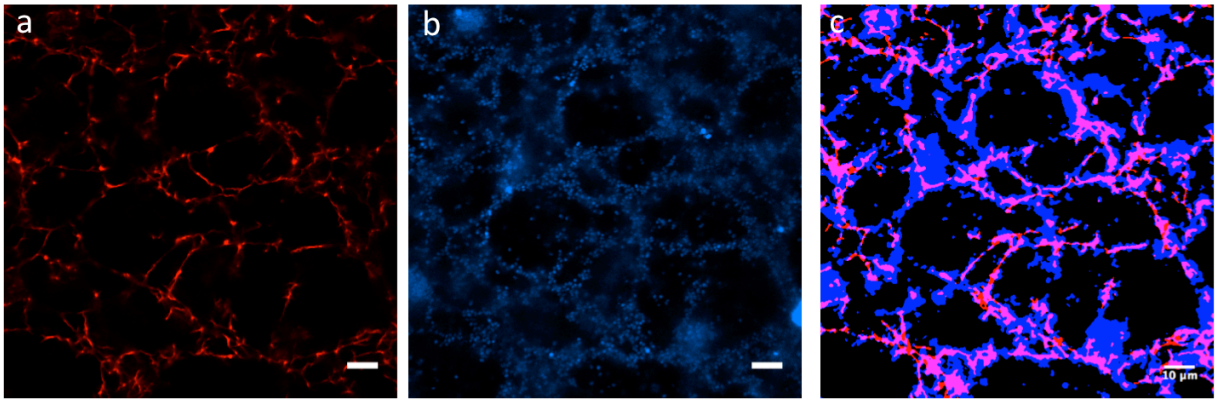

Figure 2-3 | Fiber area and bacteria-fibrin overlap percentage

(a) Single image of the fibrin channel, (b) bacteria channel, and (c) the merged threshold images for the infected clot, in which fibrin is red, bacteria are blue and the overlap regions are magenta. Scale bar = 10 µm.

To compute the mesh size, distances between on-pixels for the fibrin channel were recorded by scanning along pixel rows and columns. Along each dimension, distributions of distances were least-squares fitted to a Poisson distribution, $P = P_0 e^{-\xi/\xi_0}$, with P_0 and the decay length ξ_0 -- taken as the mesh size -- as the fitting parameters. Example analyses for pure fibrin and infected fibrin clots are in Figure 2-4, respectively. The dependence of mesh size fitting on threshold values is negligible around the mean intensity as reported in Figure 2-4c. The mesh size of each image was obtained by averaging the fitted mesh size for all rows and columns. Two populations were resolved for infected clots because the distribution of distances between fibers could not be described by a single Poisson distribution (c.f. Methods and Figure 2-4b). Steady-state mesh size values were calculated by averaging all the stacks in all replicates (at the time interval 60 – 100

min). The reported values for mesh size, fiber area and overlap percentage are the average of all stacks from 20μm to 40μm above the coverslip, acquired at 1μm intervals within the reported time point ± 10min. No less than four sets of z-stacks were included in each reported time bin. The error bars denote the standard deviation of all the stacks in all replicates.

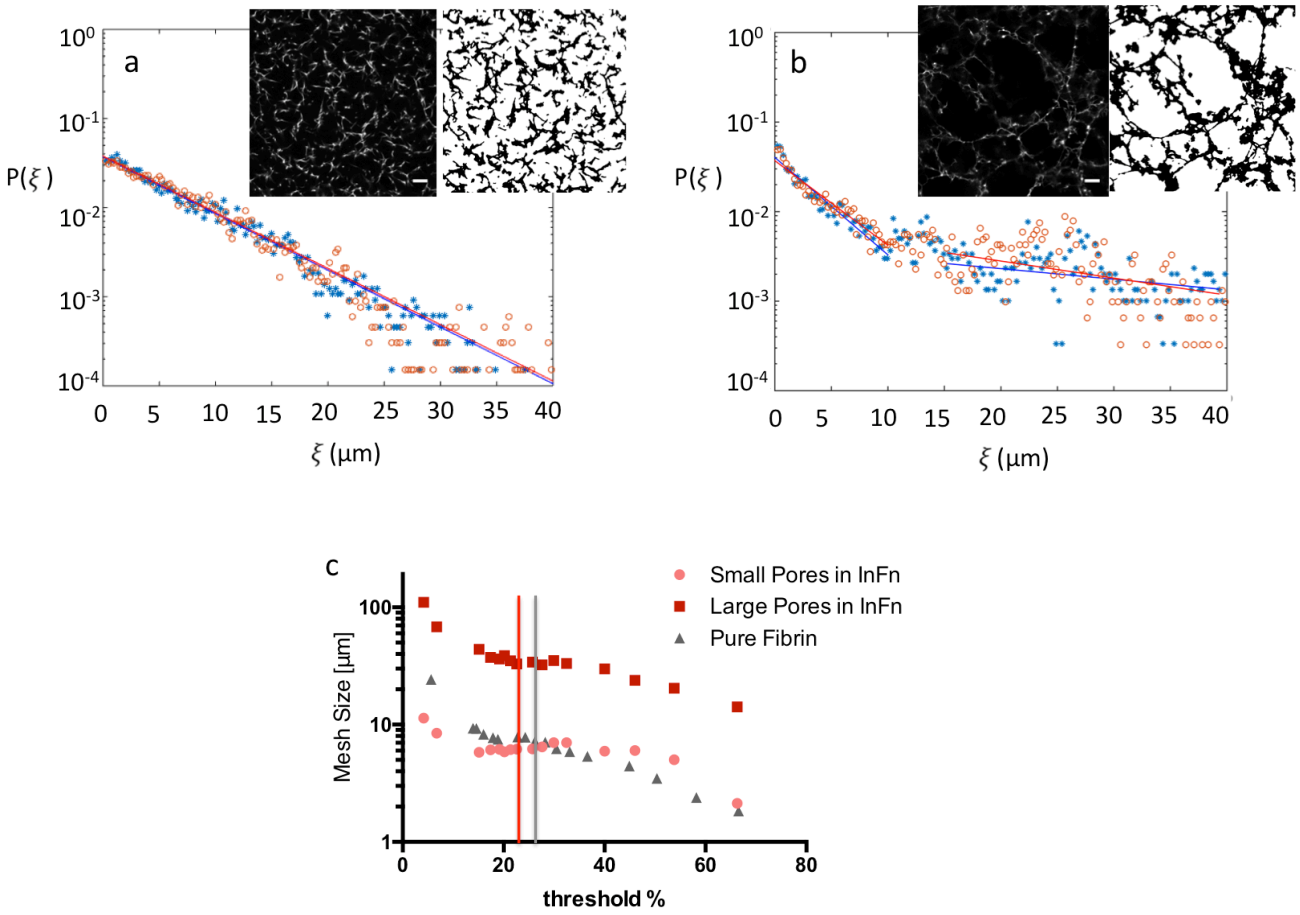

Figure 2-4 | Mesh Size Characterization

Distribution of distances between fibers measured in rows (blue '*') and columns (orange 'o') and single mode and bimodal exponential fits for (a) pure fibrin and (b) infected fibrin clot, respectively. The insets are the corresponding confocal 2D slice (left) and its threshold image (right). Scale bar = 10 μm. (c) Threshold-dependence of mesh size results. The threshold value used in this study is the mean intensity of the according slice: the grey line denotes 26% -- the mean intensity of (a) and that of (b) was 23% as denoted by the red line.

2.3.6 Microrheology

Particle tracking has been used in a variety of research topics[27,28,29]. In this study, microrheology measurements were performed by multiple-particle tracking (MPT) with confocal microscopy. The premise of MPT microrheology is that the motion of a probe particle reflects its local mechanical environment[28,29]. Fluorescent polystyrene spheres of $1\mu m$ as described above were used as probes. There were two kinds of probes -- free ones that undergo Brownian motion in fibrin voids and bound ones that attach to and fluctuate with the fibrin fibers. From the trajectories we quantified the probes' mean square displacement (MSD) ($\langle \Delta x^2(t) \rangle$) -- the average squared distance a probe travels in a given lag time -- as reported in Figure 2-5 a,b. MSDs were computed from probes' centroids as identified by Trackpy 3.0 (http://soft-matter.github.io/trackpy/stable/). The static error of the MSD was determined to be $\langle \Delta x^2(t) \rangle_{min} = 2{\times}10^{-4} \mu m^2$ by tracking fully immobilized probes at the coverslip[30]. The MSD of the pure fibrin and infected fibrin clots are 83 and 23 times higher than the static error, respectively. In a purely viscous environment the MSD increases linearly with lag time, like the free probes in the voids that contain only buffer (Figure 2-5b). For an elastic material, the MSD exhibits a plateau, independent of lag time, like the behavior of the probes bound to fibrin (Figure 2-5a). Probes bound to the pure fibrin and the infected fibrin clots exhibit plateau MSD magnitudes that differ. That is, the probes are localized in space to differing degrees; probes in the infected clot display a lower plateau MSD (Figure 2-5a) than probes in pure fibrin. By MPT microrheology, these MSD magnitudes are inversely proportional to the elastic modulus:

$$G' = \frac{k_B T}{\pi a \langle \Delta x^2(t) \rangle_{t \to \infty}} \qquad \text{(equation 1)}$$

Where, k_B is the Boltzmann constant, T is the temperature, a is the probe radius and $(\Delta x^2(t))$ is the MSD[31,32]. This expression was used to calculate the MPT elastic moduli reported in the

Results. Three time series movies were obtained for each replicate. The MSD ($\langle \Delta x^2(t) \rangle$) of each replicate was obtained by averaging the tracked particles in the three movies. $(\Delta x^2(t))_{t\to\infty}$ was calculated by averaging $\langle \Delta x^2(t) \rangle$ values within lag time equal to 10 seconds. The G' value of this replicate is then calculated from equation (1).

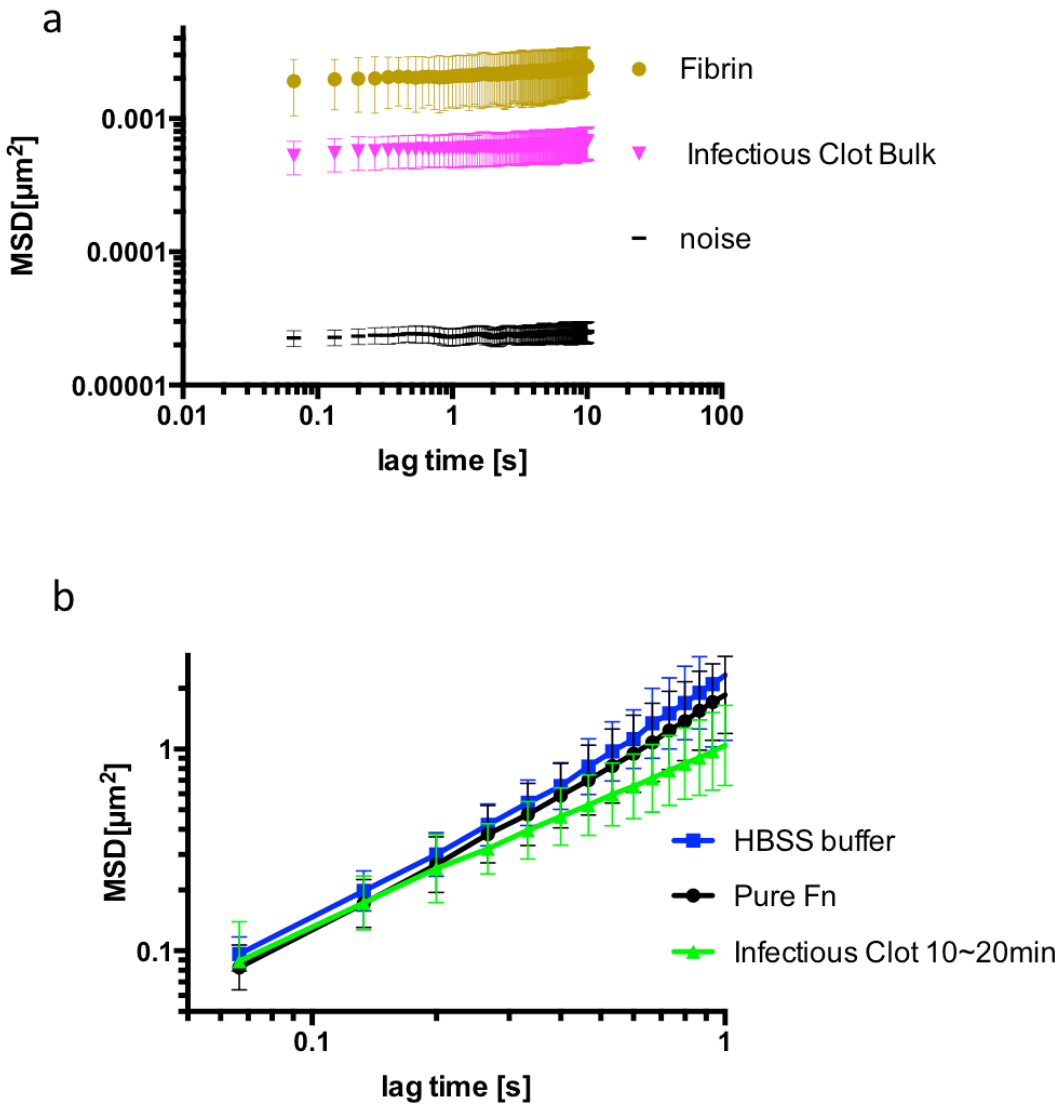

Figure 2-5 | Multiple Particle Tracking Microrheology (MPT) of pure fibrin and infected fibrin clot

(a) Mean square displacement (MSD) curves of probes trapped (15wt% BSA-treated) onto fibrin fibers at steady state. (b) Mean square displacement (MSD) curves of probes freely undergoing

Brownian motion (1wt% BSA-treated) in solvent voids in HBSS buffer, voids of a pure fibrin, and voids of an infected clot (10 minute after clotting and 20±5μm above coverslip). Error bars denote standard deviation of n=3.

2.3.7 Macroscopic clot rupture visualization

Pure fibrin clots and infected fibrin clots were constituted as described above and in an 8-well chamber coverglass and kept in a 37℃ incubator. Samples were taken out of the incubator and photographed every 40±10min.

2.3.8 Comparison of cold vs. warm clot initiation

Warm clot initiation was conducted as following: The fibrinogen (Fg) solution, the cell-Fg mixture and the chamber coverglass dishes were kept in a 37℃ dry bath incubator (Fisher Scientific™ Isotemp™ Digital and Analog Dry Bath Incubators) for temperature to reach 37℃. Solutions were loaded to the chamber coverglass dishes and 0.5U/ml thrombin (final concentration) was added to initiate the polymerization. Chamber coverglass dishes were kept in a 37℃ incubator afterwards.

Cold clot initiation was conducted as described in Methods in the main text. It is used in order to 1) allow time to load the samples on the rheometer plate, 2) capture the entire clotting process. We did not observe significant differences in the trends for mesh size observed for cold clot initiation compared to 37℃ clot initiation (c.f. Figure 2-1). Likewise, macroscopic photos of infected fibrin clots with 37℃ clot initiation demonstrated similar trends in heterogeneity (64%; 14 out of 22 cases) within ten hours as cold initiated clots.

2.3.9 Fluorescent Fibrin Clot Constitution for Bulk Rheology Measurements

Alexa Fluor 546 (~558/573 nm) conjugate human Fg (Thermo Fisher Scientific, Waltham, MA, USA) was mixed with unlabeled fibrinogen in a molar ratio of 1:4 in HBSS. The non-fluorescent Fg concentration was kept constant (0.5mg/ml) in all experiments.

2.3.10 Plasminogen-depleted Fibrin Clot Constitution

Plasminogen-depleted fibrinogen (341578) was purchased from EMD Millipore Corporation (Billerica, MA, USA); in all protocols it was used equivalently to the primary plasminogen source.

2.3.11 Scanning Electron Microscopy

Clots were prepared for scanning electron microscopy (SEM) from mixtures of *S.epidermidis* cells (4×10^9cells/ml), 0.5mg/ml fibrinogen and 0.5U/ml thrombin (final concentration) in HBSS buffer, the same way as described in Methods. Mixtures were prepared on ice. A drop of ~50μl was quickly transferred on to a glass slide pre-coated with 5 wt.% bovine serum albumin (BSA) in PBS buffer overnight. The glass slides were kept in 37℃ for at least 30min before making the samples. After 70min, samples were fixed with 2.5% glutaraldehyde overnight at 4℃. Clots were then washed three times in distilled water, dehydrated in a graded series of increasing ethanol concentrations (30–100%) over three hours. The specimens were mounted, sputter-coated with gold on the SPI-Module Sputter Coater at 2.2kV and 20mA for 40 seconds. Samples was examined in the FEI Nova NanoLab SEM, under 5kV and 0.40nA, and digitalized micrographs were taken under magnifications ranging between 10000-80000X.

2.3.12 Image Analysis for large pore volume fraction

Large pore volume fraction is estimated from its area fraction in the same binary images used for network structure quantifications (c.f. Methods).

$$\phi_{large\ pores} = \frac{\#\ of\ (fiber\ pixels + \ small\ pores\ pixels)}{\#\ of\ total\ pixels}$$

in which the fiber pixels and the small pore pixels are the black ones and the blue ones, respectively, in Figure 2-6. The blue small pores are determined as the enclosed region containing no more than the average pore size in a pure fibrin. This calculation should underestimate the large pore volume fraction due to confocal microscope axial limitations – every slide is actually a $1\mu m$ projection. The blurry fibers should be fibers out of the plane. However, they are counted as fibers in the binary images with the used threshold method therefore lead to multiple times of counting.

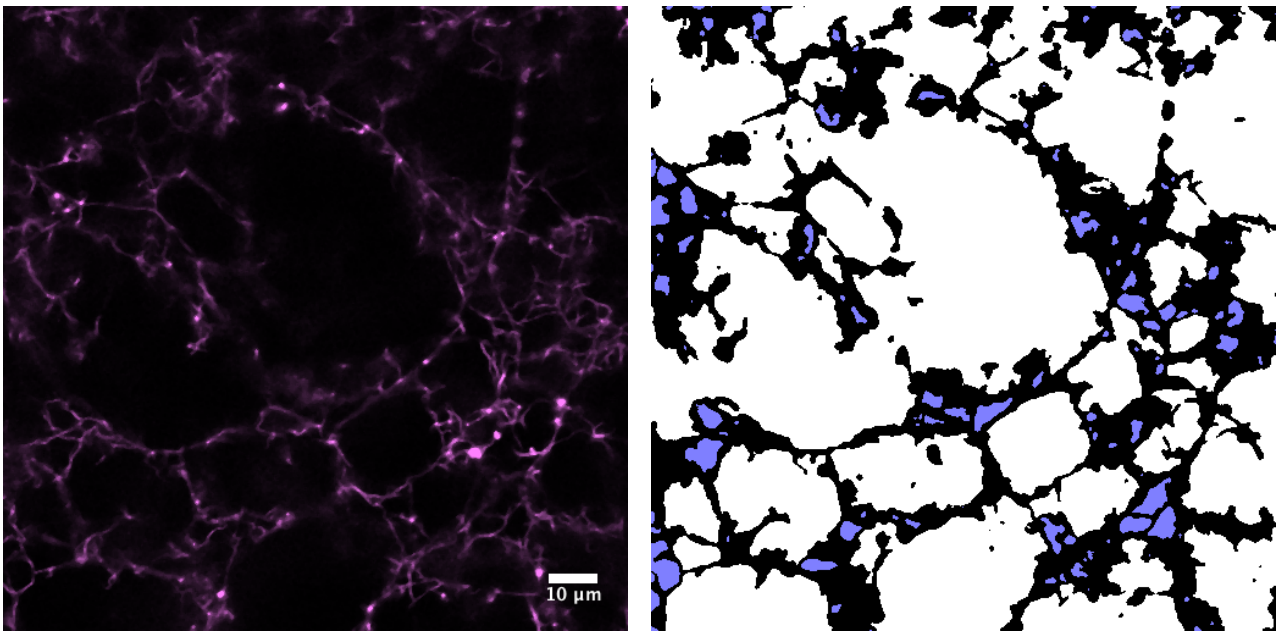

Figure 2-6 Large pore volume fraction

A single stack of infected fibrin channel (left) and its binary image (right). Black pixels denote fibrin fibers, blue pixels denote small pores, white pixels denote large pores that are elastically inactive.

2.4 Results:

2.4.1 *S. epidermidis* alters the elasticity of fibrin clots.

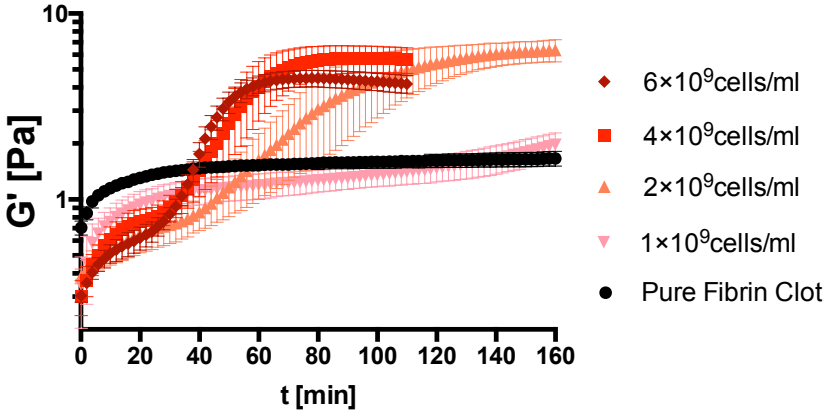

Figure 2-7 | S. epidermidis alters fibrin elasticity.

Elastic modulus, G', of pure fibrin clot (0.5mg/ml) and infected fibrin clots (0.5mg/ml fibrin with 1×10^9cells/ml, 2×10^9cells/ml, 4×10^9cells/ml, 6×10^9cells/ml) variation with time. Error bars denote standard deviation with n=3.

Figure 2-7 reports the effect of bacterial cells on fibrin clot elasticity, as quantified by the linear elastic modulus G′. Without cells, the elasticity of a 0.5 mg/ml pure fibrin clot emerges rapidly, attaining a steady-state value of 1.5 ± 0.2 Pa in ~40 min. The addition of 1×10^9cells/ml has modest effect on the elastic response. However, at higher cell concentrations, the kinetics of the elastic response becomes more complex. Initially the process is retarded and the modulus has a transient plateau at a value less than the steady-state modulus of the pure fibrin clot. Then the elastic modulus rapidly increases to a final steady-state value greater than that of the pure fibrin clot. The dynamics are cell concentration dependent. Specifically, an infected fibrin clot with the highest cell concentration (6×10^9 cells/ml) reaches its steady-state G′ value in about half the time of an infected fibrin clot with 2×10^9 cells/ml. However, as shown in Figure 2-8, the steady-state elastic modulus is about 1.4 times greater at the lower concentration (2×10^9 cells/ml) than the

higher concentration (6×10^9cells/ml). For cell concentrations between 2×10^9 cells/ml and 6×10^9cells/ml, the final steady-state modulus is about 3-4.2 times greater than the pure fibrin clot.

Cell conc. [cells/ml]	0	2×10^9	4×10^9	6×10^9
Steady state G' [Pa]	1.5±0.2	6.3±0.9	5.7±1.0	4.5±0.5

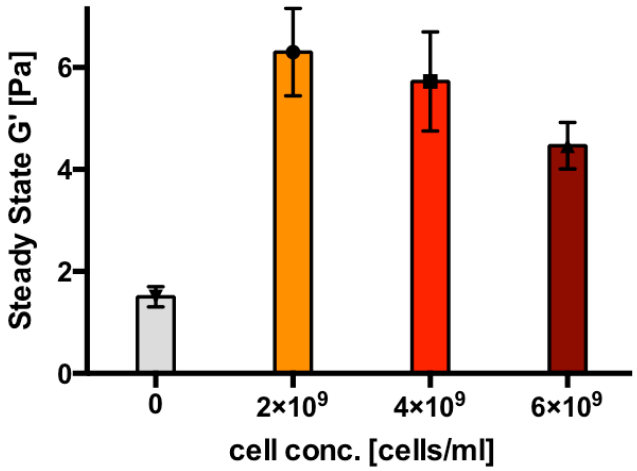

Figure 2-8 | Steady state G' values of infected fibrin clots depend on bacterial cell concentration

Table and graph both show the steady state (c.f. Methods) linear elastic modulus, G', values for infected clots with different *S. epidermidis* cell concentrations. Error bars denote standard deviation of n=3.

2.4.2 *S. epidermidis* generates a heterogeneous fibrin clot microstructure.

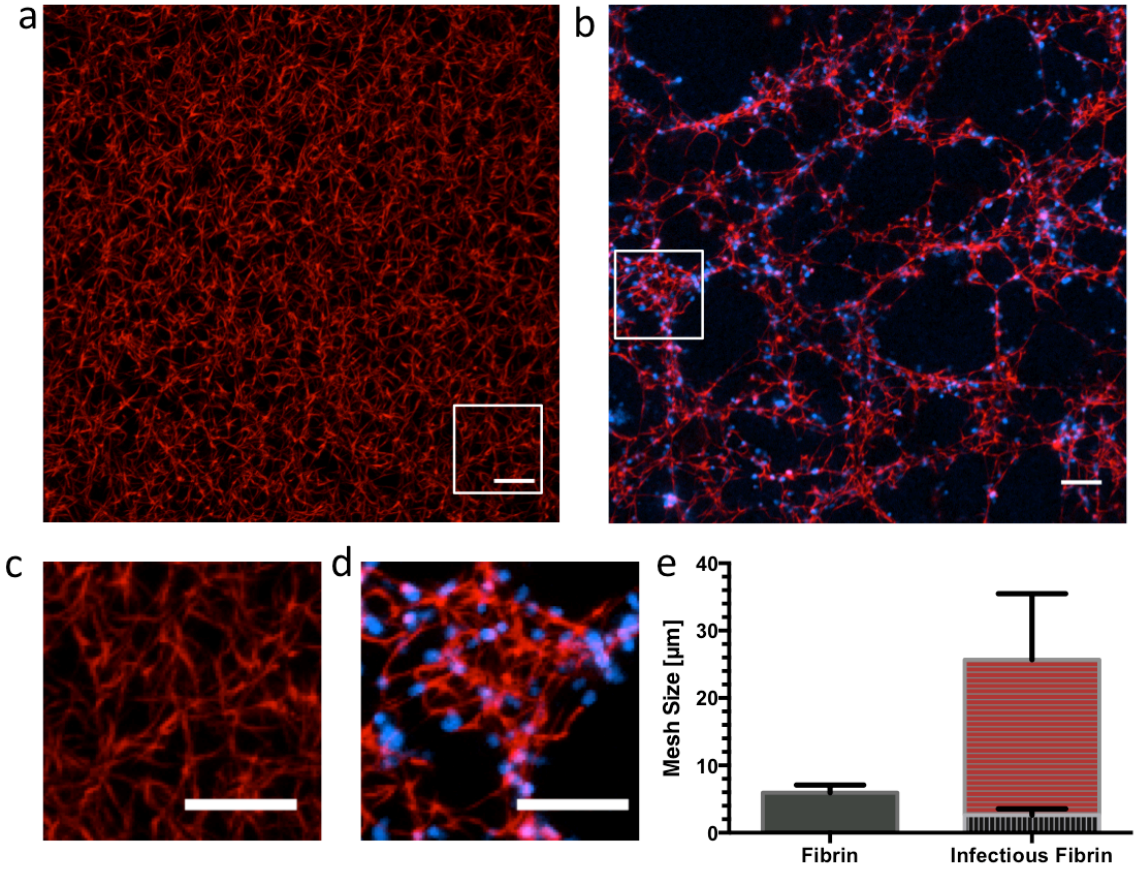

Figure 2-9 | Steady-state microstructure of fibrin clot and infected fibrin clot

(a) Axial projections of a pure fibrin clot (0.5mg/ml) and (b) an infected clot (with 4×10^9cells/ml in 0.5mg/ml fibrin) showing the existence of large pores. Fibrin is red and bacterial cells are blue. (c) High-resolution image from identified region of interest in (a). (d) High-resolution image from region of interest in (b). Scale bar = 10 µm in (a-d). (e) Mesh size characterization of steady state pure fibrin clot and infected fibrin clot. Error bars denote standard deviations of all the image stacks in all five replicates (c.f. Methods).

Figure 2-9 compares the steady-state microstructure (c.f. Methods) of a fibrin clot with that of an infected clot with 4×10^9 *S. epidermidis* cells/ml added. The pure fibrin network is homogeneous and porous with distinct filaments and voids. Image analysis indicates that the mesh size (c.f. Methods) is 5.9 ± 1.1 µm (Figure 2-9a, c, and e), consistent with previous measurements in the literature[13]. The network formed by the infected clot, on the other hand, is heterogeneous (Figure

2-9b and d). Inspection of the image projections suggests that the network mesh size structure cannot be described by a single length scale. Indeed, image analysis detects two characteristic mesh size dimensions (c.f. Methods). The two sizes detected (2.6 ± 1.0 μm and 23.1 ± 9.8 μm) differ by about a factor of ten (Figure 2-9e). The larger pore size in the infected clot network is about four times the pore size in the pure fibrin clot. Figure 2-9d shows details of the small pores, which are about half the size of the homogeneous pure fibrin network in Figure 2-9c.

2.4.3 Microrheology connects microstructure and elasticity.

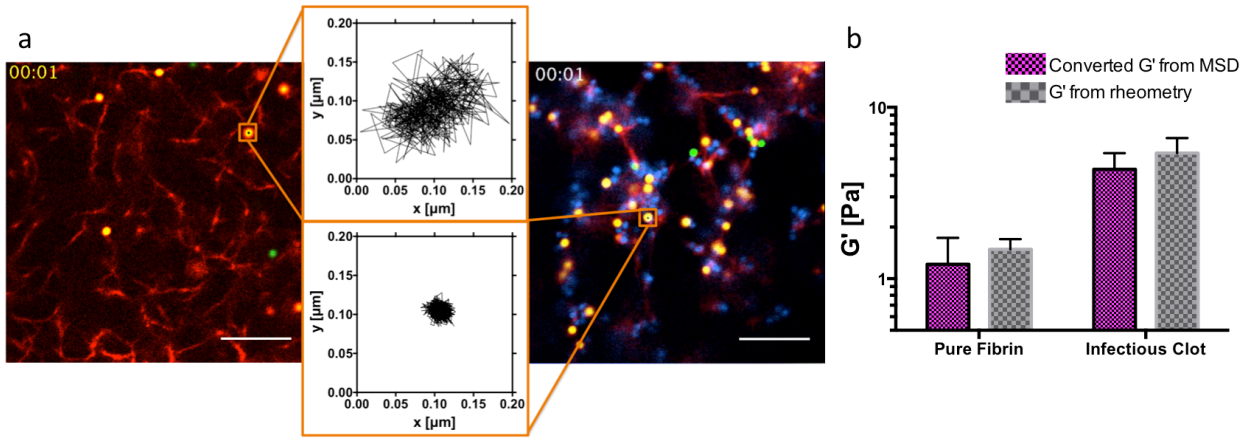

Figure 2-10 Multiple Particle Tracking (MPT) Microrheology in fibrin and infected clots

(a) One image stack from a time series images of MPT in a pure fibrin and infected clot. Fibrin is red; bacteria are blue; Probes bound to fibrin are yellow; freely diffusing probes are green (c.f. Methods). The zoomed-in plots show the trajectories of the bound probes in pure fibrin and infected fibrin, respectively. The fluctuation of probes bound to fibrin is inversely proportional to the elastic modulus. (b) Comparison between steady state elastic modulus G' obtained from bulk rheology and G' calculated from MPT (c.f. Methods). Error bars denote standard deviations with n = 3.

We hypothesized that the observed changes in clot elasticity (Figure 2-7) could be attributed to the heterogeneous structure generated by the presence of *S.epidermidis* (Figure 2-9). To test this

hypothesis, we measured, by microrheology[33], the change in elastic modulus G' of the fibrin network, as induced by added bacteria. The elastic modulus was characterized by direct visualization of the microscopic dynamics of the fibrin network. The mean-squared displacement (MSD) of submicron particle probes embedded in an elastic medium was used to characterize the medium's elastic modulus G' (c.f. Methods). Physically, the more localized the fluctuating displacements of the probe, the greater the elastic modulus of the medium. We found significant differences in probe MSD in pure fibrin and infected fibrin clots (Figure 2-10a). These differences yield elastic moduli that differ by a factor of 3.6 ± 1.2 (Figure 2-10b), consistent with the bulk rheology in Figure 2-7. Thus, differences in the dynamics of the fibrin network with and without cells correlate with the different elastic moduli of pure fibrin and infected fibrin clots.

2.4.4 *S. epidermidis* changes the microstructure of a fibrin clot over time

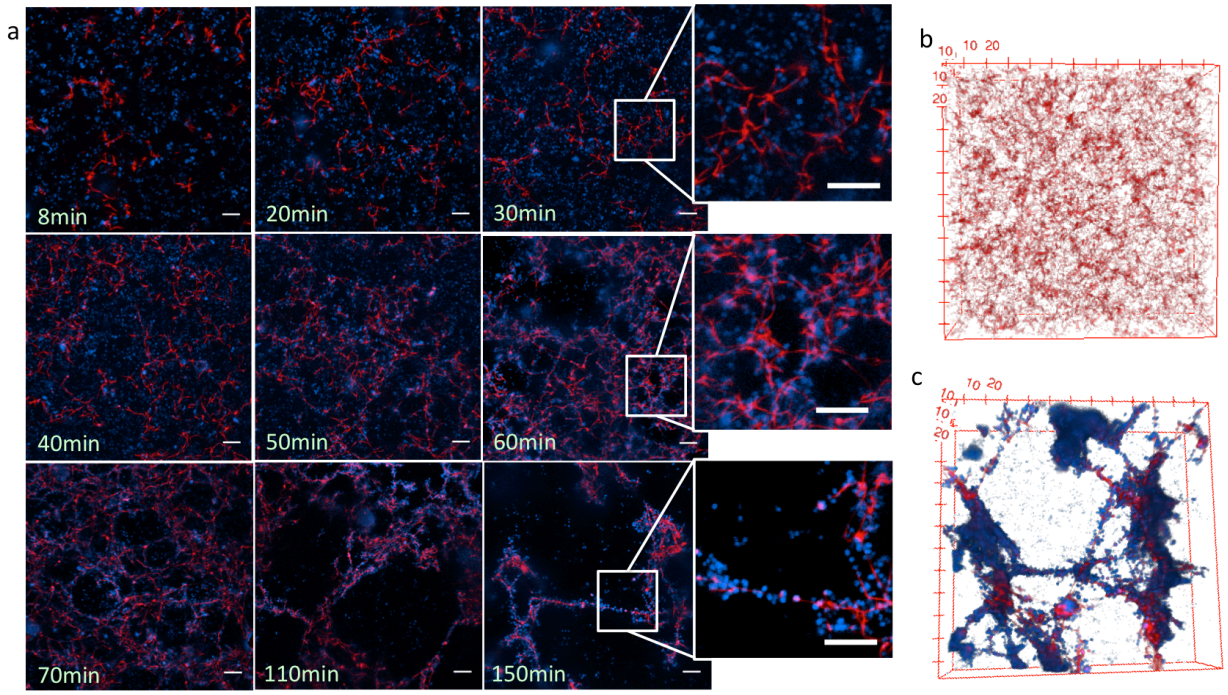

Figure 2-11 | Infected fibrin clot formation and rupture

(a) Axial projections of an infected clot (4×10^9cells/ml in 0.5mg/ml fibrin) rendered from 20 ¦ m to 30 ¦ m above the cover slip at 1 ¦ m intervals at different time points. Fibrin is stained red and bacteria are stained blue. Scale bar = 10 µm in all images. (b,c) Renderings of three-dimensional image volume of (b) a pure fibrin clot and (c) the region in the infected clot showed in (a), captured 150 minutes after adding thrombin. The width and height of volumes in (b) and (c) are 127 µm and 50 µm, respectively.

Confocal microscopy images in Figure 2-11a demonstrate how the structure of an infected fibrin clot evolves over time. Fibrin becomes visible as red pixels on the confocal microscope once fibrinogen monomers are polymerized into fibrin fibers by thrombin. Blue stained cells in the zoomed-in images show the transition from free floating cells that are evenly distributed at 30min to cells adhered onto the fibrin fibers between 60min and 150min. The change in fibrin color from red to pink is due to the co-localization of the fibrin (red) and the bacteria (blue). The large pores of the infected fibrin clot increase in size over time. The three-dimensional confocal

microscopy volumes of a pure fibrin clot (Figure 2-11b) and the corresponding region in the infected fibrin clot at 150 min (Figure 2-11c) shows that the latter has a greater heterogeneity in terms of fibrin structure and distribution of bacteria. Again, in this case the fibrin is co-localized with bacteria or bacterial aggregates.

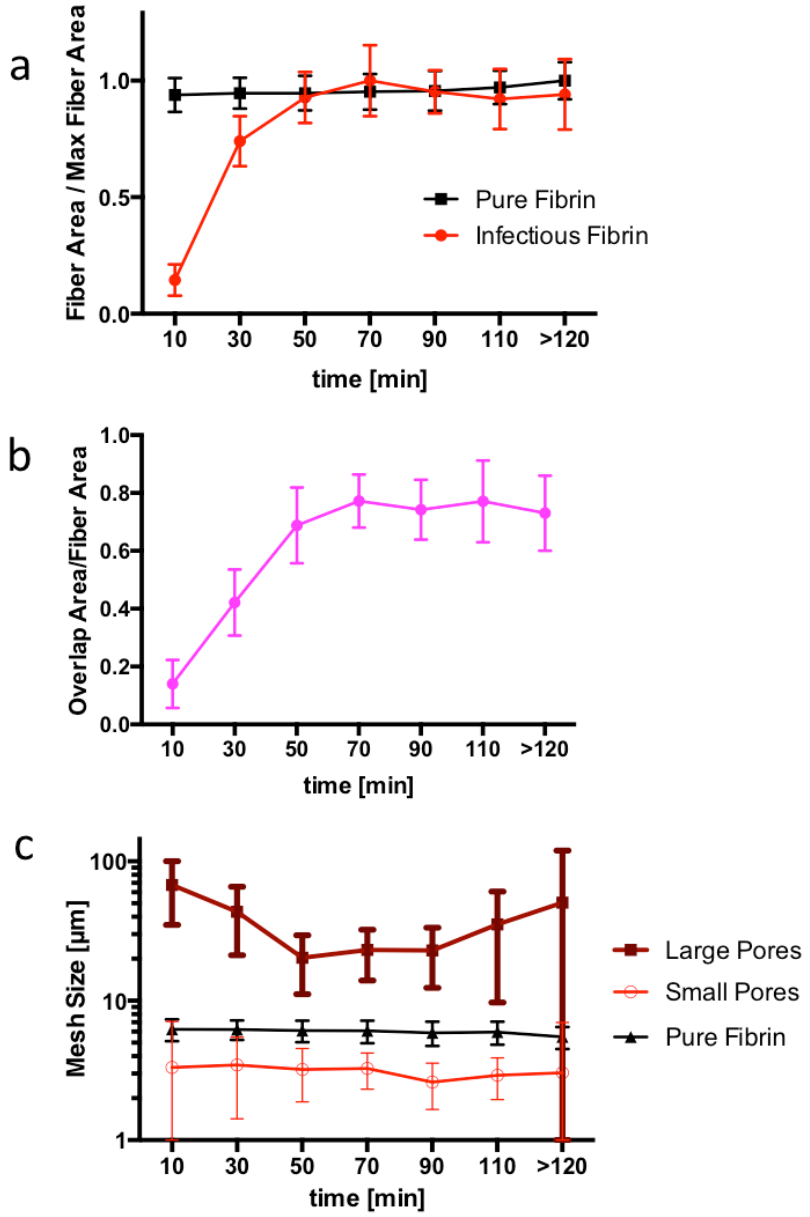

Figure 2-12 | Microstructural change during the infected fibrin clotting process

The variance of (a) normalized fiber area, (b) bacteria fibrin overlap percentage and (c) mesh sizes during the infected fibrin and the pure fibrin clotting process. Error bars denote standard deviation of n=5.

The temporal variation of normalized fibrin area, bacteria-fibrin overlap percentage (bacteria-fibrin overlap area / fibrin area), and mesh size are reported in Figure 2-12 (c.f. Methods). The fiber area of the infected clots increases until around 50 min and then remains constant (Figure 2-12a). The fiber area measurement characterizes the formation of the fibrin network as fibrinogen monomers are consumed to form visible fibrin. Compared to the pure fibrin curve, the formation of an infected clot is considerably slowed. This result agrees with the macroscopic elastic response reported in Figure 2-7.

Figure 2-12b shows the bacteria-fibrin overlap percentage. There is little overlap before 10 min – bacterial cells are free floating within this interval. The percentage increases until 70 min at which time it reaches a plateau of nearly 80%. That is, nearly 80% of the fibrin is covered with cells. The critical point of this cell-binding event (~30 min) is on the same time scale as the second step in Figure 2-7 ($4\times10^{9} cells/ml$). That is, the transition from the first plateau to the second plateau of G' coincides with cell-fibrin association.

The mesh size variation with time of pure and infected clot is reported in Figure 2-12c. The pure fibrin mesh size is nearly independent of time. For the infected clots, the small pore size is also steady. However, the average size of the large pores first decreases in size (before 50 min) and then reaches a minimum at ~ 70 min. After 90 min, however, both large pore mean value and its standard deviation increase again. This increase in both standard deviation and the difference

between the small and large pore size indicates an increase in spatial heterogeneity in the network, consistent with the images in Figure 2-11.

2.4.5 *S. epidermidis* effects on fibrin microstructure and elasticity lead to macroscopic changes in infected clots at long times

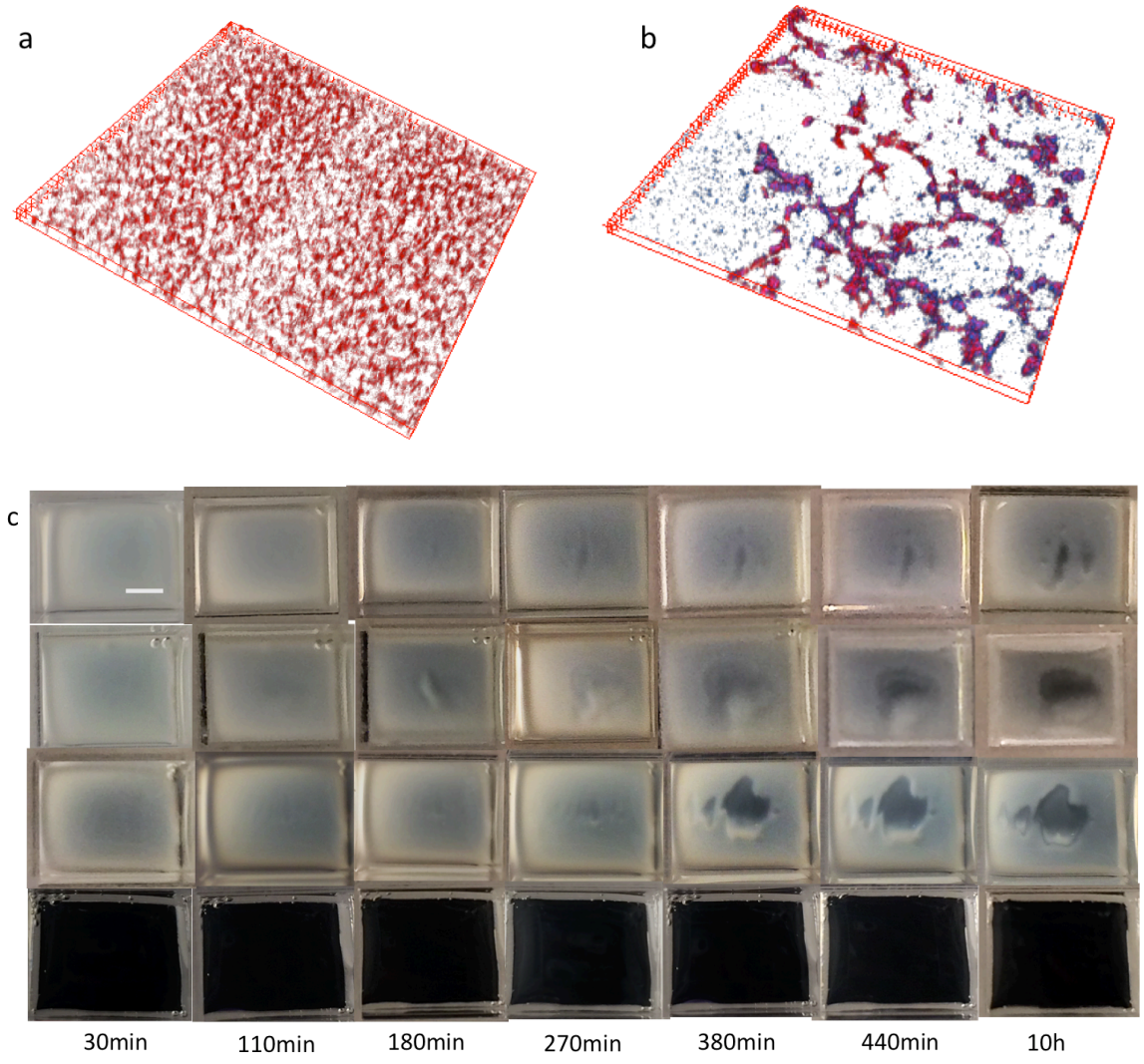

Figure 2-13 | Multiscale imaging of infected fibrin clots

Confocal microscopy three-dimensional volumes of (a) a pure fibrin clot and (b) an infected clot, imaged 5 h. Fibrin is stained red; cells are stained blue. The width and height of the volumes are 254 μm and 10 μm, respectively. (c) Triplicate time-lapse photos of infected fibrin clots with

4×10^9cells/ml (top three rows) compared to pure fibrin clot (bottom row) in chamber coverglass wells. Scale bar in the first photo = 3mm.

To test the effect of *S.epidermidis* on fibrin clots at longer times, we first used confocal microscopy to capture the mesoscopic heterogeneity of the network five hours after adding thrombin (Figure 2-13a,b). It shows that the heterogeneity of the infected clot persisted and increased in dimension to the mesoscopic scale; in comparison the pure fibrin clot remains homogeneous. We further found that *S. epidermidis* can change a fibrin clot macroscopically; time-lapse images of infected fibrin clots and a pure fibrin clot in chamber glass wells are reported in Figure 2-13c. Pure fibrin clot is homogeneous and transparent. The infected clot is turbid due to the presence of the *S. epidermidis* cells. This macroscopic opacity – both its intensity and its spatial distribution – is a function of the cell distribution in the infected clot. This cell distribution tracks the distribution of fibrin because cells adhere to the fibrin network (Figure 2-11 & 2-12). The images of the infected fibrin clots initially show spatially homogeneous turbidity. However, beginning at about 180 min, visual evidence of local imperfections becomes apparent. These local imperfections grow in size. At late times, the previously contiguous fibrin clot now appears torn or ruptured; the central region is clear and free of turbidity. Within ten hours, macroscopic heterogeneity was observed in 74% (17 out of 23) of the infected fibrin clots studied. No heterogeneity was observed in any of the ten pure fibrin clot controls, consistent with microscopic observations of homogeneous, time-independent fibrin microstructure for up to ten hours (c.f. Figure 2-14) as well as optical density measurements of the fibrin network itself (c.f. Figure 2-15).

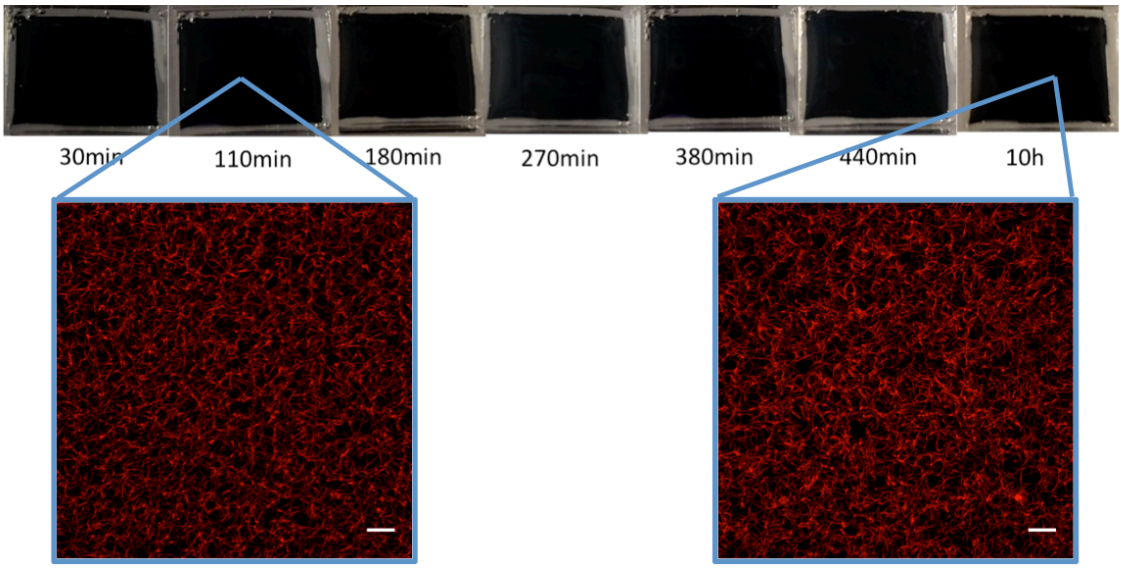

Figure 2-14 | Pure fibrin maintains its microstructure for at least 10h

25 uniformly-spaced positions were imaged across the sample at each given time point. Two Z-stacks of pure fibrin microstructures reported here are representative of the 25 images at the corresponding given time points. The microstructure is not significantly changed after 10 hrs, suggesting that any fibrinolytic proteins in the fibrinogen media are not active in the cell-free controls. Scale bar = 10 μm.

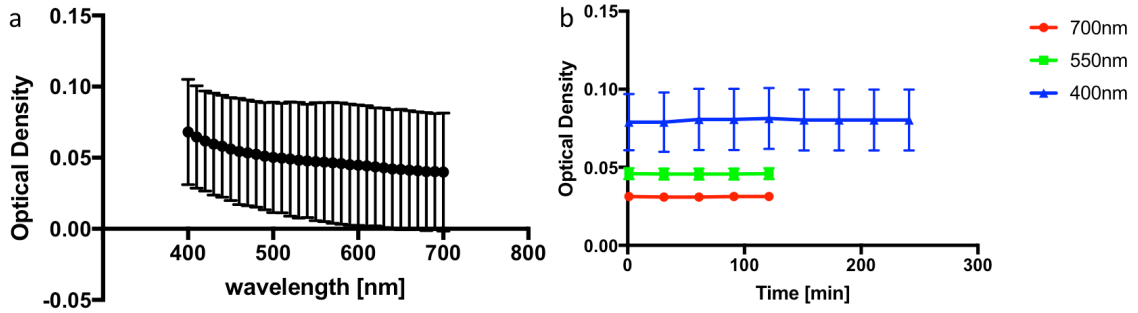

Figure 2-15 | Pure Fibrin Optical Density Over Spectrum and Time

Pure fibrin optical density was measured with a Biotek Spectrophotometer B20. (a) Within the range of the visible light spectrum, the optical density of a pure fibrin specimen at one hour after clot initiation is lower than 0.1, and therefore difficult to visualize with the naked eye. (b) The optical density of the pure fibrin specimen is low and constant with time at three different wavelengths (700nm, 550nm, 400nm). This experiment, taken together with the microstructural information, confirms that no structural changes occur in the pure fibrin networks over time.

The observations of infected clot instability are maintained when physiological concentrations of albumin are added to the HBSS buffer (c.f. Figure 2-16). Moreover, when the fibrin network is constituted from plasminogen-depleted fibrinogen solution, clot heterogeneity is still observed; however, the kinetics of instability is different, as quantified by the reduced probability of macroscopic rupture (1 of 11 for plasminogen-depleted specimens vs 17 of 23 for the primary plasminogen source), at 10 hours, c.f. Figure 2-17). Therefore, quantitative details of the infected clot heterogeneous structure and instability depend on whether or not the fibrinogen solution is depleted of plasminogen. Because some strains of *Staphylococcus* can produce enzymes that degrade host proteins (e.g. by converting plasminogen to plasmin) [17] , this observation offers a potential mechanistic explanation for the rupture and remodeling of fibrin by *S.epidermidis***.**

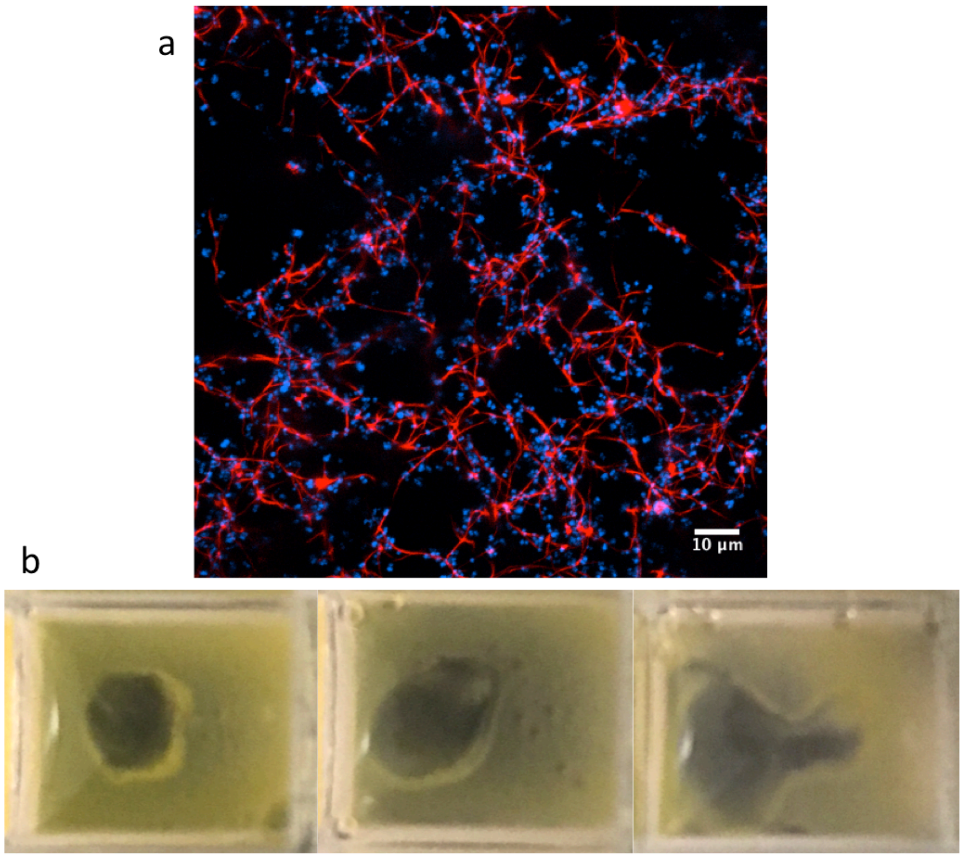

Figure 2-16 Infected Clot constituted with Bovine Serum Albumin (BSA) added to HBSS solution

(a) Axial projections of an infected fibrin formed in a solvent containing 7mg/ml BSA (physiological albumin to fibrinogen ratio). Fibrin is red, *S. epidermidis* is blue. (Compare to Figure 2-9b) (c) Triplicate infected fibrin clots formed in BSA-HBSS solvent in chamber coverglass wells at 10h (Compare to Figure 2-13c). This result shows that bacterial-fibrin interactions remain the same in a system that contains the most abundant plasma protein, present at physiological levels.

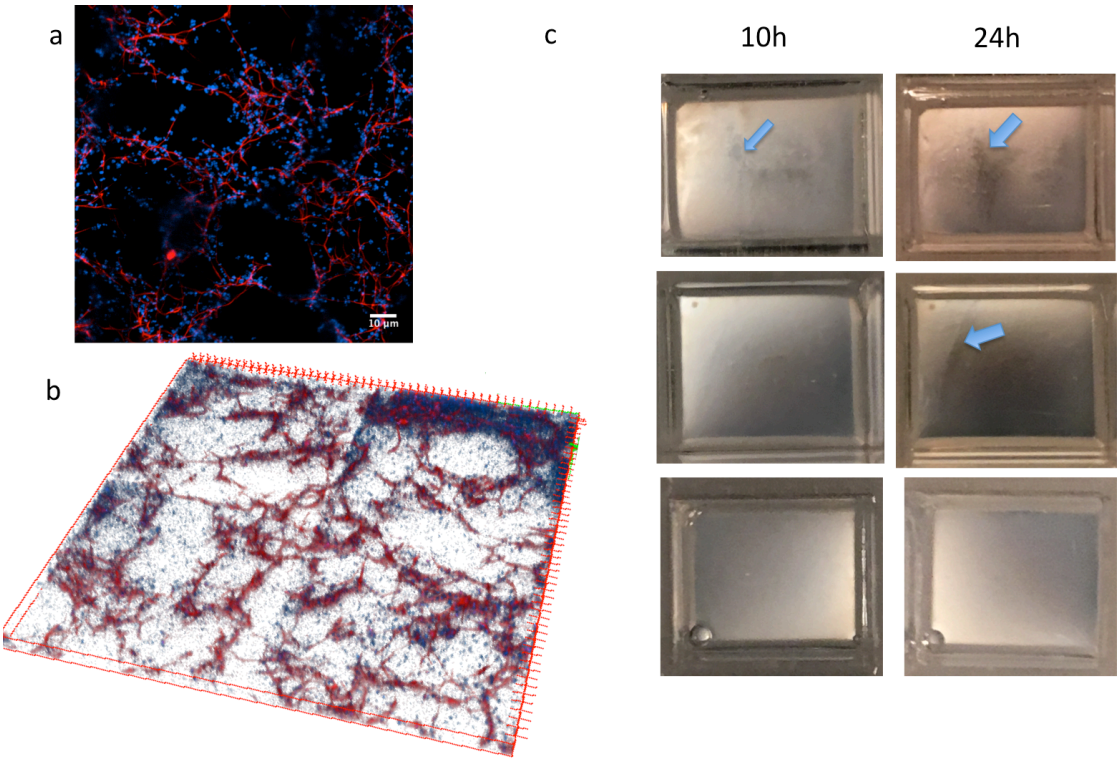

Figure 2-17 | Infected Clot with Plasminogen-depleted Fibrinogen

(a) Axial projections of an infected fibrin clot formed with plasminogen-depleted fibrinogen (Compare to Figure 2-9b). (b) Confocal microscopy three-dimensional volumes of an infected clot formed with plasminogen-depleted fibrinogen, imaged 5 h. Fibrin is stained red; cells are stained blue. The width and height of the volumes are 254 μm and 10 μm, respectively. Fibrin is red, *S.epidermidis* is blue (Compare to Figure 2-13b). (c) Three replicates of infected fibrin clots formed with plasminogen-depleted fibrinogen in chamber coverglass wells at 10h (one out of 11 samples showed noticeable heterogeneity) and 24h (five out of 11 samples showed noticeable heterogeneity). Arrows show the regions of rupture. The inner area in each well is 0.7cm^2. (Compare to Figure 2-13c)

2.4.6 Descriptions of infected fibrin clots with higher fibrin concentration

In Figure 2-18, with the same cell concentration in a four-fold concentrated fibrinogen solution (2mg/ml), the shape of the two-step bulk rheology curve is maintained and the final bulk elasticity was greater than the pure fibrin clot. However, the difference between the pure and infected fibrin steady-state G′ value is reduced and the inflection point of the infected clot curve comes later. Specifically, the 2mg/ml infected fibrin curve first increases rapidly as the

polymerization occurs and then attains a plateau (23.0 ± 4.4 Pa) that is slightly lower than pure fibrin (30.6 ± 2.4 Pa) until 100 min, when there is a sudden increase in G′. The clot reaches its steady-state G′ value (65.8±7.8 Pa), which is about 2.2 times greater than for pure fibrin. In Figure 2-19, mesoscopic heterogeneity was observed in both 1.0mg/ml and 1.5mg/ml infected clots within five hours. Within 24 hours, the 1.0mg/ml and 1.5mg/ml infected clots show macroscopic heterogeneity. Neither macroscopic nor mesoscopic ruptures were observed with the specified cell concentration in the 2.0mg/ml infected clots within 24 hours.

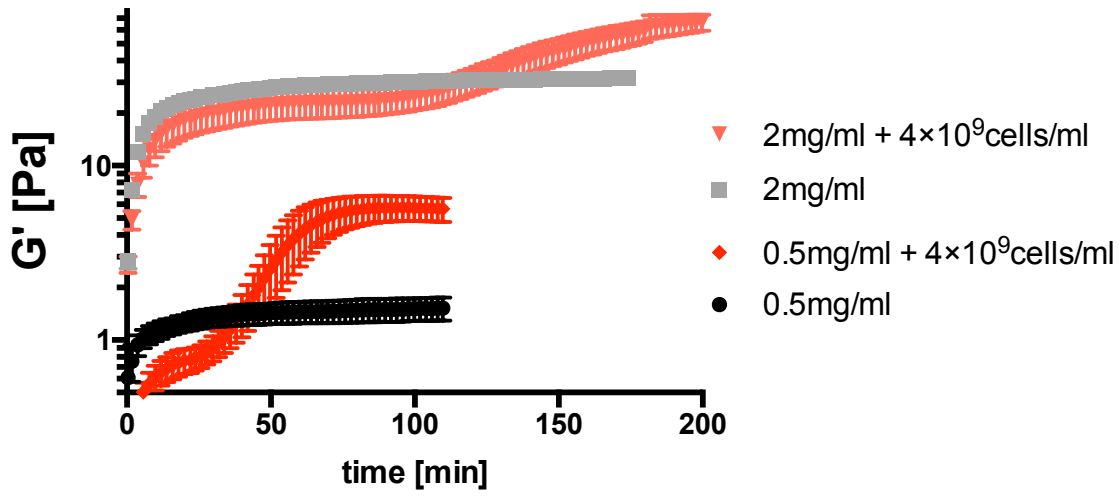

Figure 2-18 Infected fibrin clot at 2mg/ml

Linear elastic modulus, G', as a function of time for different fibrinogen (Fg) concentrations (0.5mg/ml and 2mg/ml) and with (red and orange) and without (black and grey) *S. epidermidis* cells (4×10^9cells/ml). Error bars denote standard error of the mean of n = 3.

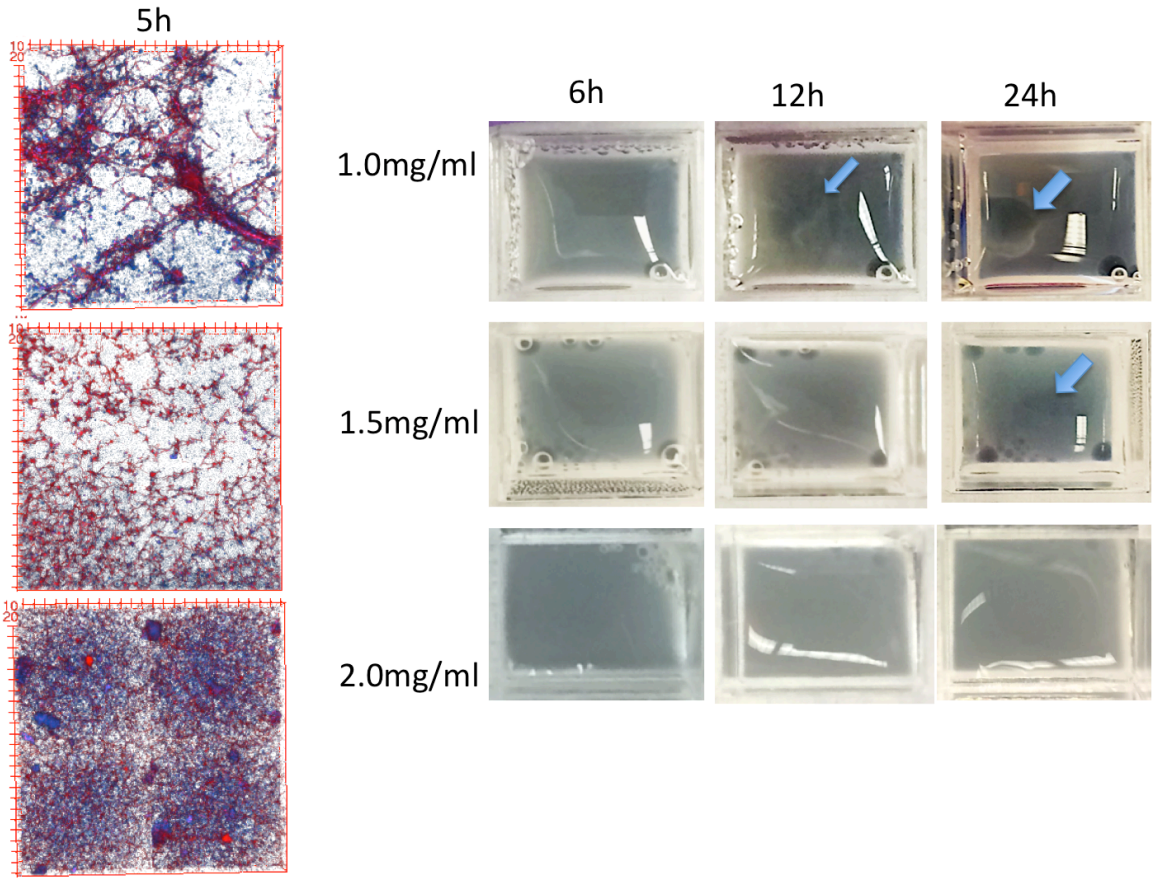

Figure 2-19 | Infected clot rupturing events

(Left panel): 3D confocal laser scanning microscopy (CLSM) images of infected clot at five hours after clotting with corresponding fibrin concentration to the right panel. Red denotes fibrin, blue denotes bacteria. Length of the volume = 128μm. Height of the volume is 50 μm. Images are obtained by stitching four stacks together. (Right panel): Images of infected clots with different fibrin concentrations at 6, 12 and 24 hours after clotting. Arrows show the ruptured spots. The inner area in each well is 0.7cm^2.

2.4.7 A composition model could explain the increased infected clot G'

The infected clot demonstrates a bimodal mesh size distribution, which yields a G' value higher than a pure fibrin clot. The large pores in this case are elastically inactive; they would act to reduce the elastic modulus of a small mesh size fibrin network by an amount proportional to their volume. Here we propose a composition model:

$$G'_{bimodal} = (1 - \emptyset_{large\ pores}) G'_{small\ mesh} \qquad \text{eqn (S1)}$$

in which $G'_{bimodal}$ is the experimental elastic modulus of the bimodal infected fibrin network; $G'_{small\ mesh}$ is the hypothetical homogeneous fibrin network with the small mesh size population. The lower bound of the large pore volume fraction is $80 \pm 4\%$ (c.f. Figure2-6 and Methods). Scanning electron microscopy (Figure 2-20) suggests that the fibrin fiber diameter in these regions is unchanged by addition of bacteria. The local elastic modulus of the smaller pore size regions of the infected clot is consequently predicted to be 82 ± 63 Pa from eqn (2). Combined with the bound on the large pore size, an upper bound on the infected clot elastic modulus of 16 ± 13 Pa is predicted by eqn S1, an increase of a factor of 11 ± 9. The large errors of these estimates stem from the large sensitivity of the elastic modulus to the mesh size. The actual increase is a factor of 4 ± 1 from Figure 2-7 and Figure 2-8. An alternative view is that for the model and measurements to be in accord, the large pore volume fraction would need to be $90\% \pm 9\%$ as compared to the image (lower bound) estimate of 80% ± 4%. These discrepancies could be due to experimental limitations in measuring the large pore volume fraction, an indication of the strong sensitivity of fibrin network elastic modulus to fiber radius ($G_s \sim r^8$) and mesh size ($G_s \sim \square^{-5}$), or a failure of the biomodal model itself. However, even given the discrepancy, the model comparison suggests that effect of the cells on the clot mechanics is to open large voids. These voids have two effects on elasticity that offset each other. First, the voids are effectively elastically inactive. Second, the voids localize fibrin in dense regions that are comparatively stiffer than the cell-free fibrin network.

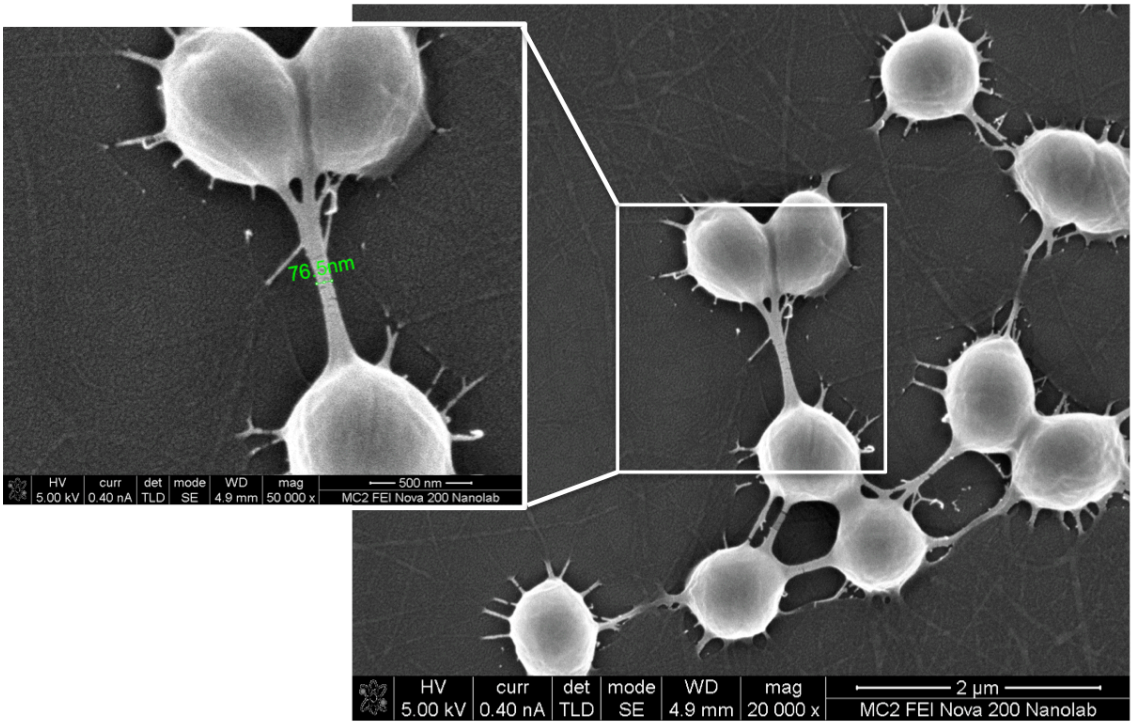

Figure 2-20 | Scanning Electron Microscopy images of an infected fibrin clot

Spherical objects are *S. epidermidis* cells attaching to the bottom surface, the fibers connecting the cells are fibrin. White square shows the magnified region in the left. The green bar estimates the diameter of the fibrin fibers. Images were taken as described in Methods.

2.4.8 Protein-cell interaction could explain the slower clotting kinetics

In addition to the increasing elastic modulus, the additional of cells also changes the kinetics of fibrin structure formation and the infected clot elasticity development. Specifically, the infected clots require around twice the time of pure fibrin to reach steady state: 44 min for pure fibrin clot; 86 min for infected fibrin clot. Assuming the fibrin polymerization rate depends on the reaction rate for thrombin-mediated cleavage of fibrinogen, the process is modeled as:

$$E + S \underset{k_{-1}}{\overset{k_1}{\rightleftharpoons}} E \bullet S \underset{k_{-2}}{\overset{k_2}{\rightleftharpoons}} E + P \qquad \text{eqn (S2)}$$

in which, E is the enzyme – thrombin, S is the substrate – fibrinogen, P is the product – cleaved fibrinogen molecules, which will then immediately polymerize to fibrin. In this model [34] the time to 95% consumption of fibrinogen is:

$$\Delta t = \frac{0.95[S_0]+K_m(ln20)}{k_2[E_{tot}]} \qquad \text{eqn (S3)}$$

in which $[S_0]$ is the initial substrate concentration, K_m is the Michaelis constant, k_2 is the forward reaction rate constant of the second reaction shown in (eqn S2), and $[E_{tot}]$ is the total concentration of the enzyme. The reaction constants are independent of the presence of bacterial cells. However, the time to reach steady state depends on the protein concentrations – fibrinogen or thrombin, which could be altered by their adsorption or binding to the bacterial cell wall.

Estimates suggest that even if all of the cell surface were covered with a fibrinogen monolayer, overall fibrinogen solution concentration would decrease by only 1%. Thus, fibrinogen adsorption by bacterial does not explain the slower kinetics. On the other hand, if half ($0.25U/ml$) of the total thrombin concentration is sequestered on cell surfaces, the effective free thrombin available for cleaving fibrinogen to form fibrin would drop by an equivalent amount. This change would double the time to steady state (eqn S3). This hypothesis is plausible. First, under the conditions of this study, thrombin is reported to be positively charged[35] and therefore could adsorb on *S. epidermidis* (zeta potential of -26 $\pm$ 2 mV[36]) due to non-specific electrostatic interactions. Second, the bacterial cell surface area is ~ $0.8\,\mu m^2/cell$. 50% sequestration would require only 2% of the total available cell surface area be adsorbed by thrombin[37]. This coverage is reasonable because up to 60% of the staphylococcal cell wall is comprised of wall teichoic acids (WTA), which are polyanionic [38]. In fact, WTA is reported to be highly associated with cationic peptides targeting cell walls [39]. Thus, it is plausible that positively charged thrombin

molecules are sequestered on the WTA-rich, negatively charged bacterial surfaces, thereby impacting the kinetics of infected clot development.

2.5 Discussion

This study quantifies the significant impact of *S. epidermidis* on the structure, mechanics, and instability of an *in vitro* model of a blood clot on both microscopic and macroscopic scales. Here we consider: (i) potential limitations on the generality of the results; (ii) mechanistic origins of the cellular effects on clotting kinetics, elasticity and clot microstructure; (iii) implications of the findings for human disease.

A fibrinogen concentration of 0.5 mg/ml was used to produce the model clots; a potential limitation of the work is that the fibrinogen concentration in normal human plasma is higher (~ 2-4 mg/ml)[40], and the amount attracted to and polymerized on the device surface could vary. The 0.5 mg/ml concentration was selected to meet the sensitivity requirements of microrheology and to shift the effect of *S. epidermidis* on fibrin clot formation to within a duration of ten hours. It was, however, possible to study the effect of higher fibrinogen concentrations on elasticity and meso/macroscopic structural heterogeneity, so as to assess the generalizability of our results. The trends in elastic modulus reported in Figure 2-7 were preserved when the fibrinogen concentration was increased to 2 mg/ml (Figure 2-18). Likewise, macroscopic heterogeneity similar to Figure 2-13 was observed when fibrin concentration was increased (Figure 2-19); however, in this case much longer observation times were required.

The study design recognizes: (i) the need to deconstruct the multiple interactions that occur in physiological infected clots; (ii) the centrality of bacteria-fibrin interactions to infected clot

stability because of the primary role of fibrin in clot mechanics; (iii) the spectrum of choices available to study the bacteria-fibrin interaction. As discussed in the Introduction, the present research represents a limiting case in which bacterial cell attachment and replication are eliminated from the study design. The high bacterial cell concentrations used in the study are appropriate because they are representative of conditions found in vivo, for infected clots in an animal model (22).

Our identification of these elements in the study design provides a roadmap for future work to generate full mechanistic understanding of infected clots under physiological conditions. That is, each of the three conditions in our initial deconstruction could be revisited. Such work would address the additional interactions generated by other blood constituents, particularly platelets. It would bridge between the present study – focused on the bacteria-fibrin interaction – and results on infected clots under physiological conditions (e.g. as in recently reported in *Davies et al*) [41].

The elastic modulus of the model clot could change if the added bacterial cells induce structural changes in the fibrin network itself. A well-tested model of the fibrin network elastic modulus finds that:

$$G_s = \frac{3\pi^2 E^2 r^8}{8 k_B T \xi^5} \qquad \text{(equation 2)}$$

where E is the Young's modulus of a single fibrin fiber, r is the fiber radius, and ξ is the network mesh size[13,42 43]. Unligated fibrin fibers have bending Young's modulus E ~2MPa [25 13 44], A 0.5mg/ml fibrin network has an average fiber radius r ~ 36 nm[14]. With the pure fibrin network mesh size $\xi = 5.9\mu m$ (c.f. Figure 2-9), equation (2) yields a predicted steady-state elastic modulus of 1.4 Pa; this prediction is in agreement with the Figure 2-7 report of 1.5 ± 0.2 Pa.

The infected clot exhibits a bimodal mesh size distribution with average mesh sizes of 23 □m and 2.6 □m. Because of the strong inverse relationship between modulus and mesh size ($G_s \sim \square^{-5}$), the large pore regions are effectively elastically inactive. These regions therefore decrease the infected clot modulus in proportion to their volume fraction. On the other hand, the fibrin network in the infected clot has a higher elastic modulus; some regions are enriched in fibrin relative to the pure fibrin clots as evidenced by their relatively smaller pore size population. Calculations (c.f. Figures 2-6, 2-20) show that the offsetting contributions of the higher local elastic modulus of the smaller pore size regions and the elastically inactive regions of large pore size could explain the observed increase of the infected clot elastic modulus. That is, the analysis suggests that the effect of the cells on the clot mechanics could be to open large voids; these voids localize fibrin in dense regions that are comparatively stiffer than the cell-free fibrin network.

The additional of cells also changes the kinetics of fibrin structure formation and the clot elasticity development. Interactions between host proteins and pathogenic bacteria could generate these effects by reducing the effective concentration of either fibrinogen monomer or thrombin enzyme available for fibrinogen polymerization. In fact, estimates suggest that fibrinogen adsorption by bacteria does not explain the slower kinetics. However, if half ($0.25U/ml$) of the total thrombin concentration is sequestered on cell surfaces, the effective free thrombin available for cleaving fibrinogen to form fibrin would drop by an equivalent amount. Thrombin adsorption to the bacterial surface is consistent with both the charge state and

composition of the *S. epidermidis* cell wall. Reduced concentration of free thrombin would explain the observed retardation kinetics of clot formation.

Previously, colloidal particles have been used to study the influence of micrometer-scale objects on fibrin structure [45]. To evaluate the potential relevance of such findings to the above hypothesis, we performed the following control experiment: Bacterial cells were replaced with 0.5 □m polystyrene particles, incubated in two different concentrations of Bovine Serum Albumin (BSA). In Figure 2-21, we show that low-BSA (0.5%, incubated for 24 hours) coated particles influence the clot structure in a similar way to *S. epidermidis* bacterial cells. On the other hand, high-BSA (15%, incubated for more than a month) coated particles do not create a heterogeneous fibrin structure, functioning instead as an inert, micron-scale filler. Thus, particle surface chemistry appears to be a determinant of whether or not added cells/objects affect fibrin structure. Particle/cell surface chemistry could affect fibrin polymerization through its role in surface-adsorption of thrombin, fibrinogen and/or fibrin oligomers onto the particles/cells, as we earlier hypothesized. The control experiments suggest that the bacterial effect on fibrin structure is mediated by the surface properties of the cells, rather than just by the fact that the cells take up volume in the network.

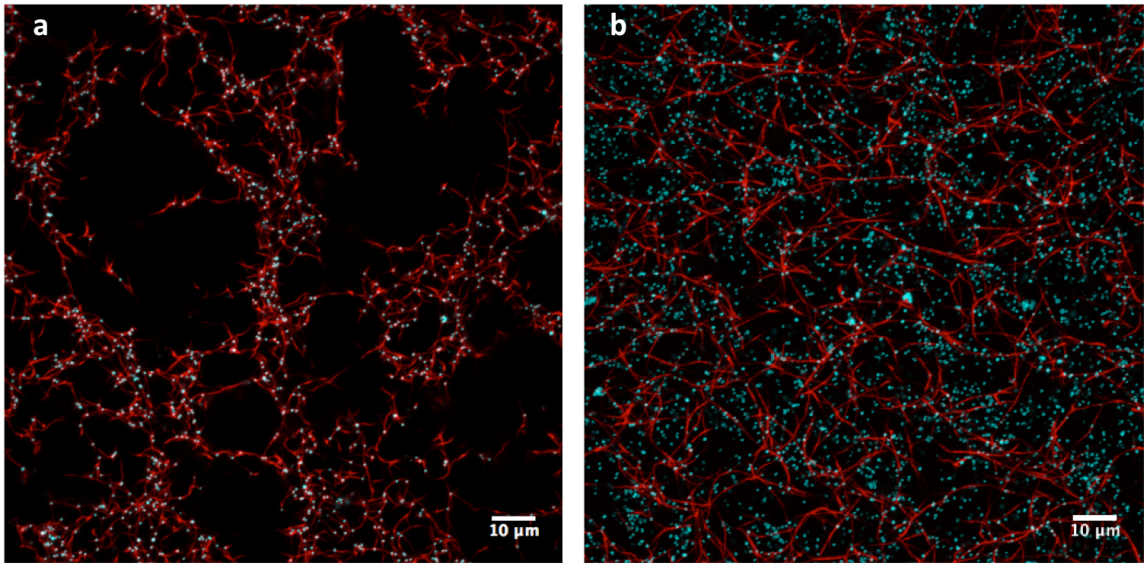

Figure 2-21 | Fibrin Structure influenced by micrometer-scale objects

Axial projections of fibrin formed in the presence of 0.5 µm carboxylate conjugated polystyrene particles incubated in (a) 0.5% bovine serum albumin (BSA) solution for 24 hours; (b) 15% BSA solution for more than a month. Fibrin is red, colloidal particles are light blue. Comparison to Figure 2-9 shows that the fibrin structure in (a) is similar to that of introduced bacteria in terms of the distinct heterogeneity in pore size distribution -- large pores and small pores; however, the fibrin structure in (b) does not have the same structure as Figure 2-9. The zeta-potential of the two particles are -24 ± 2 mV (a) and – 11 ± 6 mV (b), respectively. The results show that particle surface chemistry and surface charge are correlated with the self-assembled fibrin structure.

This fundamental study of the influence of *S. epidermidis* cells on fibrin kinetics, structure and instability simplifies the conditions of physiological clotting so as to directly identify bacterial – fibrin interactions. A recent study under physiological conditions by *Davies et al. (35)* showed that clot structure and mechanics change with the different stages of sepsis. Common features of the two studies are the observed correlation of microstructure and mechanical properties. Our *in vitro* study sheds light on the underlying physical and biochemical mechanisms that link fibrin kinetics with bacterial cells. Future work could address the role that other physiological

constituents – serum proteins and platelets in particular – play in mediating the effect that bacteria has on clot structure and mechanics.

This study addressed the structure, mechanics, and instability of an *in vitro* blood clot model infected by *S.epidermidis* from microscopic and macroscopic perspectives. It has potential clinical implications: the result that *S. epidermidis* cells slow down the fibrin clotting process has potential connections to infection-related hemostatic diseases. The fact that the infected clot which formed in the presence of bacteria exhibits a higher elasticity has implications for embolic diseases which have been correlated with high fibrin rigidity[46,47] – a clinical indicator used to determine the appropriate therapy for venous thrombosis treatment[13,14]. Furthermore, this study presents evidence suggesting that *S. epidermidis* remodels host fibrin network, leading to clot rupture, the detailed kinetics of which could be the subject of future study. This relationship provides insight into the correlation between bacterial infection and thromboembolism. By identifying *S.epidermidis* effects on fibrin networks, it opens up discussion of the interaction mechanisms between bacteria and embolism with potential implications for treating septic thromboembolism. The infected clot model could also be used to study other situations – such as chronic wound healing and scar formation – in which bacteria and clot co-present in the human body.

2.6 Acknowledgement

We thank John G. Younger for early collaboration and project conceptualization. We also thank Usha Kadiyala for the help with taking the scanning electron microscopy image. This work is supported by NIH NIGMS (Grant GM-081702).

2.7 References:

1 Arnold, M. *et al.* Thrombolysis in patients with acute stroke caused by cervical artery dissection: analysis of 9 patients and review of the literature. *Archives of neurology* **59**, 549-553 (2002).

2 Tapson, V. F. Acute pulmonary embolism. *The New England journal of medicine* **358**, 1037-1052, doi:10.1056/NEJMra072753 (2008).

3 Samama, M. M. An epidemiologic study of risk factors for deep vein thrombosis in medical outpatients: the Sirius study. *Archives of internal medicine* **160**, 3415-3420 (2000).

4 Dalager-Pedersen, M. *et al.* Venous thromboembolism after community-acquired bacteraemia: a 20-year danish cohort study. *PLoS One* **9**, e86094, doi:10.1371/journal.pone.0086094 (2014).

5 Grau, A. J. *et al.* Clinical and biochemical analysis in infection-associated stroke. *Stroke; a journal of cerebral circulation* **26**, 1520-1526 (1995).

6 Hall-Stoodley, L., Costerton, J. W. & Stoodley, P. Bacterial biofilms: from the Natural environment to infectious diseases. *Nat Rev Micro* **2**, 95-108 (2004).

7 Raad, II *et al.* The relationship between the thrombotic and infectious complications of central venous catheters. *Jama* **271**, 1014-1016 (1994).

8 Brackman, G., De Meyer, L., Nelis, H. J. & Coenye, T. Biofilm inhibitory and eradicating activity of wound care products against Staphylococcus aureus and Staphylococcus epidermidis biofilms in an in vitro chronic wound model. *Journal of applied microbiology* **114**, 1833-1842, doi:10.1111/jam.12191 (2013).

9 Lordick, F. *et al.* Ultrasound screening for internal jugular vein thrombosis aids the detection of central venous catheter-related infections in patients with haemato-oncological diseases: a prospective observational study. *British journal of haematology* **120**, 1073-1078 (2003).

10 Kim, M. K., Ingremeau, F., Zhao, A., Bassler, B. L. & Stone, H. A. Local and global consequences of flow on bacterial quorum sensing. *Nat Microbiol* **1**, 15005, doi:10.1038/nmicrobiol.2015.5 (2016).

11 Peterson, B. W. *et al.* Viscoelasticity of biofilms and their recalcitrance to mechanical and chemical challenges. *FEMS Microbiol Rev* **39**, 234-245, doi:10.1093/femsre/fuu008 (2015).

12 VanEpps, J. S. & Younger, J. G. Implantable Device-Related Infection. *Shock (Augusta, Ga.)* **46**, 597-608, doi:10.1097/shk.0000000000000692 (2016).

13 Piechocka, I. K., Bacabac, R. G., Potters, M., Mackintosh, F. C. & Koenderink, G. H. Structural hierarchy governs fibrin gel mechanics. *Biophys J* **98**, 2281-2289, doi:10.1016/j.bpj.2010.01.040 (2010).

14 Ryan, E. A., Mockros, L. F., Weisel, J. W. & Lorand, L. Structural origins of fibrin clot rheology. *Biophysical Journal* **77**, 2813-2826 (1999).

15 Weisel, J. W. Structure of fibrin: impact on clot stability. *Journal of Thrombosis and Haemostasis* **5**, 116-124, doi:10.1111/j.1538-7836.2007.02504.x (2007).

16 Janmey, P. A., Winer, J. P. & Weisel, J. W. Fibrin gels and their clinical and bioengineering applications. *J R Soc Interface* **6**, 1-10, doi:10.1098/rsif.2008.0327 (2009).

17 Otto, M. Staphylococcus epidermidis--the 'accidental' pathogen. *Nat Rev Microbiol* **7**, 555-567, doi:10.1038/nrmicro2182 (2009).

18 McCann, M. T., Gilmore, B. F. & Gorman, S. P. Staphylococcus epidermidis device-related infections: pathogenesis and clinical management. *The Journal of pharmacy and pharmacology* **60**, 1551-1571, doi:10.1211/jpp.60.12.0001 (2008).

19 Wisplinghoff, H. *et al.* Nosocomial bloodstream infections in US hospitals: analysis of 24,179 cases from a prospective nationwide surveillance study. *Clinical infectious diseases : an official publication of the Infectious Diseases Society of America* **39**, 309-317, doi:10.1086/421946 (2004).

20 Prasad, J. M. *et al.* Mice expressing a mutant form of fibrinogen that cannot support fibrin formation exhibit compromised antimicrobial host defense. *Blood* **126**, 2047-2058, doi:10.1182/blood-2015-04-639849 (2015).

21 Loof, T. G. *et al.* Staphylococcus aureus-induced clotting of plasma is an immune evasion mechanism for persistence within the fibrin network. *Microbiology* **161**, 621-627, doi:10.1099/mic.0.000019 (2015).

22 Lungren, M. P. *et al.* Bacteriophage K antimicrobial-lock technique for treatment of Staphylococcus aureus central venous catheter-related infection: a leporine model efficacy analysis. *J Vasc Interv Radiol* **25**, 1627-1632, doi:10.1016/j.jvir.2014.06.009 (2014).

23 Whiting, D. & DiNardo, J. A. TEG and ROTEM: Technology and clinical applications. *American Journal of Hematology* **89**, 228-232, doi:10.1002/ajh.23599 (2014).

24 Evans, P. A. *et al.* Rheometry and associated techniques for blood coagulation studies. *Medical engineering & physics* **30**, 671-679, doi:10.1016/j.medengphy.2007.08.005 (2008).

25 Collet, J.-P., Shuman, H., Ledger, R. E., Lee, S. & Weisel, J. W. The elasticity of an individual fibrin fiber in a clot. *Proceedings of the National Academy of Sciences of the United States of America* **102**, 9133-9137, doi:10.1073/pnas.0504120102 (2005).

26 Bendix, P. M. *et al.* A Quantitative Analysis of Contractility in Active Cytoskeletal Protein Networks. *Biophysical Journal* **94**, 3126-3136, doi:10.1529/biophysj.107.117960 (2008).

27 Utada, A. S. *et al.* Vibrio cholerae use pili and flagella synergistically to effect motility switching and conditional surface attachment. *Nat Commun* **5**, 4913, doi:10.1038/ncomms5913 (2014).

28 Valentine, M. T. *et al.* Colloid Surface Chemistry Critically Affects Multiple Particle Tracking Measurements of Biomaterials. *Biophysical Journal* **86**, 4004-4014, doi:10.1529/biophysj.103.037812 (2004).

29 Billings, N., Birjiniuk, A., Samad, T. S., Doyle, P. S. & Ribbeck, K. Material properties of biofilms-a review of methods for understanding permeability and mechanics. *Rep Prog Phys* **78**, 036601, doi:10.1088/0034-4885/78/3/036601 (2015).

30 Savin, T. & Doyle, P. S. Static and dynamic errors in particle tracking microrheology. *Biophys J* **88**, 623-638, doi:10.1529/biophysj.104.042457 (2005).

31 Stewart, E. J., Ganesan, M., Younger, J. G. & Solomon, M. J. Artificial biofilms establish the role of matrix interactions in staphylococcal biofilm assembly and disassembly. *Sci Rep* **5**, 13081, doi:10.1038/srep13081 (2015).

32 Squires, T. M. & Mason, T. G. Fluid Mechanics of Microrheology. *Annual Review of Fluid Mechanics* **42**, 413-438, doi:doi:10.1146/annurev-fluid-121108-145608 (2010).

33 Squires, T. M. & Mason, T. G. Fluid Mechanics of Microrheology. *Annual Review of Fluid Mechanics* **42**, 413-438, doi:10.1146/annurev-fluid-121108-145608 (2009).

34 Michaelis, L., Menten, M. L., Johnson, K. A. & Goody, R. S. The original Michaelis constant: translation of the 1913 Michaelis-Menten paper. *Biochemistry* **50**, 8264-8269, doi:10.1021/bi201284u (2011).

35 Mommaerts, W. F. H. M. ON THE NATURE OF FORCES OPERATING IN BLOOD CLOTTING : II. THE CLOTTING OF FIBRINOGEN AS A TWO-STEP REACTION. *The Journal of General Physiology* **29**, 113-122 (1945).

36 McGuffie, M. J. *et al.* Zinc oxide nanoparticle suspensions and layer-by-layer coatings inhibit staphylococcal growth. *Nanomedicine : nanotechnology, biology, and medicine* **12**, 33-42, doi:10.1016/j.nano.2015.10.002 (2016).

37 Fischer, H., Polikarpov, I. & Craievich, A. F. Average protein density is a molecular-weight-dependent function. *Protein Science : A Publication of the Protein Society* **13**, 2825-2828, doi:10.1110/ps.04688204 (2004).

38 Brown, S., Santa Maria, J. P., Jr. & Walker, S. Wall teichoic acids of gram-positive bacteria. *Annu Rev Microbiol* **67**, 313-336, doi:10.1146/annurev-micro-092412-155620 (2013).

39 Weidenmaier, C. & Peschel, A. Teichoic acids and related cell-wall glycopolymers in Gram-positive physiology and host interactions. *Nat Rev Microbiol* **6**, 276-287, doi:10.1038/nrmicro1861 (2008).

40 Tennent, G. A. *et al.* Human plasma fibrinogen is synthesized in the liver. *Blood* **109**, 1971-1974, doi:10.1182/blood-2006-08-040956 (2007).

41 Davies, G. R. *et al.* The effect of sepsis and its inflammatory response on mechanical clot characteristics: a prospective observational study. *Intensive care medicine* **42**, 1990-1998, doi:10.1007/s00134-016-4496-z (2016).

42 van Kempen, T. H., Bogaerds, A. C., Peters, G. W. & van de Vosse, F. N. A constitutive model for a maturing fibrin network. *Biophys J* **107**, 504-513, doi:10.1016/j.bpj.2014.05.035 (2014).

43 MacKintosh, F. C., Kas, J. & Janmey, P. A. Elasticity of semiflexible biopolymer networks. *Phys Rev Lett* **75**, 4425-4428, doi:10.1103/PhysRevLett.75.4425 (1995).

44 Liu, W., Carlisle, C. R., Sparks, E. A. & Guthold, M. The mechanical properties of single fibrin fibers. *Journal of thrombosis and haemostasis : JTH* **8**, 1030-1036, doi:10.1111/j.1538-7836.2010.03745.x (2010).

45 Bharadwaj, N. A. *et al.* Integration of colloids into a semi-flexible network of fibrin. *Soft Matter* **13**, 1430-1443, doi:10.1039/c6sm02141g (2017).

46 Collet, J. P. *et al.* Dusart syndrome: a new concept of the relationship between fibrin clot architecture and fibrin clot degradability: hypofibrinolysis related to an abnormal clot structure. *Blood* **82**, 2462-2469 (1993).

47 Collet, J. P. *et al.* Influence of fibrin network conformation and fibrin fiber diameter on fibrinolysis speed: dynamic and structural approaches by confocal microscopy. *Arterioscler Thromb Vasc Biol* **20**, 1354-1361 (2000).

Chapter 3: Growth-dependent bacteria-fibrinogen interaction and infected fibrin formation[2]

3.1 Abstract:

Bacterial infection and thrombosis are highly correlated, especially in patients with medical device implants. Attention has been drawn to the interaction between bacteria and host protein, specifically fibrinogen and fibrin. However, little is know regarding the impact of the bacterial change from planktonic to biofilm-like phenotype on this interaction. Here we investigate on the growth phase dependent bacteria-fibrinogen interaction and bacterial effect on fibrin formation, structure and mechanics. Furthermore, this difference is mediated by increased adhesion to fibrinogen. Flow cytometry is applied to study the growth-phase dependent bacterial affinity for fibrinogen. A functional *in vitro* model was developed to evaluate adhesion of *S. epidermidis* to a fibrinogen coated surface in a continuously flowing environment. The bacterial deposition rate onto fibrinogen and residence time on the surface were both significantly greater for stationary phase as compared to exponential phase. Furthermore, the gene expression for SdrG – the protein that adheres *S. epidermidis* cells to fibrinogen was significantly increased in the stationary phase. Rheometry and confocal microscopy were used to show that stationary phase bacterial cells have a more robust effect on fibrin formation, structure and mechanics. We speculate that the stronger interaction between stationary phase bacterial cells and fibrinogen could cause the more robust

[2] The work of Chapter 3 is in preparation of publication as "Growth-dependent bacteria-fibrinogen interaction and infected fibrin formation*"* by **Tianhui Ma**, Carolyn Vitale, Janice Sim, Erika Martinez-Nieves, Michael Solomon, and J. Scott VanEpps

effect on fibrin. It contributes to the current understanding of the growth phase dependent regulation of bacterial virulent factors and the correlation between bacterial infection and thrombosis.

3.2 Introduction:

Pathologic clots, for example, venous thromboembolism and embolic cerebrovascular accidents, are highly correlated with bacterial infection(1-4). Clinically, thrombosis and bacterial biofilms often appear simultaneously, especially on implanted medical devices(1, 5). One study showed that 12 of 14 patients with central venous catheter (CVC) related infection had a preceding CVC related venous thrombosis (6) and a relative risk of thrombosis is assigned to the presence of infection (7). One of the mechanisms to explain such correlation is that clotting proteins provide a substrate for bacterial adherence with microbial receptor-specific binding to fibrinogen and its cleaved product fibrin. Specifically, *Staphyloccocus epidermidis* has a well described surface protein called SdrG which binds fibrinogen in a "lock, dock and latch" mechanism (8-11). Given its specific binding of the coagulation protein fibrinogen, SdrG is a plausible key protein mediating the interaction between infection and thrombosis.

A biofilm is a bacterial community that occurs when bacteria attach to a surface, alter their phenotype and produce a protective layer of extracellular polymeric substance (EPS). A significant cause of clinical infections, biofilms present a significant obstacle to host immune defense, mechanical debridement, and treatment with traditional antimicrobials(12) The most commonly recognized biofilm infections are those related to indwelling medical devices(13). The life cycle of a biofilm begins when bacteria adhere to a surface followed by an initially period of exponential growth and EPS production. Once the biofilm becomes densely populated and encased in EPS, the bacteria slow their growth to a stationary phase. Finally, some of the bacteria detach as planktonic (*i.e.*, free floating) bacteria to attach and start a new biofilm colony elsewhere. Each phase of the life cycle requires specific protein machinery to be most effective and the bacteria display phenotypic changes as they progress from planktonic to biofilm

phenotype. While the change in phenotype is key in biofilm formation, little is known about the impact of these changes on the bacteria-host protein interaction, specifically fibrinogen.

Staphylococcus epidermidis, a ubiquitous commensal colonizer of human skin, belongs to the group of coagulase negative Staphylococcal species which are the leading cause of device related infection, endocarditis and surgical site infections (14, 15). Device related infections, particularly central line associated bloodstream infections increase mortality, medical cost and hospital length of stay (16, 17).

Previous work from our lab showed that not only bacteria adhere to fibrin clots, their presence also influence the clot microstructure and mechanics in a way that has implications for bacterial induced thromboembolism (18). The goal of this research is to explore the phenotypic differences between stationary and exponential phase bacteria in the scope of their interactions with fibrinogen and their impact on thrombus characteristics, specifically fibrin formation, structure and mechanics. We first applied flow cytometry to characterize the growth-phase dependent bacterial affinity for fibrinogen. We then evaluated phase dependent *S.epidermidis* affinity for fibrinogen in solution and separately the surface based deposition of bacteria onto fibrinogen in a continuously flowing model mimicking blood flow. Next, we compared phase differences in gene expression of bacterial cell surface proteins with potential impact on adhesion and interaction with host coagulation proteins. We performed rheology and evaluated structure of *S. epidermidis* infected fibrin clots.

3.3 Materials and methods:

3.3.1 Bacterial strains and culture:

S. epidermidis strain RP62A, a pathogenic strain which forms biofilms, was used for all experiments. Loop inoculates from frozen glycerol stock (-80°C) were grown on Tryptic Soy Agar (TSA, Fisher Scientific) plates for at least 16 hours at 37°C. A single colony was selected and cultured in Tryptic Soy Broth with glucose 1% (TSBG) at 37°C under agitation at 200-250 rpm. Exponential phase growth was defined as an optical density of 0.4 ± 0.1 measured at 600 nm. A 30 mL sample of culture was removed and left undisturbed for 30 -60min at room temperature to allow for settling of flocculated cells. For the model of bacterial deposition onto fibrinogen mimicking medical device infection and the flow cytometry experiment, the culture was returned to incubator at 37°C to continue growth under agitation until optical density of 1.4 (± 0.05) at 600 nm which defined stationary phase growth. For the rheometry experiments, a separate culture was grown to the stationary phase growth as defined previously.

3.3.2 Quantification of surface fibrinogen by flow cytometry:

S. epidermidis were cultured to exponential and stationary phase growth as defined and described above. Cell density was quantified in each sample with Incyto Hemacytometer (Thermo Fisher Scientific, Waltham, MA, USA) and cells were centrifuged into a pellet at 5000 xg for 3 minutes. Supernatant was discarded, and pelleted cells were diluted to concentration of $2x10^9$ cells/mL. Two conditions were prepared in triplicate for each culture—control and labeled fibrinogen. Control sample and labeled fibrinogen pellets were resuspended in Hank's Buffered Salt solution 1X (with Calcium, Magnesium, no phenol red, 1g/L D-Glucose, Thermo Fisher Scientific, Waltham, MA, USA . Fluorescently labeled fibrinogen (Alexafluor 647 Fibrinogen, 650/668nm,

Thermo Fisher Scientific, Waltham, MA, USA) was added to each sample for final concentration of 0.5 mg/mL and incubated for 15 minutes. Cells were then analyzed by flow cytometry (Cytoflex, Beckman). Mean fluorescence was determined as a surrogate for total fibrinogen concentration on the cell surface using FCS Express (Denovo). A total of 9 experiments were completed in triplicate with the mean from each experiment used for analysis. Statistical analyses was performed with Wilcoxon paired signed rank test with significance defined as $p < 0.05$.

3.3.3 Bacterial adhesion to fibrinogen in continuously flowing environment:

Fibrinogen (Fg) from human plasma (EMD Millipore Corporation, Billerica, MA, USA) was reconstituted as directed and stored at -80°C in aliquots. Frozen aliquots were thawed and diluted to concentration of 10 μg/mL using sterile distilled water. Glass coverslips were coated with fibrinogen for 4 hours at 20°C, blocked with 1% bovine serum albumin for 1 hour followed by three washes with normal saline.

The stationary phase sample was diluted with normal saline to match optical density of the exponential phase culture then left undisturbed at 20°C for one hour. Exponential stationary phase cells were fluorescently labeled with Syto 9 (Thermo Fisher Scientific, Waltham, MA, USA). Cells were loaded into a 10 mL syringe on a standard syringe pump (Harvard Apparatus). Fibrinogen coated glass coverslips were constructed into a parallel plate flow chamber (Harvard Apparatus). Cell suspensions were infused at a rate of 125 μL/min through parallel plate flow chamber mounted on a epifluorescent microscope with high speed microvideography capabilities. Images were captured every 3 seconds for 30 minutes. A total of 10 experiments

were completed in duplicate and the mean for each experiment was used. Image analysis was completed in MATLAB. A new adhesion event was defined as the new appearance of a bacteria which persisted for two or more images in a single location. Residence time was defined as the total time a signle bacteria persisted at a single location. Wilcoxon signed-rank test was used for nonparametric hypothesis testing comparing deposition rate, expressed as cells/cm^2 s versus growth phase. For residence time, a Kruskal-Wallis test was used to compare the population of bacteria persisting for greater than 500 seconds for each growth phase with significance defined as $p < 0.001$.

3.3.4 Gene expression changes from exponential to stationary phase:

RNA was extracted from *S. epidermidis* grown to either exponential or stationary phase as described above. One mL of liquid bacterial cultures was grown to centrifuged at 8000 rpm for 1 minute to pellet the cells. After washing with RNase free water, cells were resuspended. Cell lysis was achieved with 5 µl lysostaphin (2ug/µl), incubation at 37°C for 45min to an hour followed by addition of 75µl TRIzol and vigorous pipetting. Samples were vortexed and then centrifuged at 12000 rpm for 10 minutes at 4°C. Supernatant was removed and incubated at room temperature for 5 minutes. Chloroform (15µl) was added to the sample, vortexed for 15 seconds, and incubated at room temperature for 3 minutes. Following this, samples were centrifuged at 12000 rpm for 15 minutes at 4°C. The aqueous phase was isolated and transferred to using the RNeasy Mini Kit spin columns (Qiagen) and RNA was purified per the manufacturer's instructions. High quality RNA yield was confirmed by UV spectrophotometry and Bioanalyzer. Samples were stored at -80°C.QuantiTect Probe RT-PCR (Qiagen) was utilized in 50 µl reactions. The reaction mixture contained 25 µl 2x Probe RT-PCR Master Mix, 0.5 µl

RT Mix, 5 µl of Exponential Phase or Stationary Phase (Ep/Sp) RNA template (5 ng), and 5 µl of each gene forward/reverse-primer (F/R-primer, 1 uM) and probe-primer (0.2 uM); finally, amplification mixture was set to 50 µl by adding 4.5 µl of RNase-free water. The RT-PCR Master Mix contained HotStarTaq DNA polymerase, ROX reference dye, dNTP mix, and RT-PCR buffer (Tris-Cl, KCl, (NH4)SO4, 8 mM MgCl2, at pH 8.7). Thermal cycling protocol began with 30 minutes in the reverse transcription step at 50°C, followed by an initial activation step of 15 minutes at 95°C, denaturation of 15 seconds at 94°C, and combined annealing/extension step at 65°C for 60 seconds for a total of 45 cycles.

3.3.5 Mechanics and microstructure measurements of fibrin clots:

Materials and constitution methods are described in previously published work (18). Briefly, Citrate-free thrombin from human plasma and fibrinogen (Fg) from human plasma were purchased from EMD Millipore (Billerica, MA). Fibrinogen solutions (0.5mg/ml) were made by diluting the stock solution with Hank's Balanced Salt Solution at 37°C. Clot was initiated by adding thrombin (0.5U/ml as final concentration).

Clot elasticity was characterized by measuring the linear elastic modulus, G', on a mechanical rheometer (TA Instruments AR-G2, cone and plate fixture with a 2° cone angle and a 40 mm diameter); clot microstructures were observed using a Nikon A1Rsi confocal laser scanning microscope with a 100x, 1.45 NA, oil immersion objective and images were analyzed to determine mesh size using Matlab as we have previously described (18). The steady state of fibrin structures is defined as those that are 50 – 90min from the initiation of clot formation as explained in our previous work (18). Bacteria concentration for both exponential and stationary phase were 4×10^9 cells/ml to match the in vivo biofilm concentration.

3.4 Results:

3.4.1 Stationary phase *S. epidermidis* cell surface binds more fibrinogen

Figure 3-1a shows an example of a single experiment with exponential phase in black and stationary phase in red. The fluorescence of stationary phase is higher than exponential phase with a similar distribution. Composite mean fluorescence index of all experiments (n= 9 in triplicate) is shown in Figure 3-1b. The mean fluorescence of stationary phase bacteria incubated with fluorescently labeled fibrinogen was significantly higher as compared to exponential phase bacteria under the same condition (3642 ± 349 vs 6388 ± 919, n=10, p = 0.004) as seen in Figure 3-1b.

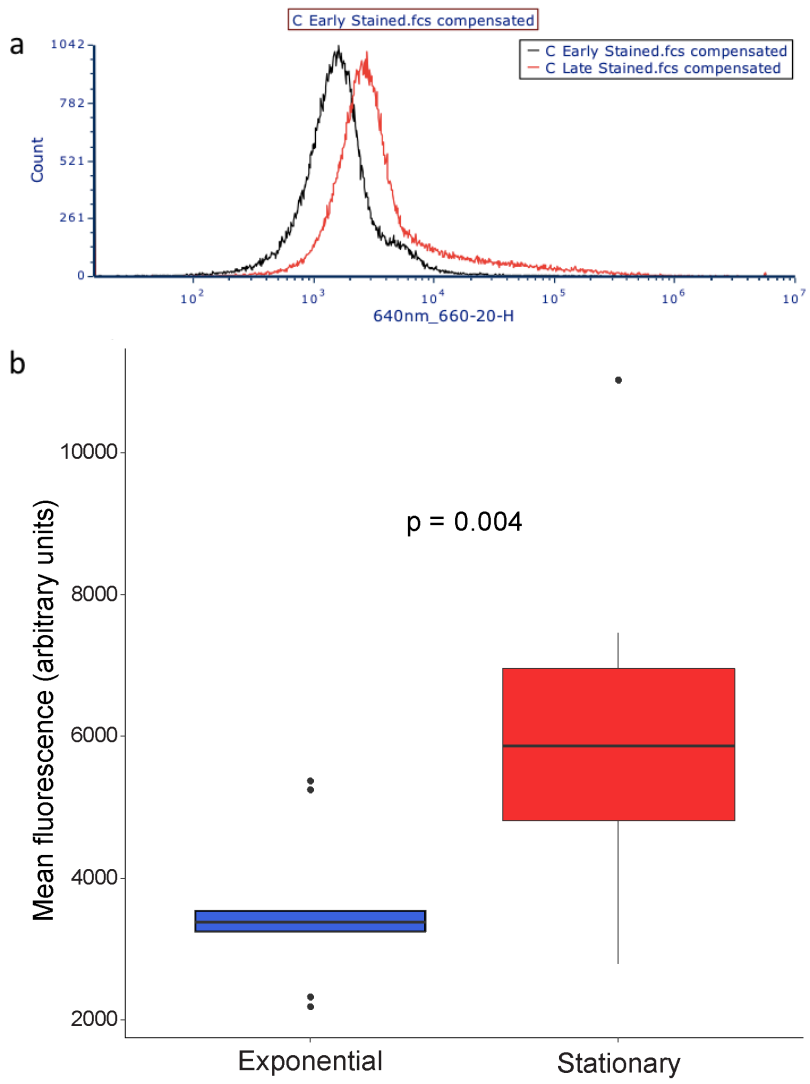

Figure 3-1 | Flow cytometry of bacteria incubated with fluorescently labeled fibrinogen

(a) Example of single experiment with fluorescence versus event count. (b) Mean fluorescence of S. epidermidis in exponential phase versus stationary phase growth with a bacterial cell concentration of 4×10^9cells/ml and fibrin concentration of 0.5mg/ml. n = 9 of paired experiments in triplicate. Data was collected by Carolyn Vitale.

3.4.2 Stationary phase *S. epidermidis* cells has a stronger attraction to fibrinogen

Fluorescent labeled bacteria were visualized in image capture flowing past immobilized fibrinogen (Figure 3-2a-e), appearing as streaks on image capture but clearly defined circular shape as they slow and rest on the surface. Persistence of a bacteria in a single location for

multiple images defined an adhesion event (white box in Figure 3-2b-d) while subsequent absence of an adhered bacteria (white box Figure 3-2f) defined a release event and the total time spent adhered was defined as residence time. The deposition rate of bacterial cells on immobilized fibrinogen showed a steady, linear relationship for both exponential and stationary phase bacteria (Figure 3-2f); however, the deposition rate of stationary phase cells was significantly greater than the deposition rate of cells in exponential phase (5360 ± 1776 vs 2212 ± 264, n=10, $p < 0.05$) (Figure 3-2g). Additionally, stationary phase bacteria showed a significantly longer residence time when compared to exponential phase cells (Figure 3-2h). Most notably there was a population of stationary phase cells that had a residence time of greater than 500 seconds, skewing the distribution to the right as compared to the exponential phase bacteria. That is, only 2.7% of exponential cells had a residence time of greater than 500 seconds while 13.1% of the stationary phase cell had a residence time greater than 500 seconds. This difference is also significant (Chi-squared, $p<0.001$).

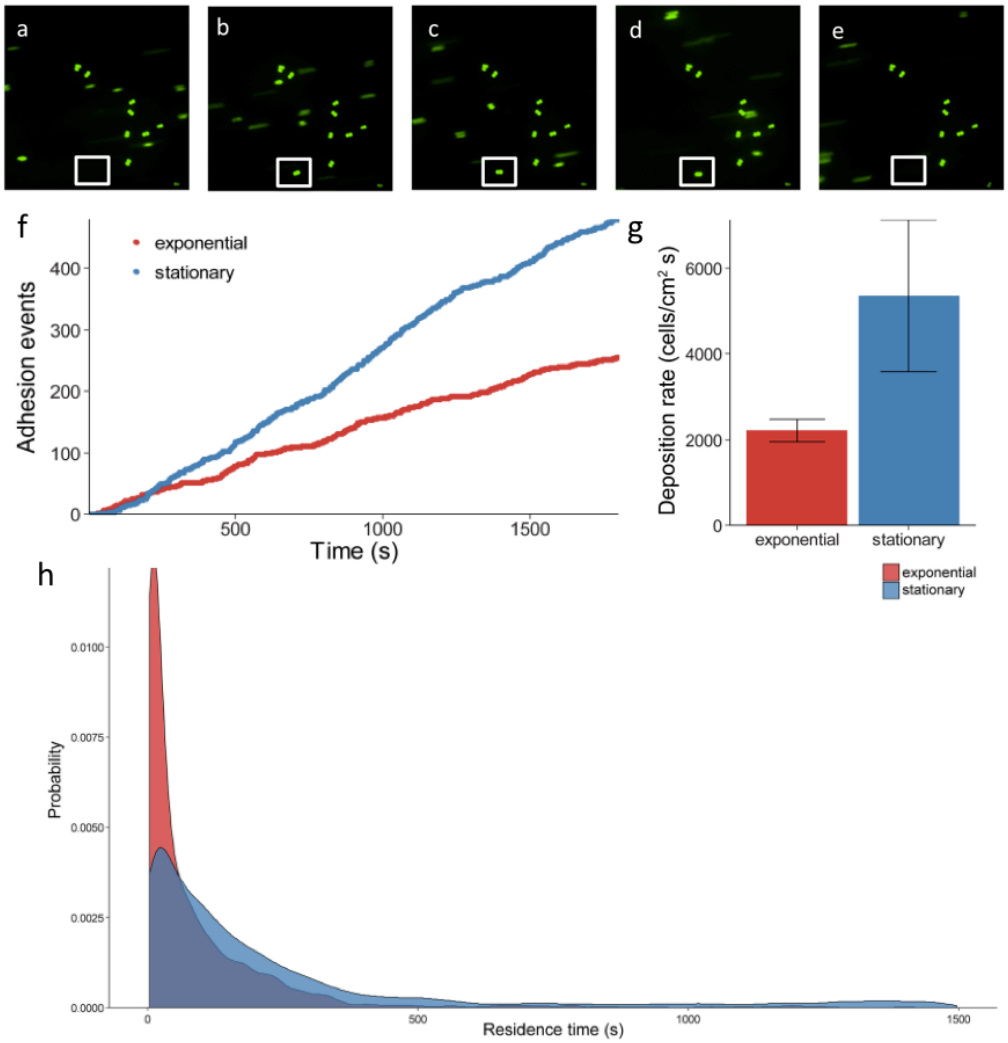

Figure 3-2 | Adhesion of S. epidermidis to a fibrinogen coated surface under a continuously flowing environment

(a-e) Images captured 3 seconds apart of fluorescently labeled fibrinogen (green) with absence of bacteria in white frame in (a), adhesion in frames (b-d) and absence in (e) representing a release event. Time between frames (b) to (e) represents the residence time of that single bacteria. (f) Graphical representation of a single experiment of adhesion events over time with exponential phase bacteria (red) versus stationary phase (blue). (g) Adhesion rate of exponential phase (red) versus stationary phase (blue) *S. epidermidis* with n = 10 of paired experiments in duplicate. (h) Residence time of exponential phase (red) versus stationary phase (blue) *S. epidermidis* with n = 10 of paired experiments in duplicate. Data was collected by Carolyn Vitale.

3.4.3 Stationary phase *S. epidermidis* cells express more fibrinogen-binding proteins

The RNA expression of SdrG (2.16 ± 0.91) and Sspa (3.43 ± 1.83), described in fold-change in stationary phase compared to exponential phase bacteria, were significantly elevated in stationary phase bacteria as compared to the expression in exponential phase bacteria (Figure 3-3). The expression of Aap (2.15 ± 1.1), Atle (1.11 ± 0.65), Ica (1.62 ± 0.85) and SdrF (1.21 ± 0.83) all showed non-significant increase in expression in stationary phase bacteria. There was a significant decrease in IcaR (0.743 ± 0.15) expression in stationary phase as compared to exponential phase bacteria. Analysis done with a paired t-test with Bonferroni correction for multiple comparisons. $p<0.05$ indicated by *.

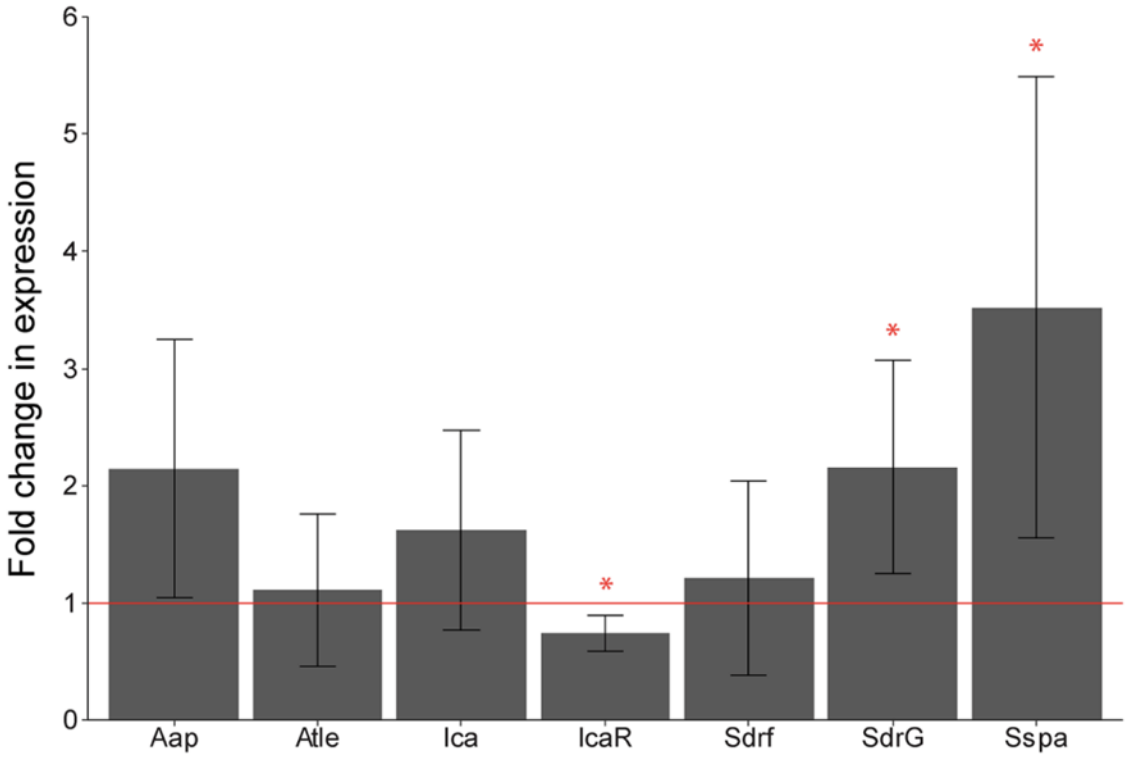

Protein	Function
AtlE	Cell adhesion to abiotic surfaces
Sspa	Degrades fibrinogen and C5
SdrF	Adhesion to collagen
ica	Cell-cell adhesion
aap	Cell-cell adhesion
SdrG	Adhesion to fibrinogen

Figure 3-3 | RT-PCR of S. epidermidis proteins

(a) Fold change in expression of stationary phase bacteria as compared to exponential phase bacteria. Error bars represent standard error of the mean with n = 7. RNA samples were extracted by Janice Sim and RT-PCT was performed by Erika Martinez-Nieves. (b) *S. epidermidis* proteins and their function.

3.4.4 The mechanical and structural effect of S. epidermidis on fibrin clots growth-phase dependent

The elasticity of a pure fibrin clot (0.5 mg/ml fibrinogen) without bacterial cells increases rapidly and reaches a steady-state value of 1.5 ± 0.2 Pa in ~40 min (Figure 3-4a). The addition of stationary phase bacterial cells has a significant effect on the kinetics of the fibrin clot elastic response: Clot formation is initially retarded and has a transient plateau at a modulus value less than the steady-state modulus of the pure fibrin clot. Then the elastic modulus rapidly increases to a second steady-state value ~4 times greater than that of the pure fibrin clot. Contrarily, the addition of the exponential phase bacterial cells of the same cell concentration has a less significant effect on fibrin kinetics. Initially, the process is also retarded but it then reaches its final plateau at a modulus value lower than that of the pure fibrin.

Figure 3-4b and c compare the steady-state structure (c.f. Methods) of the corresponding conditions with the fibrin elasticity measurements. The pure fibrin network has a homogeneous pore size distribution. The pure fibrin mesh size (c.f. Methods) – the average distance between fibers – is 5.9±1.1 μm (Figure 3-4c), consistent with previous measurements in the literature(19). On the other hand, the network formed in the presence of stationary phase *S. epidermidis* is heterogeneous with two characteristic mesh size as reported by our group previously (18). However, the fibrin network structure formed in the presence of exponential phase bacterial cells (7.1 ± 1.5 μm) remains homogeneous and the mesh size becomes larger than the pure fibrin ($p < 0.001$). The exponential phase bacterial cells are visualized in the voids of the fibrin network.

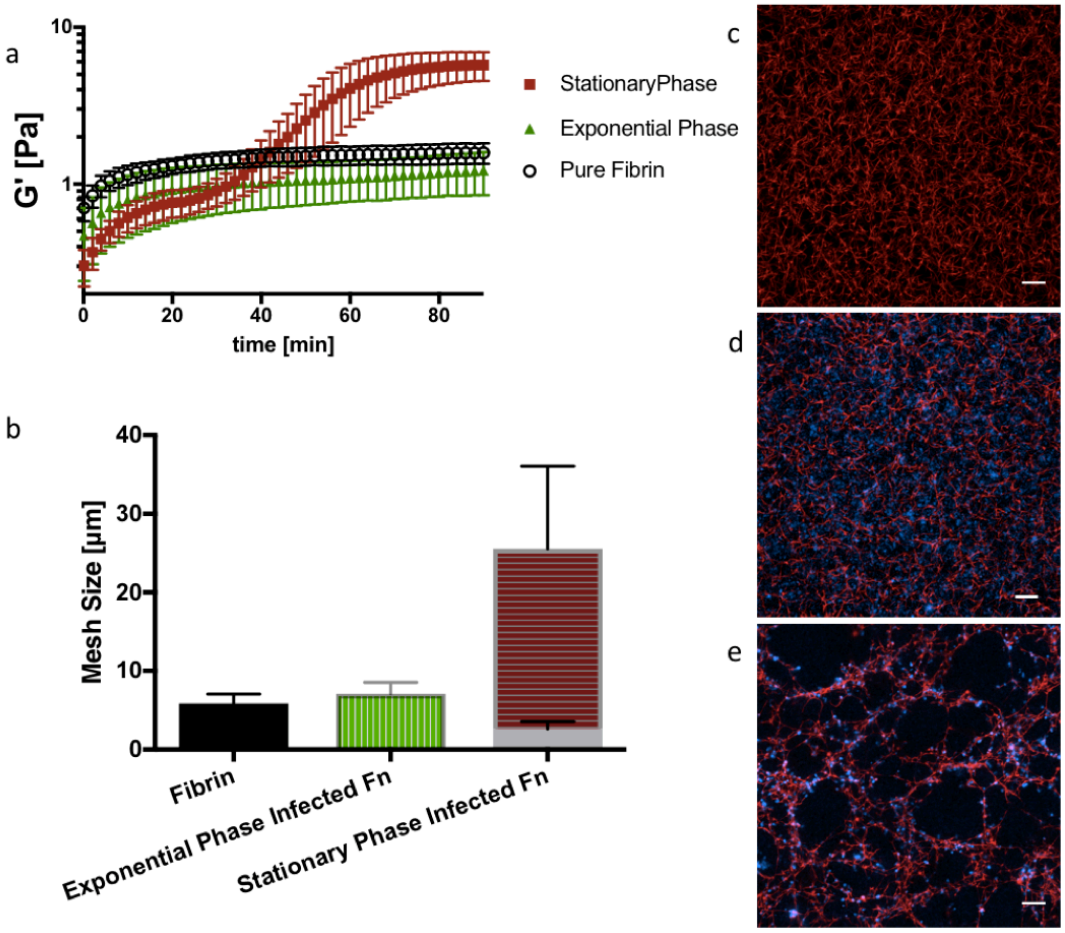

Figure 3-4 | Stationary Phase *S. epidermidis* Alters Fibrin Elasticity and Structure

(a) Time sweep of elastic modulus, G', of pure fibrin clot (0.5mg/ml) (black) and fibrin clots infected by stationary phase bacterial cells (red), exponential phase bacterial cells (green) and stationary phase bacterial cells incubated with BSA (orange) (0.5mg/ml fibrin with 4×10^9cells/ml). Error bars denote standard deviation with n=3. (b) Mesh size characterization of steady state pure fibrin clot and infected fibrin clot. Error bars denote standard deviations of all the image stacks in all five replicates (c.f. Methods). Scale bar = 10µm. (c) Axial projections of a pure fibrin clot, (d) a fibrin clot infected with exponential phase bacterial cells. Images were collected by Janice Sim. (e) Stationary phase bacterial cells and (f) Stationary phase bacterial cells incubated with BSA. Bacterial cell concentrations are all 4×10^9cells/ml and fibrin concentration is 0.5mg/ml. Fibrin is red and bacterial cells are blue.

3.5 Discussion:

This study demonstrates the growth phase dependent bacterial fibrinogen interactions. We further elucidated the growth phase dependent effect of bacteria on fibrin formation, mechanics and structure. Specifically, *S.epidermidis* in its stationary phase expresses more SdrG, has increased affinity for fibrinogen, adheres more and for a longer duration to a fibrinogen coated surface and generates a heterogeneous fibrin clot network structure that is four times higher in stiffness; on the contrary, *S.epidermidis* in its exponential phase expresses less SdrG, has a lower fibrinogen affinity, with less adhesion to a fibrinogen coated surface and does not have a significant influence on fibrin clot structure and mechanics. Here in the discussion, we especially consider the possible explanations of the correlation between fibrinogen attachment to cells and the influence of cells on fibrin formation.

In our previous work, the heterogeneous structure in Figure 3-4(b,c) has been linked to the higher stiffness (G') in Figure 3-4(a) via microrheology. Thus, the stationary phase *S.epidermidis* cells generate a heterogeneous fibrin structure with higher stiffness while a fibrin forms at the presence of the exponential phase *S.epidermidis* cells has a homogeneous pore size distribution like a pure fibrin and with a stiffness no larger than pure fibrin. In Figure 3-5, we demonstrate the idea of how strong attraction between cells and fibrinogen could lead to the formation of a heterogeneous fibrin network structure. With bacterial cells that strongly attract fibrinogen, the originally evenly distributed fibrinogen molecules can have an increased concentration around cells, thus, a heterogeneous distribution of fibrinogen, which would finally lead to a heterogeneous fibrin network structure. Specially since stationary phase *S.epidermidis* cells slow down the fibrin formation kinetics as described in our previous work (Figure 3-4 and 3-5), the described fibrinogen re-distribution process has around 30 minutes to complete (18) which could

generate a significant enough heterogeneous fibrinogen distribution leading to a final heterogeneous fibrin network structure, therefore, higher fibrin stiffenss.

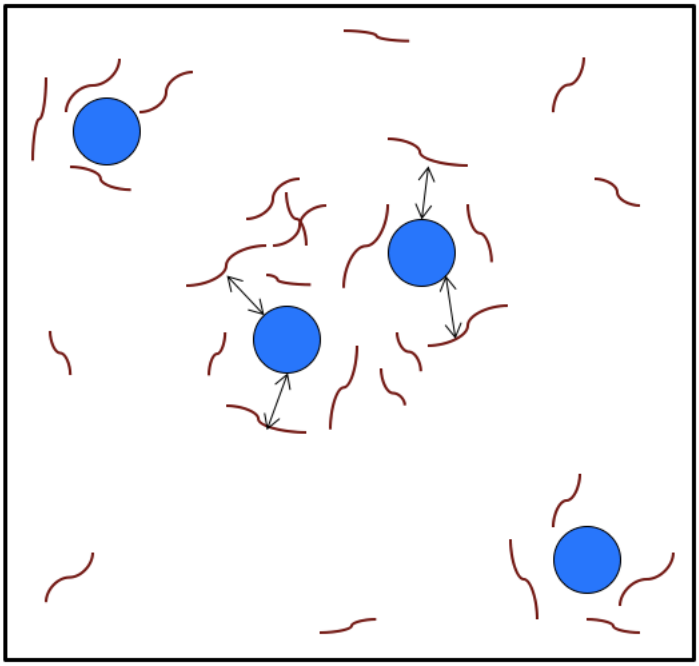

Figure 3-5 | A sketch of the hypothesized mechanism for the noticed phenomena in Figure 3-4

When bacterial cells (blue circles) are sticky to fibrinogen (red lines), the attraction between cells and fibrinogen may generate a heterogeneous fibrinogen distribution that may result in a final heterogeneous fibrin network structure.

Then increase in SdrG expression in the stationary phase S.epidermidis cells could explain the stronger interaction between the stationary phase cells and fibrinogen. In the meanwhile, bacterial cell can also bind fibrinogen via non-specific binding. Furthermore, in our experimental system, fibrinogen is not the only molecule bacterial cells can interact with: thrombin, the enzyme that cleaves fibrinogen and initiates the fibrin polymerization, is also positively charged and can be attracted to bacterial cell wall. Thus, bacteria-fibrinogen attraction may not be the only cause of the fibrin heterogeneous structure. Similarly, bacteria-thrombin attraction could

also generate a heterogeneous distribution of thrombin, and therefore, leads to a heterogeneous fibrin polymerization.

In conclusion, this study demonstrates the growth phase dependent interaction between *S.epidermidis* fibrinogen and effect of *S.epidermidis* on fibrin formation, structure and mechanics. It contributes to the current understanding of growth phase dependent regulation of *S.epidermidis* virulence factors and the association between bacterial infection and thrombosis. It also shines lights on future pharmaceutical solutions to infection-induced thromboembolism.

3.6 References:

1. Raad II, Luna M, Khalil SA, Costerton JW, Lam C, Bodey GP. The relationship between the thrombotic and infectious complications of central venous catheters. Jama. 1994;271(13):1014-6.

2. Samama MM. An epidemiologic study of risk factors for deep vein thrombosis in medical outpatients: the Sirius study. Archives of internal medicine. 2000;160(22):3415-20.

3. Dalager-Pedersen M, Søgaard M, Schønheyder HC, Thomsen RW, Baron JA, Nielsen H. Venous thromboembolism after community-acquired bacteraemia: a 20-year danish cohort study. PLoS One. 2014;9(1):e86094.

4. Grau AJ, Buggle F, Steichen-Wiehn C, Heindl S, Banerjee T, Seitz R, et al. Clinical and biochemical analysis in infection-associated stroke. Stroke. 1995;26(9):1520-6.

5. Brackman G, De Meyer L, Nelis HJ, Coenye T. Biofilm inhibitory and eradicating activity of wound care products against Staphylococcus aureus and Staphylococcus epidermidis biofilms in an in vitro chronic wound model. J Appl Microbiol. 2013;114(6):1833-42.

6. Lordick F, Hentrich M, Decker T, Hennig M, Pohlmann H, Hartenstein R, et al. Ultrasound screening for internal jugular vein thrombosis aids the detection of central venous catheter-related infections in patients with haemato-oncological diseases: a prospective observational study. Br J Haematol. 2003;120(6):1073-8.

7. VanEpps JS, Younger JG. Implantable Device-Related Infection. Shock. 2016;46(6):597-608.

8. Davis SL, Gurusiddappa S, McCrea KW, Perkins S, Höök M. SdrG, a fibrinogen-binding bacterial adhesin of the microbial surface components recognizing adhesive matrix molecules subfamily from Staphylococcus epidermidis, targets the thrombin cleavage site in the Bbeta chain. The Journal of biological chemistry. 2001;276(30):27799-805.

9. Nilsson M, Frykberg L, Flock JI, Pei L, Lindberg M, Guss B. A fibrinogen-binding protein of Staphylococcus epidermidis. Infect Immun. 1998;66(6):2666-73.

10. Bowden MG, Heuck AP, Ponnuraj K, Kolosova E, Choe D, Gurusiddappa S, et al. Evidence for the "dock, lock, and latch" ligand binding mechanism of the staphylococcal microbial surface component recognizing adhesive matrix molecules (MSCRAMM) SdrG. The Journal of biological chemistry. 2008;283(1):638-47.

11. Bowden MG, Chen W, Singvall J, Xu Y, Peacock SJ, Valtulina V, et al. Identification and preliminary characterization of cell-wall-anchored proteins of Staphylococcus epidermidis. Microbiology (Reading, England). 2005;151(Pt 5):1453-64.

12. Otto M. Staphylococcus epidermidis--the 'accidental' pathogen. Nature reviews Microbiology. 2009;7(8):555-67.

13. Wolfmeier H, Pletzer D, Mansour SC, Hancock REW. New Perspectives in Biofilm Eradication. ACS Infect Dis. 2018;4(2):93-106.

14. Gahlot R, Nigam C, Kumar V, Yadav G, Anupurba S. Catheter-related bloodstream infections. Int J Crit Illn Inj Sci. 2014;4(2):162-7.

15. Rogers KL, Fey PD, Rupp ME. Coagulase-Negative Staphylococcal Infections. Infectious Disease Clinics of North America. 2009;23(1):73-98.

16. Ziegler MJ, Pellegrini DC, Safdar N. Attributable mortality of central line associated bloodstream infection: systematic review and meta-analysis. Infection. 2014.

17. Stevens V, Geiger K, Concannon C, Nelson RE, Brown J, Dumyati G. Inpatient costs, mortality and 30-day re-admission in patients with central-line-associated bloodstream infections. Clin Microbiol Infect. 2014;20(5):O318-24.

18. Ma TM, VanEpps JS, Solomon MJ. Structure, Mechanics, and Instability of Fibrin Clot Infected with Staphylococcus epidermidis. Biophys J. 2017;113(9):2100-9.

19. Piechocka IK, Bacabac RG, Potters M, Mackintosh FC, Koenderink GH. Structural hierarchy governs fibrin gel mechanics. Biophys J. 2010;98(10):2281-9.

20. Collet JP, Soria J, Mirshahi M, Hirsch M, Dagonnet FB, Caen J, et al. Dusart syndrome: a new concept of the relationship between fibrin clot architecture and fibrin clot degradability: hypofibrinolysis related to an abnormal clot structure. Blood. 1993;82(8):2462-9.

21. Collet JP, Park D, Lesty C, Soria J, Soria C, Montalescot G, et al. Influence of fibrin network conformation and fibrin fiber diameter on fibrinolysis speed: dynamic and structural approaches by confocal microscopy. Arterioscler Thromb Vasc Biol. 2000;20(5):1354-61.

Chapter 4: Role of Polysaccharide Intercellular Adhesin in Staphylococcus Interaction with Fibrin Network[3]

4.1 Abstract

The co-existence of staphylococcal biofilms and host protein clots appears on most, if not all, indwelling medical devices, contributing to 50-70% of nosocomial infection – the fifth leading cause of death in the US. *IcaB,* a cell surface-attached protein, has a key role in staphylococcal biofilm formation and immune evasion by deacetylating and introducing positive charge to polysaccharide intercellular adhesin (PIA) molecules; these charges facilitate adhesion of bacterial cells within a biofilm cluster. However, the role of *IcaB* in staphylococcal biofilm formation in the presence of host fibrin network remains unclear. Here we study the role of *icaB* on an *in vitro* model of biofilm-infected fibrin network. Specifically, using an *icaB* deletion, we evaluated the effects of PIA deacetylation on staphylococcal interaction with a fibrin network and the resulting structural and mechanical changes to the network. We find that the $\Delta icaB$ mutant degrades fibrin networks faster than the wild-type, both structurally and mechanically. Indeed, the $\Delta icaB$ produce more *sspA*, a protease that putatively degrades fibrin. We further demonstrate that the $\Delta icaB$ cells, which are more mobile and diffusive than the wild type cells, co-localize with the fibrin fibers. This co-localization is correlated with fibrin network degradation. These results suggest a pivotal role for *icaB* in modulating staphylococcal bacterial-

[3] The work of Chapter 4 is in preparation of publication as "Role of Polysaccharide Intercellular Adhesin in Staphylococcal Interaction with Fibrin Network" by **Tianhui Ma**, J. Scott VanEpps, and Michael Solomon

fibrin interactions and resulting fibrin mechanical structure. This dynamic could be relevant to a potential molecular mechanism for infection-induced thromboembolism.

4.2 Introduction

Polysaccharide intercellular adhesin (PIA), first discovered by Mack, D. et.al., is a homopolymer of β-1,6-linked N-acetylglucosamine (GlcNAc) residues[1]. It dominates the extracellular polymeric substance (EPS) microstructure of *Staphylococcus epidermidis*[2],the leading cause of device-related infections[3]. The production of PIA is encoded by the *ica* gene locus, which consists of the *icaA*, *icaB*, *icaC*, and *icaD* genes, first discovered by Heilmann et al. in *S. epidermidis* [4] but is also present in *Staphylococcus aureus*[5]. IcaA and IcaD form a GlcNA-transferase located in the cellular membrane[6] and produce a chain from activated GlcNAc monomers[7]. IcaC elongates the chain to longer polymers and might be involved in the export of PIA[6]. IcaB, located on the cell surface, deacetylates the GlcNAc moieties and thus, introduces positive charges on the PIA polymer chain[8]. This deacetylation step is essential for the surface localization of PIA and its intercellular adhesion function. The absence of IcaB impairs the key bacterial virulence factor – biofilm formation – and their resistance to immune systems[8, 9].

On implanted medical devices, bacteria often appear simultaneously with fibrin [10 11 12] – the main structural component of blood clots[13, 14]. The co-existence of bacteria and fibrin has been explained with their bidirectional relationship: bacteria activate inflammation and host clots promote bacterial adhesion[10]. Although the deacetylation of PIA by IcaB has been shown to be key to biofilm formation in the absence of host fibrin, it is unclear how it mediates bacterial behavior in the presence of fibrin network. IcaB directly controls whether PIA persists on bacterial cell walls and thereby influences cell surface properties; these surface properties in turn play an important role in cell-fibrin interaction. These interactions may vary the microenvironment of the bacterial cells, which may indirectly influence the expression of other genes as a response to the environmental change[15] and further influence bacterial interaction with

fibrin. For example, *S.epidermidis* has a gene – *sspA* – that produces glutamyl endopeptidase and serine protease that putatively degrades fibrin[16 9], which may have a significant effect on fibrin integrity.

Fibrin network integrity, defined by its structure and mechanical properties, predict the probability of embolism[17 18 19]. Clinically, device-related infection has been correlated with thromboembolism[20 21 22]. Our previous work suggests that a fibrin network infected with bacteria is more prone to rupture than a sterile fibrin network[17]. Investigation into how *icaB* influences the integrity of a bacteria-infected fibrin network could contribute to molecular understanding of the relationship between bacterial infection and thromboembolism.

Here we compare an *icaB* deletion mutation of *S.epidermidis* with the wild type (WT) and a complement strain with a plasmid containing the *icaB* gene to study the role of *icaB* in the bacteria-fibrin interaction and the resulting changes to the integrity of a fibrin network. We show that the $\Delta icaB$ degrades the fibrin network faster than the WT. The fibrin degradation is likely mediated by increased expression of *sspA*. We further find that the $\Delta icaB$ co-localizes with fibrin fibers while the WT remains in cell clusters independent of the fibrin fibers. This localization may further facilitate fibrin proteolysis.

4.3 Materials and Methods

4.3.1 Bacterial strains

The clinical isolate *S.epidermidis* 1457 and its Δ$icaB$, together with a complement strain with a plasmid containing the *icaB* gene under a xylose promoter— Δ$icaB$ + pTX$icaB$, were obtained from Dr. Michael Otto [8]. Briefly, the Δ$icaB$ strain is an isogenic $icaB$ deletion (see ref [8]for details). To generate plasmid pTX$icaB$, the *icaB* gene was amplified using mutagenizing primers and cloned into plasmid pTX15 [8 23], which was transformed into the Δ$icaB$ yielding Δ$icaB$ + pTX$icaB$ [8].

4.3.2 Bacterial culture conditions and fibrin network formation

Citrate-free thrombin from human plasma (605206-100U) and plasminogen-depleted fibrinogen (Fg) from human plasma (341578-500MG) were purchased from EMD Millipore (Billerica, MA).

For culturing *S. epidermidis* 1457 and the Δ$icaB$, a colony from trypic soy agar is inoculated and cultured in trypic soy broth with 1 wt.% glucose (TSB_G). For Δ$icaB$ + pTX$icaB$, $10ug/ml$ tetracycline (with Hydrochloride, Millipore Sigma) was added to both the agar and broth and the 1 wt.% glucose was replaced with 1 wt.% xylose (Sigma-Aldrich) (TSB_X). After the bacterial culture reached exponential growth phase, an INCYTO C-Chip Disposable Hemocytometer (Thermo Fisher Scientific) is used to determine the cell concentration. A target number of cells are diluted in a 0.5mg/ml Fg solution of 200µl to achieve 200 $cells/\mu l$. With this cell concentration, a blood clot (or, thrombus) with a size of 0.1 mm^3 would have around 20 cells/clot,

which could be considered as an initial stage of an infected clot. Fg solutions were made by diluting the stock solution with TSB_G for *S. epidermidis* 1457 and the Δ*icaB*, and TSBx with tetracycline for Δ*icaB* + pTX*icaB*. TSB_G was used for constitution of Fg solutions for sterile fibrin networks. Then the samples were transferred to a Nunc Lab-Tek II chambered cover glass dish (Thermo Fisher Scientific) kept at 37℃. Fibrin network was initiated by adding thrombin (0.5 U/mL as final concentration) to the Fg solution at 37℃. After 15 minutes, 200µl TSB_G or TSBx was added on top of the fibrin network. The chambered cover glass was sealed with Breathe-Easy® sealing membrane (Sigma-Aldrich) to prevent desiccation. The samples were held in a 37℃ incubator for the targeted amount of time before analysis, as described below. For conditions in which bacteria grew in medium without fibrin, 400µl medium was used instead. For Δ*icaB* + pTX*icaB* growing both with and without fibrin, 10ug/ml tetracycline and 1% xylose was added to the medium again after 9-10 hours after the start of the culture to maintain *icaB* expression.

4.3.3 Structure visualization and particle tracking

Fibrin microstructure, fibrin elasticity, and bacterial cell mobility were evaluated using confocal laser scanning microscopy (CLSM), multiple particle tracking, and microrheology as previously described by Ma et.al. [17]. Briefly, a Nikon A1Rsi CLSM with a 100×, 1.45 NA, oil immersion objective (Nikon, Melville, NY) was used. Image volumes for microstructure visualization and analysis were obtained by axially scanning from the coverslip to 20 μm above the coverslip in increments of 1 μm. The image size was 127.45 × 127.45 μm^2 at 512 × 512-pixel resolution. For multiple-particle tracking, 2D time series of 500 images with size 42.48 × 42.48 μm^2 (512 × 512 pixels) were collected at 30 frames per second at a distance of 10 ± 5 µm above coverslip. Both

image volumes and time series were captured randomly over the specimen dish. Image volumes at five different regions in each sample were taken for structure visualization; time series at five different regions in each sample were taken for fibrin mechanics. Image projections and renderings of the 3D volumes were made with the software ImageJ (http://rsbweb.nih.gov/ij/).

Fibrin was visualized using AlexaFluor 546 (558/573 nm) conjugated human Fg (Thermo Fisher Scientific), which was mixed with unlabeled fibrinogen in a molar ratio of 1:4 [17]. Bacterial cells were stained for 30 min with 20 μM SYTO 40 (420/441) (Thermo Fisher Scientific) and PIA was stained with 10 µg/mL Wheat Germ Agglutinin, Alexa Fluor™ 488 Conjugate (Thermo Fisher Scientific). Sulfate modified Microspheres, diameter 1.0 μm, with yellow-green fluorescent FluoSpheres (505/515), 2% solids (Thermo Fisher Scientific) were used for particle tracking microrheology. Bovine serum albumin (BSA; Sigma-Aldrich, St. Louis, MO) was adsorbed to the microsphere surface to control the interaction between probes and Fg [17 24]. BSA was dissolved in filtered deionizing water. The probes (0.1% solids as the final concentration) were incubated with 0.02 wt % BSA solutions on a roller at room temperature overnight. Probes were washed with deionizing water and resuspended into Fg or bacterial/Fg solution before clotting with 0.04% solids.

4.3.4 Structure quantification

The degree of bacteria-fibrin co-localization was calculated from binary images as described in [17]. We define bacteria and fibrin as being co-localized when their fluorescence emission overlaps in the same pixel. Briefly, bacteria-fibrin overlap pixels are the intersection of the on-pixels in the bacteria and fiber channels, with on-pixels define through a threshold operation. The overlap

percentage of every image with respect to fibrin and bacteria was computed by dividing the overlap area by the fibrin area and bacteria area, respectively. Image analysis was performed in MATLAB R2014b (The MathWorks, Natick, MA).

In the fibrin structure images, fibrin appears to be either branched patterns or patchy patterns. We introduce patch percentage to represent the area fraction of the patchy pattern relative to all fibrin patterns, including branched and patchy ones, in a certain image. Patch percentages were calculated from binary images and the analysis was performed in Python 3.6.4. We first divided all of the identified fibrin pixels into contiguous objects by means of cluster analysis. The minimal rectangle that encompasses all pixels in a connected object was drawn and the area fraction of the fibrin pixel inside this rectangular box was calculated. For example, an area fraction that equals 0.36 means that 36% of the box are fibrin pixels with the rest of the pixels being voids. A continuous object that is patchy pattern would have a high area fraction whereas an object of a branched pattern would have a low area fraction. Thus, we use the area fraction to identify whether a fibrin pattern is patchy or branched. As shown in Figure 4-1, an area fraction equals 0.36 was chosen to define patches versus branches: if the density is below 0.36, then we define the object as a branch, otherwise, the object is defined as a patchy pattern. Figure 4-1 shows that a non-degraded fibrin image calculated this way has a patch percentage of 16% and a fully degraded fibrin image example has a patch percentage of 93%. The patch percentage of every image is then calculated by separating fibrin patterns into patches and branches. Using this method, we quantified the structural characteristic of a fibrin image.

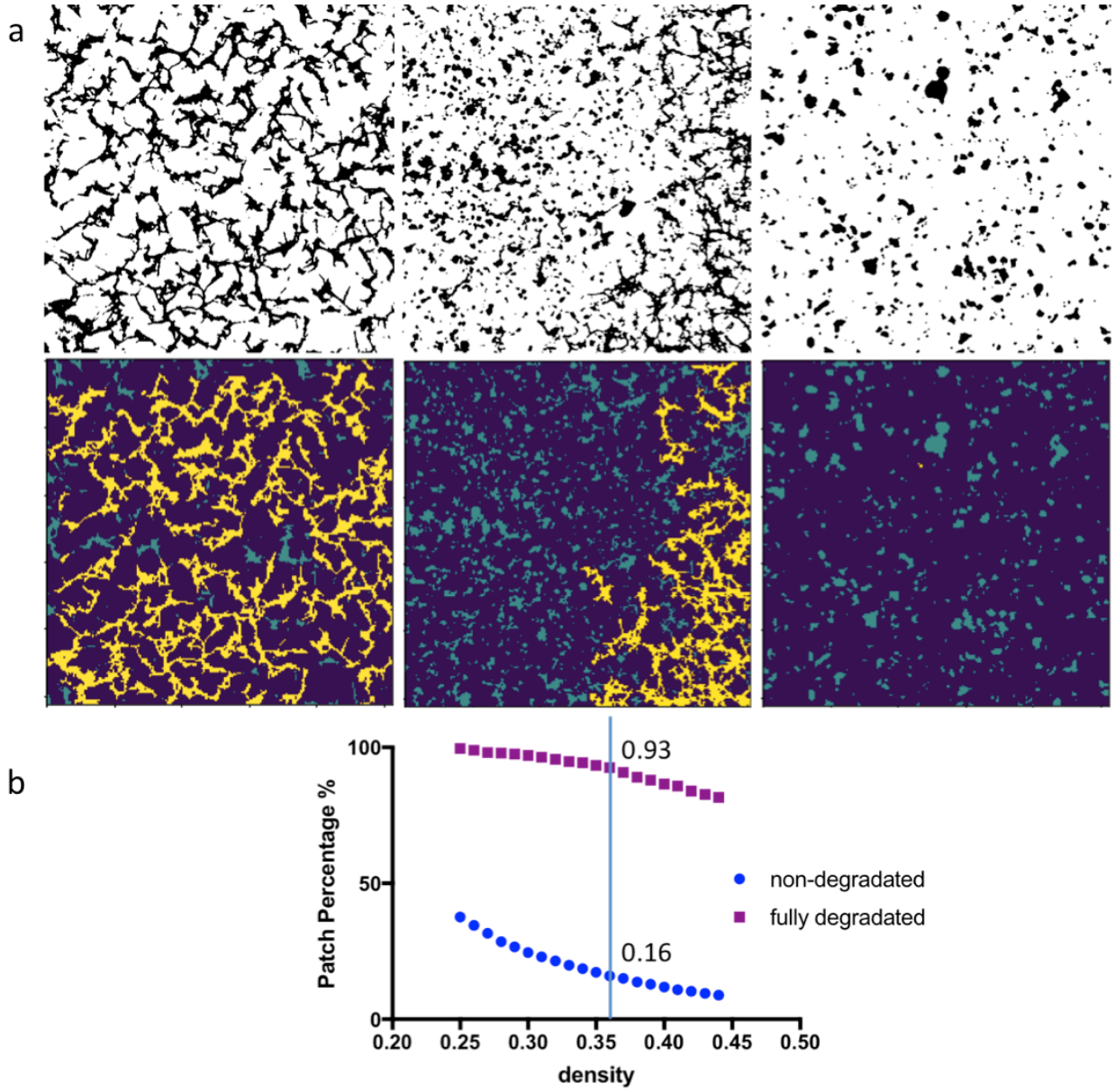

Figure 4-1 Image Analysis of patch versus branch of a fibrin network

(a) Top row: binary images of a non-degraded fibrin (left), a partially degraded fibrin (middle) and a fully degraded fibrin (right). Bottom row: analyzed images of the corresponding binary images with yellow indicating branches and blue indicating patches. (b) The result of fibrin patch percentage varying with the chosen density value of fiber pixels inside a rectangular box drawn around the furthest fibrin pixels in a connected object (c.f. Methods). It shows that the results are relatively insensitive to the chosen density. With a chosen density value of 0.36, a non-degraded fibrin has a patch percentage of 16% and fully degraded fibrin has a patch percentage of 93%.

4.3.5 Microrheology

The theory and method for using particle tracking microrheology for probing fibrin mechanics was described in [17], as adapted from the theory and methods that are well-developed for polymers[25, 26]. Briefly, we quantify the mean square displacement (MSD) ($\Delta x^2(t)$) —the average squared distance a probe travels in a given lag time – of probes dispersed in the fibrin matrix from time series of 2D images. MSDs were computed from probes' centroids as identified by TrackPy 3.0 (http://soft-matter.github.io/trackpy/stable/).

4.3.6 Cell mobility

Cell mobility in cultures without fibrin was characterized to study the ability of a bacterial cell to undergo displacement by means of Brownian motion. Bacteria were cultured without fibrin for the measurements cell mobility due to the limitations of experimental methods. Nevertheless, they are intrinsic cell properties that would influence the bacterial behaviors at the presence of fibrin. A bacterial cell's mobility is constrained by other bacterial cells, which influences whether it has the potential to wander around and find fibrin fibers. It is therefore studied in cell cultures without fibrin. It cannot be characterized inside fibrin because once a mobile cell is trapped by fibrin, it becomes stagnant[10]. Bacterial cells were tracked and analyzed by TrackPy 3.0 and the mobility reported as a diffusivity. Time-series at three different regions were taken within each sample for the cell mobility studies.

4.3.7 Zeta potential measurement

Just like cell mobility measurement, bacteria were cultured without fibrin for the measurements of zeta potential due to the limitations of experimental methods. The measurement of zeta

potential is not feasible with the original setup with bacteria growing in fibrin. Thus, stationary phase bacteria were used to resemble the biofilm phenotype[10]. Bacterial strains were cultured in 1-2ml medium (TSB_G for *S.epidermidis* 1457 and its $\Delta icaB$ and TSBx with $10\mu g/ml$ tetracycline for $\Delta icaB$ + pTX*icaB*) to the stationary phase with the optical density at 600nm (OD_{600}) = 1.45 ± 0.1. Stationary phase was used here to resemble the biofilm phenotype in the rest of the study. Cells were diluted to c.a. $10^6 cells/ml$ for zeta potential measurements made using a Zetasizer Nano ZSP (Malvern Panalytical).

4.3.8 RNA extraction and RT-PCR

After 19 ± 1 hours' incubation at 37℃ in cover glass dishes as described above, samples were completely scraped from the wells and centrifuged at 8000 rpm for one minute to pellet the cells. After washing with Milli-Q water, cells were resuspended in an NAES buffer (50mM sodium acetate buffer, 10mM EDTA and 1% SDS at pH = 5) and vortexed for one minute. Acid-washed glass beads (212-300µm, Sigma-Aldrich) of 0.5 grams were used for homogenizing each sample in a Bullet Blender Storm 24 (Next Advance) for 30 minutes. Cell lysis was achieved with 500 µl TRIzol (Sigma-Aldrich) and 100 µl chloroform (Sigma-Aldrich), followed by a three-minute vortex. Following this, samples were centrifuged at 12000 rpm for 15 minutes at 4°C. Then the samples were resuspended in 600 µl 70% ethanol (Sigma-Aldrich) and vortexed for one minute. Samples were then transferred to spin columns from an RNase free Mini Kit (Qiagen) and processed per manufacturer's instructions. RNA quality and integrity were confirmed using UV spectrophotometry and Bioanalzer Purified RNA samples were stored at -80°C.

For reverse transcription polymerase chain reaction (RT-PCR), QuantiTect sybr green RT-PCR (Qiagen) was performed in 25 µl reactions. The reaction mixture contained 12.5 µl RT-PCR Master Mix, 0.25 µl RT Mix, 2 µl of RNA sample (30 ng), and 2 µl of each gene forward/reverse-primer (F/R-primer, 12.5 µM) and 6.5 µl of RNase-free water. Thermal cycling protocol began with 10 minutes reverse transcription at 50°C, followed by an initial activation step of 5 minutes at 95°C, denaturation of 10 seconds at 95°C, and combined annealing/extension step at 60°C for 30 seconds for a total of 40 cycles. Sequences for forward and reverse primers are CCAATATAGACAACTTTACC and GCAACTATAAGTAGCAATAC, respectively. Both of them have an amplicon length of 119 and GC% of 35%. The Primer Melting Temperature (Tm) for the forward *sspA* was 55 and that of the reverse *sspA* was 56.

4.3.9 Time points and experimental conditions

Measurements were conducted at initial, mid-point, and end-point times: the initial time point is recorded within one hour after fibrin network initiation; the mid-point time is 19 ± 1 hours after fibrin network initiation; the end point time is 30 ± 1 hours after fibrin network initiation, which allows the bacteria to generate a significant effect on the fibrin under the experimental conditions. The mid-point time is used in some cases to characterize physical and genetic conditions that may be causative of end-point time observations.

in Figure 4-5(a,b) for bacterial locations inside a fibrin network and Figure 4-6 for *sspA* expression. In this study, we hypothesize that Figure 4-5 and 4-6 could be the causes for Figure 4-2 and 4-5 – the results. A mid time point is therefore used because we want to observe the

causes before the results. Specifically, for example, the co-localization of Δ$icaB$ and fibrin fibers cannot be observed any more at the endpoint time when almost all of the fibrin fibers become patches.

4.3.10 Statistics

Statistics were performed using GraphPad Prism (GradphPad Software, Inc., San Diego, CA). One-way ANOVA was used for Figure 4-2, 4-4 and 4-6. Student's t-test was used for Figure 4-7.

4.4 Results:

4.4.1 *S. epidermidis* Δ$icaB$ alters fibrin network morphology to a higher degree than WT

Figure 4-2 reports the microstructure of fibrin networks infected with *S. epidermidis* 1457 (WT), Δ$icaB$ and Δ$icaB$ + pTX$icaB$. The initial fibrin network, inoculated with bacteria at 200cells/μl (c.f. Methods), has a porous structure. Thirty hours later the bacteria have grown within the fibrin, leading to some loss of the branched pattern, and giving rise to patchy distribution of fibrin. In those samples inoculated with WT and the Δ$icaB$ + pTX$icaB$, branches remain between the patchy regions, whereas in the fibrin networks infected with Δ$icaB$, the branched network pattern is almost completely lost, leaving just dense patches.

To better quantify this observation, we used image analysis to characterize the percentage of patchy morphology versus branched morphology (c.f. Methods & Figure 4-1). As shown in Figure 4-2b, a fibrin network without bacteria at one hour analyzed in this way has an average

patchy pattern percentage of $(16 \pm 5)\%$. No difference in fibrin network morphology is noticed at one hour: the patch percentage of a sterile fibrin network, a fibrin network infected with the wild type, $\Delta icaB$ and $\Delta icaB$ + pTX*icaB* is measured to be $(16 \pm 7)\%$, $(16 \pm 1)\%$, $(17 \pm 6)\%$, $(17 \pm 2)\%$, respectively. At the endpoint time, a sterile fibrin network has a patch percentage of $(15 \pm 5)\%$, whereas that of a fibrin network infected with the wild type, $\Delta icaB$ and $\Delta icaB$ + pTX*icaB* is measured to be $(36 \pm 10)\%$, $(93 \pm 5)\%$ and $(46 \pm 14)\%$, respectively.

Hypothesis testing with ANOVA indicates that the patch percentage of a fibrin infected with the $\Delta icaB$ at the endpoint time are significantly different than the other conditions ($P<0.0001$). Both the wild type and the $\Delta icaB$-complement strain ($\Delta icaB$ + pTX*icaB*) have a significant increase in patch percentage as compared to their beginning stages ($P<0.005$) (c.f. Methods). Thus, judging from the patch percentage in the fibrin structures, we conclude that the clinical strain *S.epidermidis* 1457 can change the morphology of fibrin networks over time and the change is enhanced when infected by $\Delta icaB$. This change of fibrin morphology from branchy patterns to patchy patterns resembles the degradation of fibrin by plasmin (Figure 4-3). The result therefore indicates the degradation of fibrin by the bacteria.

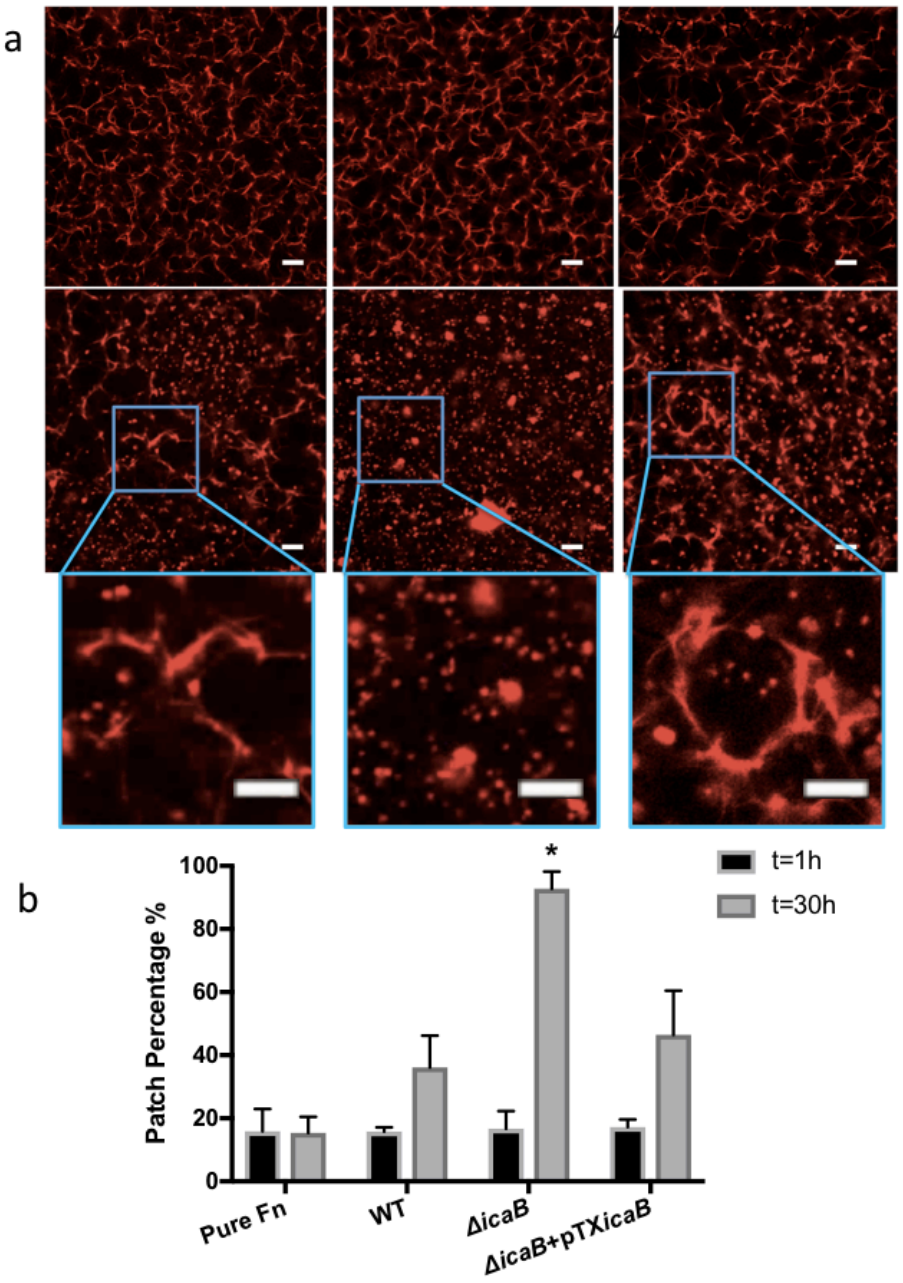

Figure 4-2 Structural characterization of fibrin degradation

(a) Images of confocal microscopy of wild-type (WT), Δ$icaB$ and Δ$icaB$ + pTX$icaB$ (from left to right). Red indicate fibrin, blue indicates bacteria. Top row: within one hour after fibrin network initiation; Second row: 30 hours after fibrin network initiation; Third row: Zoomed-in images from regions in the second row. (b) Patch percentage of sterile fibrin, wild-type (WT), Δ$icaB$ and Δ$icaB$ + pTX$icaB$ at time zero and 30h. Error bars indicate standard deviation of five replicates. An asterix indicates statistical significance.

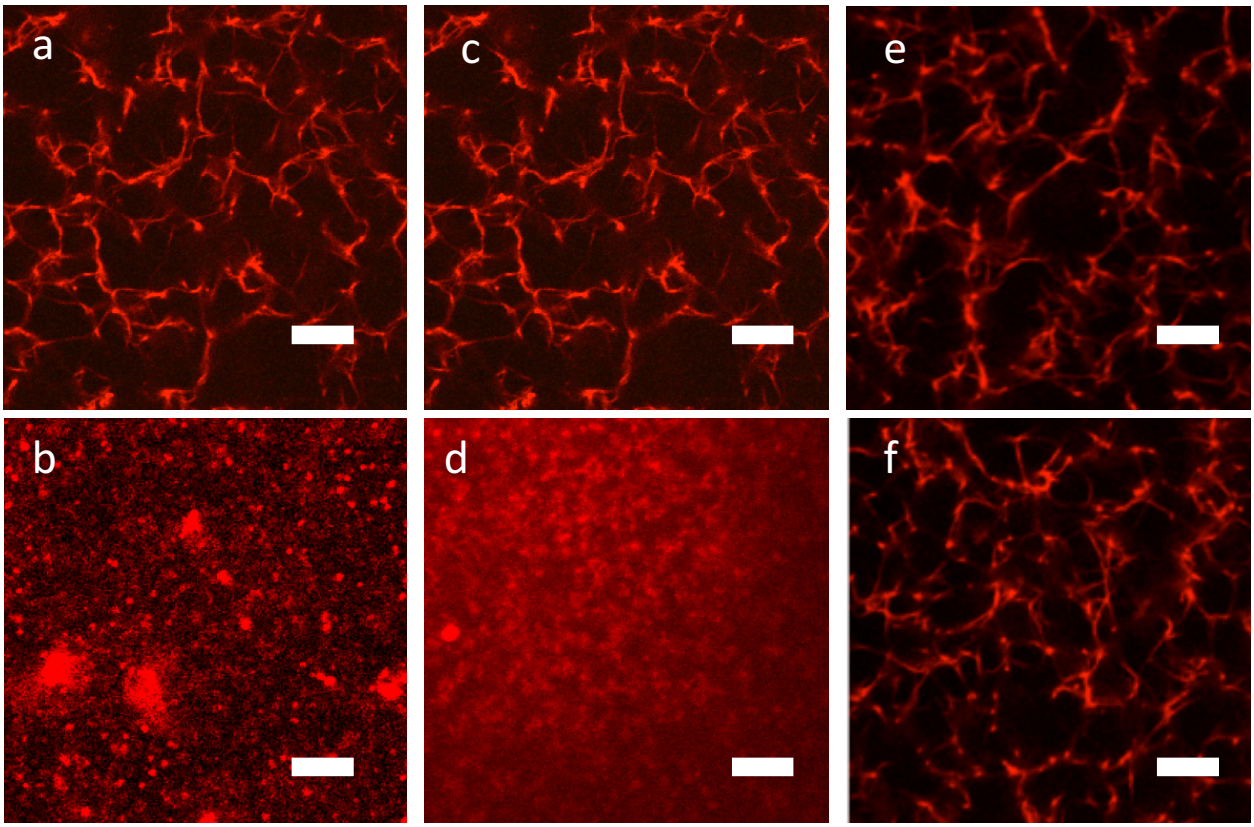

Figure 4-3 Compare fibrin infected with the mutant and fibrin degraded by plasmin.

Fibrin infected with 100cells/ml at (a) time 0 and (b) 50 hours later when cells grow into biofilms; Fibrin with 3.3×10^{-2}U/ml plasmin solution loaded on top at (c) time 0 and (d) 9 hours later; pure fibrin at (e) time 0 and (f) time 50h. Scale bar = 10 μm.

4.4.2 Fibrin networks infected with the Δ*icaB* becomes a mechanically weaker network

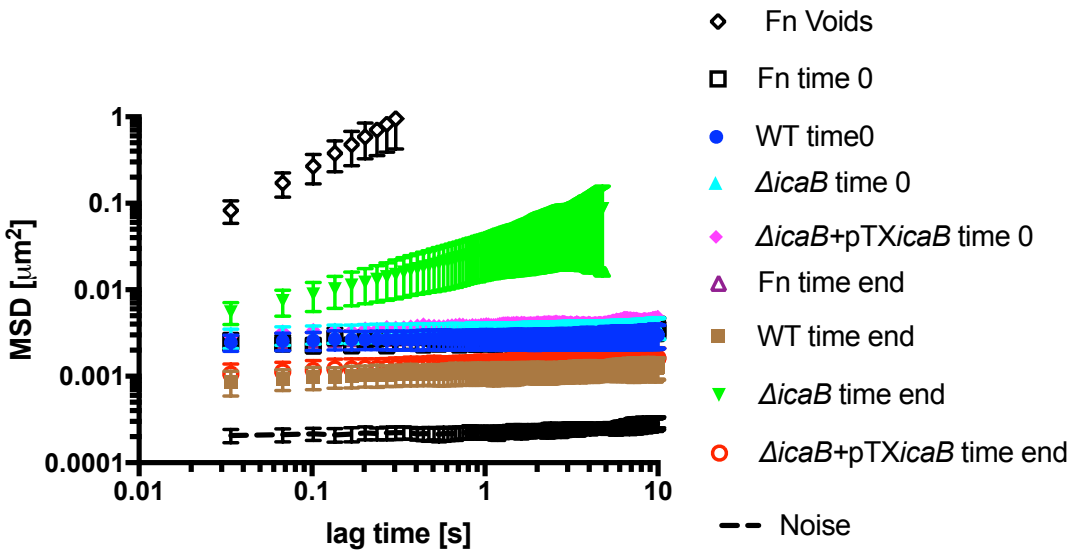

Figure 4-4 | Mean square displacements of probes trapped on fibrin fibers of pure fibrin and fibrin infected with the wild-type (WT) *S.epidermidis* 1457, its Δ*icaB* and the complement strain Δ*icaB* + pTX*icaB* at the starting and ending time point after clot initiation, respectively, together with free loating probes in fibrin (Fn) voids and noise floor

(Fn time 0, WT time 0, Δ*icaB* time 0, Δ*icaB* + pTX*icaB* time 0 and Fn time end overlap; WT time end and Δ*icaB* + pTX*icaB* time end overlap). Error bars indicate standard deviation of five replicates. The probes (0.1% solids as the final concentration) were incubated with 0.02 wt % (for probes trapped on fibrin fibers) and 10 wt.% (for probes freely floating in fibrin voids) BSA solutions on a roller at room temperature overnight (c.f. Methods).

We hypothesize that the change from branched to patch structure of a fibrin network is a consequence of fibrin degradation. Am implication of such a hypothesis is that the fibrin network would be less elastic and more viscous. To test this hypothesis, we applied microrheology (c.f. Methods). In Figure 4-4, the mean square displacement (MSD) of submicron particle probes trapped onto fibrin fibers reveals the mechanical properties of the fibers. Thus, an ensemble average of the MSDs of probes over an entire fibrin clot reveals the mechanical properties of the fibrin clot [1]. A complete fibrin clot at the experimental concentration is pure elastic, or solid-like

[1]. For a pure elastic solid, the MSD remains fixed over the lag time, i.e. probes tend to fluctuate around the same position. When in a purely viscous liquid, the MSD increases linearly with the lag time, i.e. probes in a pure liquid undergo Brownian motion over time. Therefore, the log slope of the measured MSD, α, characterizes the viscoelasticity of the material (c.f. Methods). For a pure elastic solid $\alpha = 0$ whereas for a pure viscous liquid $\alpha = 1$; for viscoelastic materials $0 < \alpha < 1$, which increasing α indicating more viscous and less elastic character. In Figure 4-4, fibrin and infected fibrin at t=1h behave like a pure elastic solid; at the ending time point, fibrin infected with the wild type and $\Delta icaB$ + pTX$icaB$ still behaves like a solid whereas fibrin infected with the $\Delta icaB$ behaves like a viscoelastic material. Fibrin void behaves like a pure liquid.

In Figure 4-5a, we show that at the initial stage, sterile fibrin control and fibrin networks infected with $200 cells/\mu l$ bacteria all behave like an elastic solid with an average α value of 0.04 ± 0.02. At the endpoint time, the sterile fibrin control, fibrin networks infected with the wild type and $\Delta icaB$ + pTX$icaB$ remain solid-like with an α value of 0.04 ± 0.01, 0.05 ± 0.01 and 0.06 ± 0.01, respectively. However, the fibrin network infected with the $\Delta icaB$ shows $\alpha = 0.5 \pm 0.2$, indicating that this material has an even balance of elastic and viscous properties. Statistics indicate that $\Delta icaB$ at the endpoint time is significantly different than the rest of the conditions ($P<0.0001$). Thus, a fibrin network infected with the $\Delta icaB$ changes from an elastic solid to a viscoelastic material over time during the replication of the bacterial cells, whereas a fibrin network infected with the wild type and the $\Delta icaB$ + pTX$icaB$ stays elastic till the endpoint time.

From the MSDs, we characterized the creep compliance, $J(t)$, of the fibrin networks. The creep compliance J(t) is related to the MSD as the following [2]:

$$\mathrm{J(t)} = \frac{\pi a \langle \Delta x^2(t) \rangle}{k_B T}$$

The creep compliance is the amount of strain a material experiences when a unit stress is applied to it. Generally, the greater the value of J(t), the less rigid the material. Figure 4-5b shows the creep compliance, $J(t)\ at\ t = 1s$, of fibrin networks at different conditions. We show that at the initial stage, sterile fibrin and infected fibrin have an average $J(t = 1s)$ value of $1.2 \pm 0.25\ Pa^{-1}$. At the endpoint time, the sterile fibrin control, fibrin networks infected with the wild type and $\Delta icaB$ + pTX*icaB* marinating comparable rigidity with $J(t = 1s)$ values of $1.10 \pm 0.26\ Pa^{-1}$, $0.42 \pm 0.12\ Pa^{-1}$ and $0.52 \pm 0.15\ Pa^{-1}$, respectively. However, the fibrin network infected with the $\Delta icaB$ has $J(t = 1s) = 10.5 \pm 5.7\ Pa^{-1}$. This order of magnitude increase in compliance indicates that the material is significantly less rigid at the endpoint time relative to the initial time ($p<0.0005$). Fibrin infected with the wild type at the starting and the endpoint time do not differ significantly from each other; neither does fibrin infected with $\Delta icaB$ + pTX*icaB differ from X* ($P>0.99$) (c.f. Methods). Judging from Figure 4-5(a) and 4-5a(b), a fibrin network infected with $\Delta icaB$ becomes mechanically weaker over time, whereas a fibrin network infected with the wild type and the $\Delta icaB$ + pTX*icaB* strain does not display a significant mechanical change. Thus, fibrin network morphologic changes caused by presence of wild type and $\Delta icaB$ + pTX*icaB* do not lead to significant change in mechanical properties, whereas $\Delta icaB$ does. Potential explanations are provided in the discussion section.

Thus, the significant morphologic changes of fibrin – from branches to patches – caused by $\Delta icaB$ is associated with significant change in fibrin mechanics, as the fibrin becomes more liquid-like and less rigid.

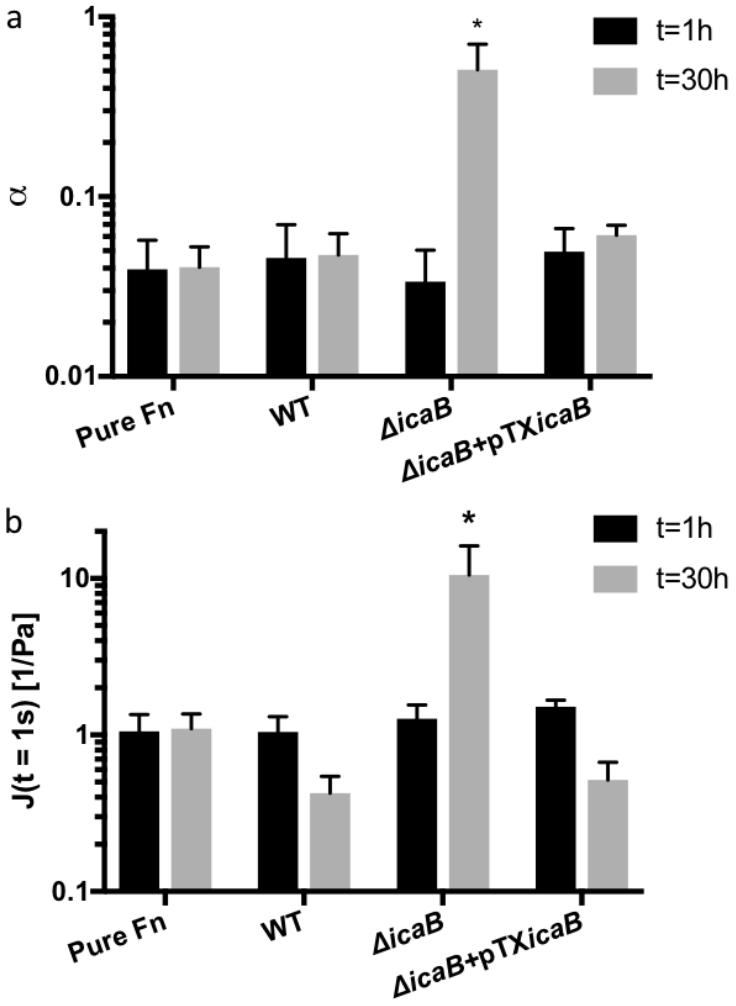

Figure 4-5 | Mechanical characterization of infected fibrin networks by microrheology

(a) The log slope of the MSD curves, α, of probes trapped on fibrin networks at t =1h and t = 30h (b) Creep compliance J(t) at t=1s of sterile fibrin, wild-type (WT), $\Delta icaB$ and $\Delta icaB +$ pTX$icaB$ at one hour and 30 hours after fibrin network initiation. Error bars indicate standard deviation of five replicates in both (a) and (b). Asterix indicates statistical significance.

4.4.3 Δ*icaB* co-localizes with fibrin network

Figure 4-5 reports the degree of co-localization of bacterial cells and fibrin. As shown in Figure 4-5a, the bacterial cells of the wild type and the Δ*icaB*-complement strain (Δ*icaB* + pTX*icaB*) persist as clusters; in these materials, the fibrin fibers are exposed, whereas the cells of the Δ*icaB* co-localize with the fibrin. The zoomed-in images show the location of PIA relative to bacterial cells. PIA appears to be concentrated inside the cell clusters of the wild type and Δ*icaB* + pTX*icaB*. *On the other hand,* PIA is around every Δ*icaB* cell.

Figure 4-5b quantifies the degree of bacteria-fibrin co-localization. At mid time point, $(7.7 \pm 5.8)\%, (63 \pm 13)\%$ and $(19 \pm 5.9)\%$ of the fibrin area is co-localized with the wild type, the Δ*icaB* and the Δ*icaB* + pTX*icaB* strains, respectively; and the bacteria-fibrin co-localization is $(7.6 \pm 3.8)\%, (37 \pm 6.0)\%$ and $(15 \pm 4.1)\%$ of the bacteria area of wild type, the Δ*icaB* and the Δ*icaB* + pTX*icaB* strain, respectively. In both cases, the Δ*icaB*-fibrin overlap ratio at the mid time point is significantly different than the rest of the conditions ($P<0.0001$) (c.f. Methods). Thus, when growing in fibrin, the Δ*icaB* tends to cluster on the fibrin network whereas the wild type and Δ*icaB* + pTX*icaB* tend to cluster independently of the fibrin network.

We hypothesized that the difference in the cell location relative to the fibrin network could result from differences in cell surface charge and cell mobility of the wild type and the Δ*icaB*. In Figure 4-5c, we show that the zeta potential of the stationary-phase wild type, Δ*icaB* and Δ*icaB* + pTX*icaB* (c.f. Methods) are $(-6.8 \pm 1.6)mV$, $(-22.4 \pm 2.2)mV$ and $(-13.5 \pm 4.7)mV$, respectively, with Δ*icaB* being significantly different than the wild type ($P<0.0001$) and the Δ*icaB* + pTX*icaB* strain ($P<0.05$). Thus, the Δ*icaB* is more negatively charged.

Cell mobility was meausred to characterize the ability of a bacterial cell to explore its local environment through diffusion (c.f. Methods). A free-floating (planktonic cell) will have a higher mobility than a cell trapped in an aggregate or biofilm. The dynamics of the former will be diffusive, whereas the dynamics of the latter will be localized. In Figure 4-5d, we report the mean squared displacement (MSD) of cells in media at t=1s, as measured by particle tracking microscopy (c.f. Methods). The values of MSD at t=1s of the wild type, Δ$icaB$ and Δ$icaB$ + pTX$icaB$ are $(0.005 \pm 0.0008)\mu m^2$, $(0.06 \pm 0.02)\mu m^2$ and $(0.008 \pm 0.0009)\mu m^2$, respectively. Statistics indicates that the MSD at 1s of Δ$icaB$ is significantly different than the wild type and Δ$icaB$ + pTX$icaB$ (P<0.01). In Figure 4-6, we furthermore show that the slope of the Δ$icaB$ MSD curve is positive while that of the wild type and Δ$icaB$ + pTX$icaB$ are nearly zero. It shows Δ$icaB$ cells are free and diffusive whereas the wild type and Δ$icaB$ + pTX$icaB$ are trapped and immobile.

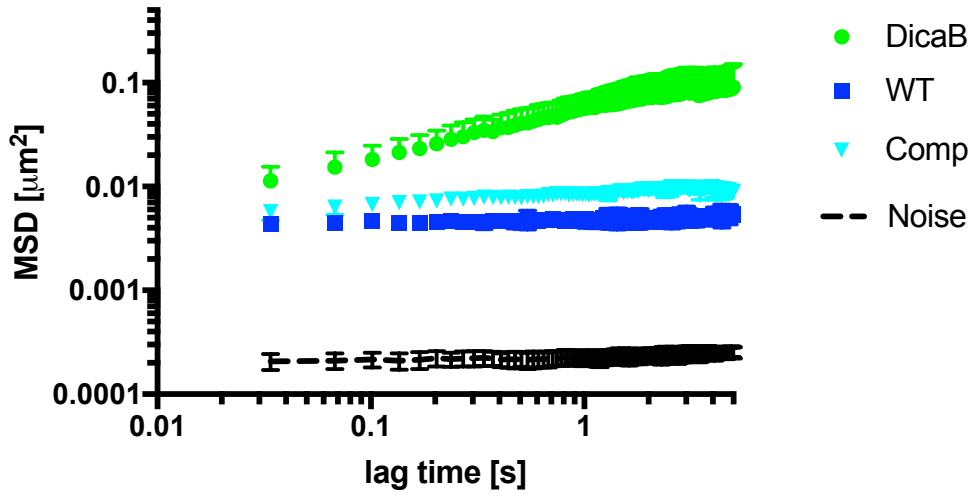

Figure 4-6 | Mean square displacements of bacterial cells of wild-type (WT), Δ$icaB$ and Δ$icaB$ + pTX$icaB$ at the mid time point. Error bars indicate standard deviation of five replicates.

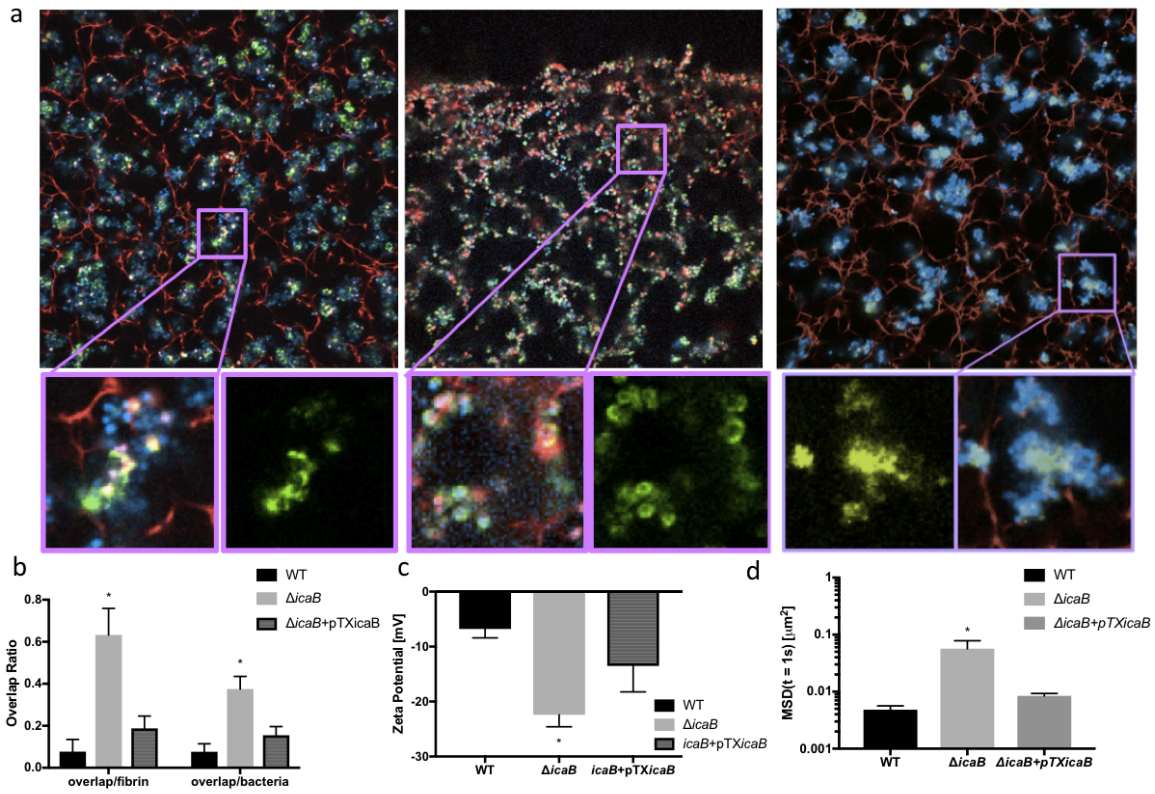

Figure 4-7 | Bacterial localization relative to fibrin fibers

(a) Confocal microscopy singles stacks of fibrin infected with wild-type (left), Δ$icaB$ (middle) and Δ$icaB$ + pTX$icaB$ (right) at the mid time point after fibrin network initiation. Red indicates fibrin, blue indicates bacteria and green indicates PIA. The top row shows the zoomed-in images of regions in the large image and the corresponding channel with only PIA on the right. (b) Fibrin-bacteria overlap ratio as compared to whole fibrin area (left) and whole bacterial area (right). Error bars indicate standard deviation of five replicates. (c) Zeta potential of stationary phase wild-type (WT), Δ$icaB$ and Δ$icaB$ + pTX$icaB$. Error bars indicate standard deviation of eight replicates. (d) Mean square displacements at t=1s of bacterial cells of wild-type (WT), Δ$icaB$ and Δ$icaB$ + pTX$icaB$. Error bars indicate standard deviation of three replicates. Asterix indicates statistical significance.

4.4.4 Δ$icaB$ has an increased sspA expression in fibrin

Figure 4-8 reports the *sspA* expression of the wild type, Δ$icaB$ and Δ$icaB$ + pTX$icaB$ growing with and without fibrin. At the mid time point, there is no difference in the wild type *sspA*

expression growing with and without fibrin, with the fold increase (with fibrin *versus* without fibrin) being 1.3 ± 0.9. No significant change is noticed in the *sspA* expression of the $\Delta icaB$ and the wild type when both grow without fibrin, with the fold increase ($\Delta icaB$ *versus* the wild type) being 0.9 ± 0.4. the fold increase of $\Delta icaB$ *versus* wild type growing in fibrin is 2.3 ± 1.1. The fold increase of $\Delta icaB$ growing with *versus* without fibrin is 3.4 ± 1.9. Statistics indicate that both are significantly above 1 ($P<0.05$).

Meanwhile, none of the conditions displays a significant increase in *sspA* expression when the wild type is compared to $\Delta icaB +$ pTX*icaB,* as shown in Figure 4-8b. The fold increase of wild type growing with *versus* without fibrin, $\Delta icaB +$ pTX*icaB versus* wild type growing without fibrin, $\Delta icaB +$ pTX*icaB versus* wild type growing with fibrin and $\Delta icaB +$ pTX*icaB* growing with fibrin *versus* without fibrin are 1.2 ± 0.7, 1.4 ± 0.8, 1.1 ± 0.4 and 1.1 ± 0.5, respectively. Thus, $\Delta icaB$ has an increased *sspA* expression in fibrin both compared to $\Delta icaB$ growing without fibrin and compared to wild type growing in fibrin.

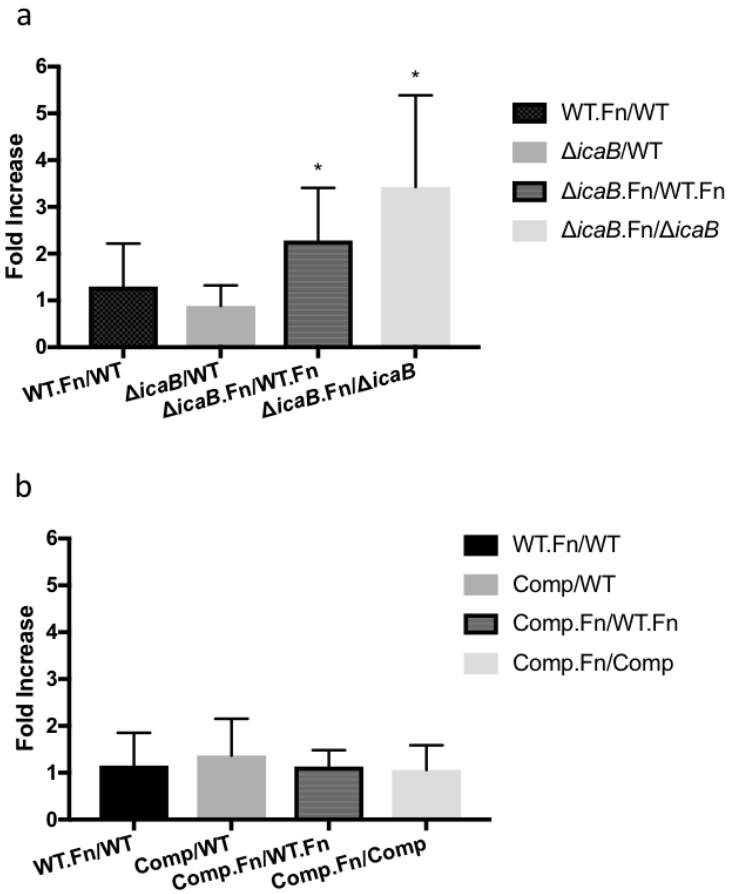

Figure 4-8 | Comparison of sspA expression under different conditions

(a) Fold increase of *sspA* expression of wild-type (WT) and the Δ$icaB$ growing with and without fibrin at the mid time point. WT = wild-type; WT.Fn = wild type in fibrin; Δ$icaB$.Fn = Δ$icaB$ in fibrin. For example, WT.Fn/WT means the fold increase of the wild type *sspA* expression growing with fibrin *versus* growing without fibrin. (b) Fold increase of *sspA* expression of wild-type and Δ$icaB$ + pTX$icaB$ in biofilms and in fibrin. Comp = Δ$icaB$ + pTX$icaB$; Comp.Fn = Δ$icaB$ + pTX$icaB$ in fibrin. Statistics indicates none of the compared fold increases are significantly above 1 ($P<0.05$). Error bars indicate standard deviation of seven replicates in both (a) and (b). Asterix indicates statistical significance. RNA samples were partially extracted by Janice Sim.

4.5 Discussion:

This study compares an *S. epidermidis* Δ$icaB$ with the wild type to investigate how the deacetylation and the introduction of positive charges to PIA molecules by IcaB influences

bacterial interaction with a fibrin network. We find that without IcaB, the bacteria co-localize onto the fibrin network, express more *sspA,* and degrade fibrin to a higher degree both structurally and mechanically relative to wild type. Here we consider potential explanations of the observations and discussion implications for staphylococcal behaviors and human disease.

We speculate that the capacity of bacteria to co-localize onto strands of the fibrin network is a key contributor in the cell's capacity to induce structural degradation of fibrin network into patches. In Figure 4-2, we show that at the endpoint time, an entire fibrin network infected with $\Delta icaB$ has almost been degraded into patches whereas a great portion of a fibrin infected with the wild type are still branches. In Figure 4-9, we show the images of bacteria together with fibrin at the endpoint time. For the wild type and $\Delta icaB$ + pTX$icaB$, we see that the fibrin branch-region is bacteria-free and the fibrin patchy-region overlaps with the bacterial patches. The $\Delta icaB$, on the other hand, grow on the fibrin fibers much earlier (at least no later than the mid time point as shown in Figure 4-7) and that could be the reason of why $\Delta icaB$ degrades a fibrin faster. At the endpoint time, both the fibrin patches and the $\Delta icaB$ cells are evenly distributed as shown in Figure 4-9.

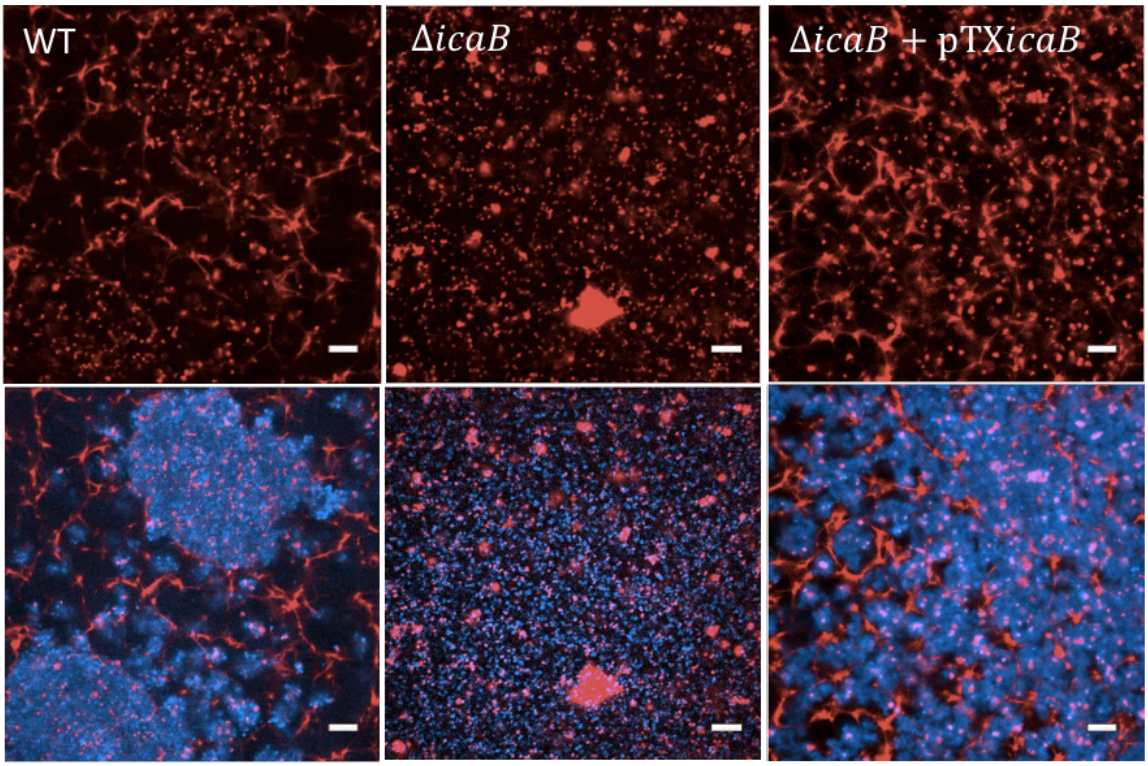

Figure 4-9 | Single stacks of confocal microscopy of wild-type, DicaB and DicaB (pTXicaB) (from left to right) at the ending time point after clot initiation. Red indicate fibrin, blue indicates bacteria.

Structurally, at the endpoint time, we observe changes from branched pattern to patchy pattern in the morphology of fibrin infected with both wild type and $\Delta icaB$. Mechanically, however, only the fibrin network infected with $\Delta icaB$ has a significant change as shown in Figure 4-5. The images in Figure 4-9 indicates that the wild type bacteria degrade the co-localized fibrin and incorporate themselves – a biofilm cluster – into the fibrin network. The wild type MSD values reported in Figure 4-7d and its MSD curve in Figure 4-7, which agrees with that measured by Stewart.et.al.[27], shows that a wild type cluster is an elastic solid with every cell being restricted by the biofilm they form. Therefore, the fibrin structurally degraded by the wild type still remains as a connected network behaving like a solid. The slight drop of the creep compliance value may be caused by the addition of mass (biofilm clusters) to the material. On the other hand, the fibrin infected with the $\Delta icaB$ may not be a connected network anymore at the endpoint time

because first, the degree of degradation is significantly higher than that of the wild type (Figure 4-2b) and second, the Δ$icaB$ cells are mobile and diffusive – more like planktonic cells with no mechanical contribution (Figure 4-7d and Figure 4-6).

From Figure 4-7, we hypothesis that cell surfaces with strong negative charge and diffusive cell populations are factors in the co-localization of bacteria and the fibrin network. Fibrin is positively charged[17]. Therefore, a negatively charged cell surface would be attractive to the fibrin fibers. In the meanwhile, only a mobile and diffusive cell – the Δ$icaB$ – could have the opportunity to be attracted to the fibrin. IcaB has been shown to be a significant factor in biofilm formation. Without IcaB, PIA may not be able to bind the cells with each other to form a biofilm community[8]. Thus, the Δ$icaB$, being both mobile and diffusive, behaves more like a planktonic cell. Whereas, a cell in the wild type is constrained in the biofilm clusters and may not have the chance to bind onto a fibrin fiber. As a biofilm-former, a newborn cell would be stick onto other cells in the cluster[9] rather than onto fibrin fibers.

A limitation of the zeta potential measurement is the difference in the experimental conditions. The measurements of zeta potential are performed on planktonic stationary-phase cells cultured at 200rpm (c.f. Methods). The PIA produced by the Δ$icaB$ could be in the solvent as suggested by Vuong et.al.[8]. However, in Figure 4-7a, we see the Δ$icaB$ cells are surrounded by PIA. This could be due to the no-shaking in the experimental condition. Nevertheless, the PIA molecules surround the Δ$icaB$ cells without deacetylation are negative, whereas the PIA molecules sticking to the wild type cell surfaces have positive charges. Regardlessly, we speculate that the extra negative charges on the cell surface may not be a necessity for the co-localization of the Δ$icaB$

cells and the fibrin fibers – the difference in mobility may be enough to generate the difference in cell location relative to fibrin fibers.

We studied a $\Delta icaB$ complement strain – $\Delta icaB + \text{pTX}icaB$ – to ensure that plasmid expression of icaB recovers the effects created by the. Judging from the results of fibrin patch percentage (Figure 4-2b), infected fibrin mechanics (Figure 4-5), bacteria-fibrin overlap ratio (Figure 4-7b), zeta potential (Figure 4-7c) and cell mobility (Figure 4-7d), the complement strain does not fully recover the effect caused by the all the way to wild type, although only the zeta potential of the complement strain is significantly different than the wild type ($P<0.0005$). This consistency may further suggest the causality of zeta potential and cell mobility to bacteria-fibrin overlap ratio and that of the bacteria-fibrin overlap ratio to fibrin morphologic and mechanical changes. This partial recovery may be due to that the culturing condition could not keep all the bacteria expressing the plasmid correctly.

This study addressed the role of the IcaB – the deacetylation and the introduction of positive charges to the PIA molecules – in bacterial interaction with a fibrin network. The deficiency of one surface protein – IcaB – could resolve in changes of bacterial behaviors in host protein networks, including their relative location to the host network, cell mobility and gene expressions. This further leads to a different influence on the integrity of the host network. Our finding that the $\Delta icaB$ co-localizes with the fibrin fibers and degrades a fibrin significantly faster than the wild type would contribute to the current understanding of the co-existence and the interaction between bacteria and host protein networks. The bacterial influence on fibrin integrity could be related to thromboembolism, which motivates future *in vivo* studies.

4.6 Reference

1. Mack D*, et al.* The intercellular adhesin involved in biofilm accumulation of Staphylococcus epidermidis is a linear beta-1, 6-linked glucosaminoglycan: purification and structural analysis. *Journal of Bacteriology* **178**, 175-183 (1996).

2. Flemming H-C, Wingender J. The biofilm matrix. *Nature Reviews Microbiology* **8**, 623 (2010).

3. Vuong C, Otto M. Staphylococcus epidermidis infections. *Microbes and infection* **4**, 481-489 (2002).

4. Heilmann C, Schweitzer O, Gerke C, Vanittanakom N, Mack D, Götz F. Molecular basis of intercellular adhesion in the biofilm- forming Staphylococcus epidermidis. *Molecular microbiology* **20**, 1083-1091 (1996).

5. Cramton SE, Gerke C, Schnell NF, Nichols WW, Götz F. The intercellular adhesion (ica) locus is present in Staphylococcus aureus and is required for biofilm formation. *Infection and immunity* **67**, 5427-5433 (1999).

6. Gerke C, Kraft A, Süßmuth R, Schweitzer O, Götz F. Characterization of theN-Acetylglucosaminyltransferase Activity Involved in the Biosynthesis of the StaphylococcusepidermidisPolysaccharide Intercellular Adhesin. *Journal of Biological Chemistry* **273**, 18586-18593 (1998).

7. Zhang YQ*, et al.* Genome- based analysis of virulence genes in a non- biofilm- forming Staphylococcus epidermidis strain (ATCC 12228). *Molecular microbiology* **49**, 1577-1593 (2003).

8. Vuong C*, et al.* A crucial role for exopolysaccharide modification in bacterial biofilm formation, immune evasion, and virulence. *Journal of Biological Chemistry* **279**, 54881-54886 (2004).

9. Otto M. Staphylococcus epidermidis—the'accidental'pathogen. *Nature Reviews Microbiology* **7**, 555 (2009).

10. VanEpps JS, Younger JG. Implantable Device-Related Infection. *Shock (Augusta, Ga)* **46**, 597-608 (2016).

11. Raad II, Luna M, Khalil S-AM, Costerton JW, Lam C, Bodey GP. The relationship between the thrombotic and infectious complications of central venous catheters. *Jama* **271**, 1014-1016 (1994).

12. Brackman G, Meyer L, Nelis H, Coenye T. Biofilm inhibitory and eradicating activity of wound care products against Staphylococcus aureus and Staphylococcus epidermidis

biofilms in an in vitro chronic wound model. *Journal of applied microbiology* **114**, 1833-1842 (2013).

13. Ryan EA, Mockros LF, Weisel JW, Lorand L. Structural origins of fibrin clot rheology. *Biophysical journal* **77**, 2813-2826 (1999).

14. de Cagny HC*, et al.* Porosity governs normal stresses in polymer gels. *Physical review letters* **117**, 217802 (2016).

15. Wassarman KM. Small RNAs in bacteria: diverse regulators of gene expression in response to environmental changes. *Cell* **109**, 141-144 (2002).

16. Nickerson NN, Prasad L, Jacob L, Delbaere LT, McGavin MJ. Activation of the SspA serine protease zymogen of Staphylococcus aureus proceeds through unique variations of a trypsinogen-like mechanism and is dependent on both autocatalytic and metalloprotease-specific processing. *Journal of Biological Chemistry* **282**, 34129-34138 (2007).

17. Ma TM, VanEpps JS, Solomon MJ. Structure, Mechanics, and Instability of Fibrin Clot Infected with Staphylococcus epidermidis. *Biophysical journal* **113**, 2100-2109 (2017).

18. Weisel J. Structure of fibrin: impact on clot stability. *Journal of Thrombosis and Haemostasis* **5**, 116-124 (2007).

19. Whiting D, DiNardo JA. TEG and ROTEM: technology and clinical applications. *American journal of hematology* **89**, 228-232 (2014).

20. Samama M-M. An epidemiologic study of risk factors for deep vein thrombosis in medical outpatients: the Sirius study. *Archives of internal medicine* **160**, 3415-3420 (2000).

21. Dalager-Pedersen M, Søgaard M, Schønheyder HC, Thomsen RW, Baron JA, Nielsen H. Venous thromboembolism after community-acquired bacteraemia: a 20-year Danish cohort study. *PloS one* **9**, e86094 (2014).

22. Grau AJ*, et al.* Clinical and biochemical analysis in infection-associated stroke. *Stroke; a journal of cerebral circulation* **26**, 1520-1526 (1995).

23. Peschel A, Ottenwälder B, Götz F. Inducible production and cellular location of the epidermin biosynthetic enzyme EpiB using an improved staphylococcal expression system. *FEMS microbiology letters* **137**, 279-284 (1996).

24. Valentine M*, et al.* Colloid surface chemistry critically affects multiple particle tracking measurements of biomaterials. *Biophysical journal* **86**, 4004-4014 (2004).

25. Cicuta P, Donald AM. Microrheology: a review of the method and applications. *Soft Matter* **3**, 1449-1455 (2007).

26. Mason T, Ganesan K, Van Zanten J, Wirtz D, Kuo S. Particle tracking microrheology of complex fluids. *Physical review letters* **79**, 3282 (1997).

27. Stewart EJ, Ganesan M, Younger JG, Solomon MJ. Artificial biofilms establish the role of matrix interactions in staphylococcal biofilm assembly and disassembly. *Scientific reports* **5**, 13081 (2015).

Chapter 5: Hydrogel materials as rheometer tooling for the transient delivery of additives during mechanical rheometry[4]

5.1 Abstract:

Mechanical rheology is widely applied to study soft matter; however, the transient rheological properties of these materials are often sensitive to additives in a way that is difficult to study because of the challenge in their delivery *in situ*. Because it is of interest to study the transient rheology of self-assembled soft matter as such additives diffuse into the material and generate microstructural and physicochemical changes, we have developed rheometer tooling comprised of a porous hydrogel. The tooling allows additives to be dosed through a rheometer plate or cone, and the consequent effect of these additives on a material's mechanical response measured. The disposable hydrogel rheometer plate is synthesized by means of the photopolymerization of an aqueous polyethylene glycol (PEG) diacrylate solution. We precisely control the dimensions of the rheometer tool and accommodate shrinkage, by fixing the mold to a five-axis optomechanical stage, which specifies the pitch, yaw, and translational position of the tool relative to its rotational axis. We demonstrate the performance of the tooling by measuring the viscoelastic properties of aqueous polyethylene oxide (PEO) solutions and comparing the values to those obtained using standard, stainless steel fixtures. We measure the diffusion of small molecules –

[4] The work of Chapter 5 is in preparation of publication as "Hydrogel materials as rheometer tooling for the transient delivery of additives during mechanical rheometry" by **Tianhui Ma**, Megan Szakasits, Peng-Kai Kao, J. Scott VanEpps, and Michael Solomon

NaCl in this case – through the hydrogel material, to confirm its function and characterize the time scale over which additives can be delivered. We apply the hydrogel fixture to dose self-assembled soft matter and gels with additives, and thereby demonstrate that the tooling can be used to study the kinetics of material property variation due to the diffusion of molecular additives into the soft material though the hydrogel plate. Examples materials studied are solutions of colloids and proteins, with the additives dosed being salts and enzymes.

5.2 Introduction:

Mechanical rheology is used to study the flow and mechanical properties of complex fluids; the effects of additives on the transient rheology of these materials have scientific and technological importance. Instances of additive effects on soft matter rheology are common. For example, the transient rheology of colloidal suspensions during gelation is important in many industries [1]. Other examples in which transient measurements are important include the addition of thickeners, gelling agents, and emulsifiers to food products [2], the use of reactive polymeric materials as rheology modifiers of lubricating greases in the oil industry [3], and the control over ionic strength in micelle solutions to change the flow properties in consumer products [4]. Turning to biological systems, protein solutions are sensitive to salinity, pH as well as chaotropic and kosmotropic agents, etc. There is furthermore interest in studying the transient rheology of protein networks formed through enzymatic process. An example of such a transient process would include blood clot fibrinolysis as plasmin diffuses into and dissolves a clot [5] and the interactions between blood clots and continuously growing bacterial biofilms[6]. The blood clot in this case is principally comprised of a fibrin polymer network. It is produced by means of enzymes (i.e., thrombin) and degraded by another enzyme (i.e., plasmin) [7]

Rheological properties are of course sensitive to other environmental factors such as temperature and light, as well as electric and magnetic fields. Mechanical rheometers are well equipped for *in situ* study of the effects of these factors on rheology through the development of tooling that is e.g., transparent, equipped with Peltier or other elements. On the other hand, current rheological methods have limited capabilities to study the transient rheology that results from the dosage of molecular additives. Currently, to conduct such measurements, components must be mixed *ex situ*. The mixture is then loaded onto the rheometer. Potential problems with this technique include: difficulty in establishing an initial time point for the additive dosing; uncontrolled deformation during the loading of the material – during which time the additive is functional – onto the rheometer; loss of the few minutes of data while the specimen is being loaded onto the rheometer.

As example, the formation of colloidal gels can be sensitive to the addition of salt [1]. In weakly aggregated colloidal gels, mixing the sample and loading it onto the rheometer can disrupt the gel network, because it is weak. Therefore, it is of interest to study the transient rheology of gelation due to salt ion diffusion into the sample under *in situ* conditions.

As an additional example, consider the fact that the enzyme plasmin dissolves fibrin networks, as the primary structural constituent of blood clot. To observe the transient rheological signature of such degradation, the network first must be synthesized under *in situ* conditions, Three components – fibrinogen (the monomers that build the fibrin network), thrombin (the enzyme that triggers the fibrin network polymerization) and plasmin – must be mixed together to

polymerize fibrinogen into fibrin network. However, this current procedure measures the effect plasmin on a forming fibrin network, not how plasmin diffuses in and dissolves a completely formed fibrin network, which is a more physiologically relevant scenario [5].

To address needs of this kind,, in this paper we design, build, and test rheometer tooling that allows for the *in situ* diffusion of additives into specimens during rheological measurement. The availability of such fixtures will improve the scope for rheological characterization of materials that are sensitive to the introduction of molecular additives.

Few methods for *in situ* dosing of additives during rheometry have been previously developed. Pavlovsky et al., modified a commercial rheometer into a continuously fed bioreactor that allows the study of bacterial biofilm properties under different growth conditions by steady flow of media across the extended gap of a parallel-plate rheometer. However, this set-up did not allow simultaneous rheometry and additive dosing, because the media flow occurred for gap dimensions larger than typical of rheometry[8].

Boyer et al., applied a porous plate (hole size = 5mm covered by 200um Nylon mesh) to study the rheology of dense particle suspensions. Since liquid can freely flow in and out of the holes, sample volume and particle volume fraction can vary during the measurements [9] in response to osmotic pressure or normal force differences. This method differs somewhat from the aim here of the *in situ* delivery of molecules to a rheological specimen.

On the other hand, specimens for microrheology, a technique that uses the dynamics of passive or active probes to characterize the viscoelasticity of the microenvironment in which the probes

are dispersed, can be configured to allow for additive delivery. For example, Schultz et al., applied microrheology to study the degradation of hydrogel in response to cell-secreted enzymes by tracking the Brownian motion of the embedded probe particles (carboxylated polystyrene probes) [10]. Similarly, Sato and Breeveld studied the transient rheology of solvent-responsive complex fluids via microrheology by introducing and tracking the fluorescent particles in the fluids [11]. Nevertheless, such measurements have limitations on the macroscopic level.

Another method to configure rheometer tooling is to 3D print the fixtures, as described by D.A.Bikos and T.G.Mason, et.al [12]. In this work,,tooling comprised of disposable plastic was designed and 3D printed to allow volume matching, uniform strain field, higher torque and greater control over tooling surface roughness. While this method produces customizable tooling, the material selections demonstrated to date does not accommodate *in situ* delivery of additives during rheometry, as addressed in the present work.

Hydrogels are widely used in both scientific and industrial settings [13] [14]. Their porosity and biocompatibility have found applications as tissue scaffolds [13]. At the same time, the stiffness of hydrogels is also controllable [14]. Hydrogels have been 3D printed to provide materials with spatially controlled functionality [15]. Because of their specific combinations of porosity and rigidity, hydrogels have been used as a solid membrane for the diffusion of additives [16]. Therefore, hydrogels are an excellent candidate material to create rheometer tooling that is both porous – to allow diffusion of additives during measurement – and rigid – to allow mechanical rheometry.

In this paper, we present the synthesis of a rheometer fixture made of a rigid, porous hydrogel that allows for transient delivery of additives during mechanical rheometry. We characterize the stiffness of the hydrogel material and its permeability to ionic, molecular, and protein solutions. The utility of the hydrogel fixture for rheometry is established by comparing its performance to that of commercial, stainless steel, rheometry tooling for the measurement of the rheological properties of complex fluids. We also illustrate two applications of the fixture in which the hydrogel tooling is used to study the kinetics of material rheology due to the diffusion of molecular additives through the hydrogel plate.

5.3 Materials and Methods:

5.3.1 Study Design

Here we present the conceptual design of the hydrogel rheometry tooling for the delivery of molecules during the rheological measurements. First, we develop a hydrogel that is both rigid and permeable. Second, we present ways to use the hydrogel tooling with commercially available rheometers. We offer two approaches: one is simple and quick to execute; the other is more laborious to implement, but yields tooling alignment that is configured to ~14 micron precision. Third, we deploy test solutions to demonstrate 1) the performance of the hydrogel tooling as compared to commercial ones; 2) examples of application of the hydrogel tooling to address needs for transient rheology of materials in the presence of additives delivered *in situ*. Finally, we present the development of a hydrogel fixture for cone and plate rheometry.

5.3.2 Hydrogel Plate Design and Production

The hydrogel material for the rheometer tooling is synthesized by photopolymerization of 33.2 wt. % poly(ethylene glycol) diacrylate (PEGDA) (MW 750), 66.4 wt. % water, and 0.4 wt. %

photoinitiator, 2-hydroxy-2-methyl-propiophenone. This aqueous pre-hydrogel solution is mixed and rolled overnight. A hydrogel plate is generated by first pouring this aqueous solution into a glass ring mold (c.f. Figure 5-1a,b), made from cut glass tubes, placed on either a petri dish or a glass slide and then illuminating UV light from beneath for two minutes. Shrinkage appears after the solution polymerizes into a hydrogel plate. Hydrogel plates generated by glass ring molds with an inner-diameter = 54 mm and 43.5 mm are measured to be 53.0 ± 0.1 mm and 43.0 ± 0.1 mm, respectively.

The stiffness of the synthesized hydrogel is measured on a RSA3 Dynamic Mechanical Analyzer (TA Instruments). A three-point bending method is used and the converted tensile stress is found to be $77 \pm 14kPa$ (n = 3).

5.3.3 Visually-Aligned Rheometer Tooling

The following simple procedure was used to produce hydrogel tooling with concentricity alignment error of $0.5 \pm 0.04\ mm$ (n=3), as measured in ImageJ. We first used a visual aligning method to incorporate the hydrogel plate onto a rheometer for a parallel plate geometry. The hydrogel plate is formed around a steel cone tooling (20mm in diameter, 2°) as a spindle to the rheometer. As shown in Figure 5-1, we visually align the glass ring with the outer circle on the template and the spindle with the inner circle. After alignment, the template is removed, and the aqueous pre-hydrogel solution is poured into the glass ring mold to make a hydrogel plate with the desired thickness (typically ~ 5 mm). The product together with the glass ring and the bottom petri dish is then rinsed with water and the hydrogel tooling is carefully removed from the glass ring. We attach the hydrogel plate tooling onto a commercial rheometer, which is easily

accomplished because the hydrogel material has been gelled around the standard commercial plate. A solvent trap and humidifier is used to keep the hydrogel plate hydrated during the tooling setup and the experiments.

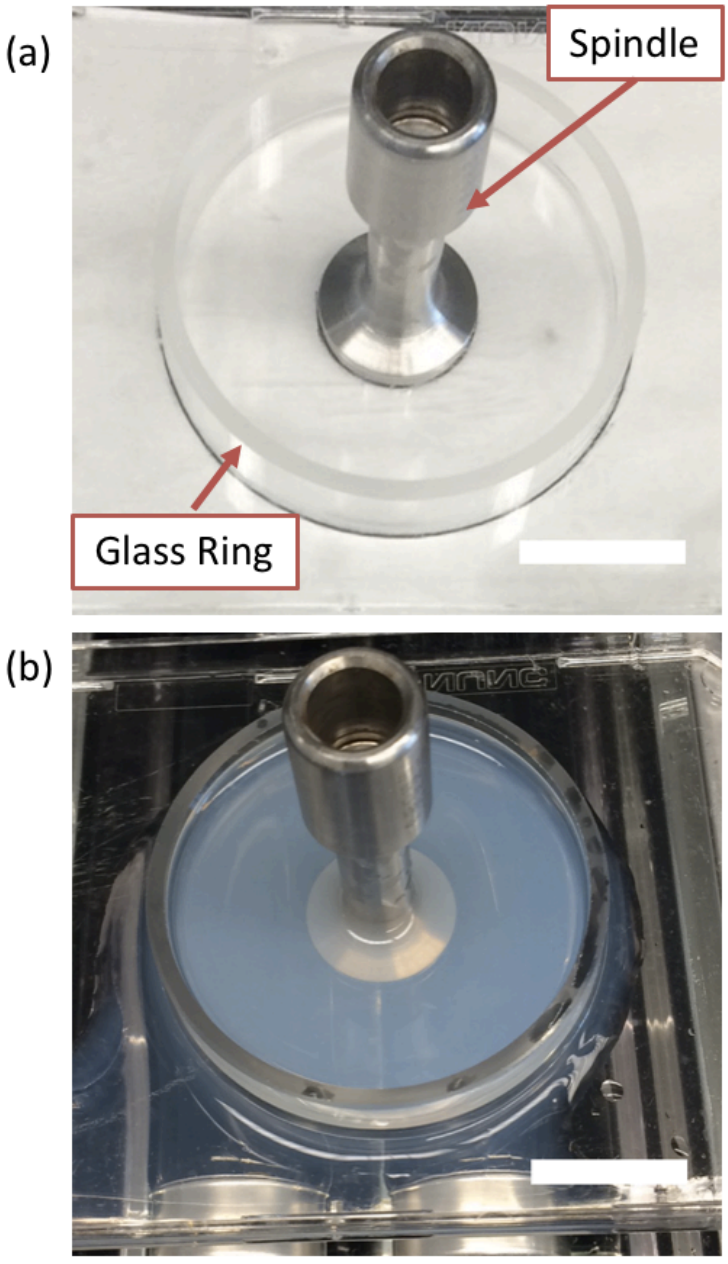

Figure 5-1 | Visually-Aligned Hydrogel Tooling

(a) A photo taken to show the alignment of the glass ring and the spindle (a commercial cone 20mm in diameter for rheometry) with a template beneath. (b) A photo to show a hydrogel plate after generation. Scale bar = 20 cm. This method was developed together with Megan Szakasits.

5.3.4 Mechanically Aligned Rheometry Tooling

The following procedure was used to produce a hydrogel tooling with concentricity alignment of precision $14\mu m$. To generate a hydrogel tooling with precise alignment, five dimensions are specified relative to the central rotational spindle of the rheometer, as shown in Figure 5-2a. These dimensions are the plate-spindle tilt control – $\theta, \emptyset$ to specify the orthoganality of the plate relative the spindle – and the x, y, z control to align the center of plate relative to the spindle axis. Figure 5-2b shows the procedure to find the center of the ring to locate the spindle. To control the five dimensions, we incorporate the tilt control and the z control from a commercial rheometer (Figure 5-2c). The spindle used is a steel cone (25mm in diameter, 2°, Anton Paar). The spindle is first attached to the rheometer. The configuration of the rheometer itself ensures that the spindle stays perpendicular to the bottom stage. A UV light is placed on the bottom stage. A glass slide is placed on top of the UV light for the fabrication of the hydrogel plate. In the zoomed-in photo in Figure 5-2c, a level is placed on the UV light to show the bottom plate where a hydrogel plate will be generated remains flat. Two micrometers that control the x, y dimension of the glass ring mold are fixed onto the bottom stage, which is also an optical table. First, we roughly locate the glass ring in the middle of the spindle. Then we set zero gap of the spindle relative to the bottom glass slide. We then translate the spindle to 0.5mm above the glass slide. Applying the method described in Figure 5-2b, we locate the glass ring mold to the center of the spindle. A humidifier and solvent trap are again used to control the humidity. Although the hydrogel plates were re-generated for each replicate in this study, the hydrogel tooling can also be stored in water for reuse.

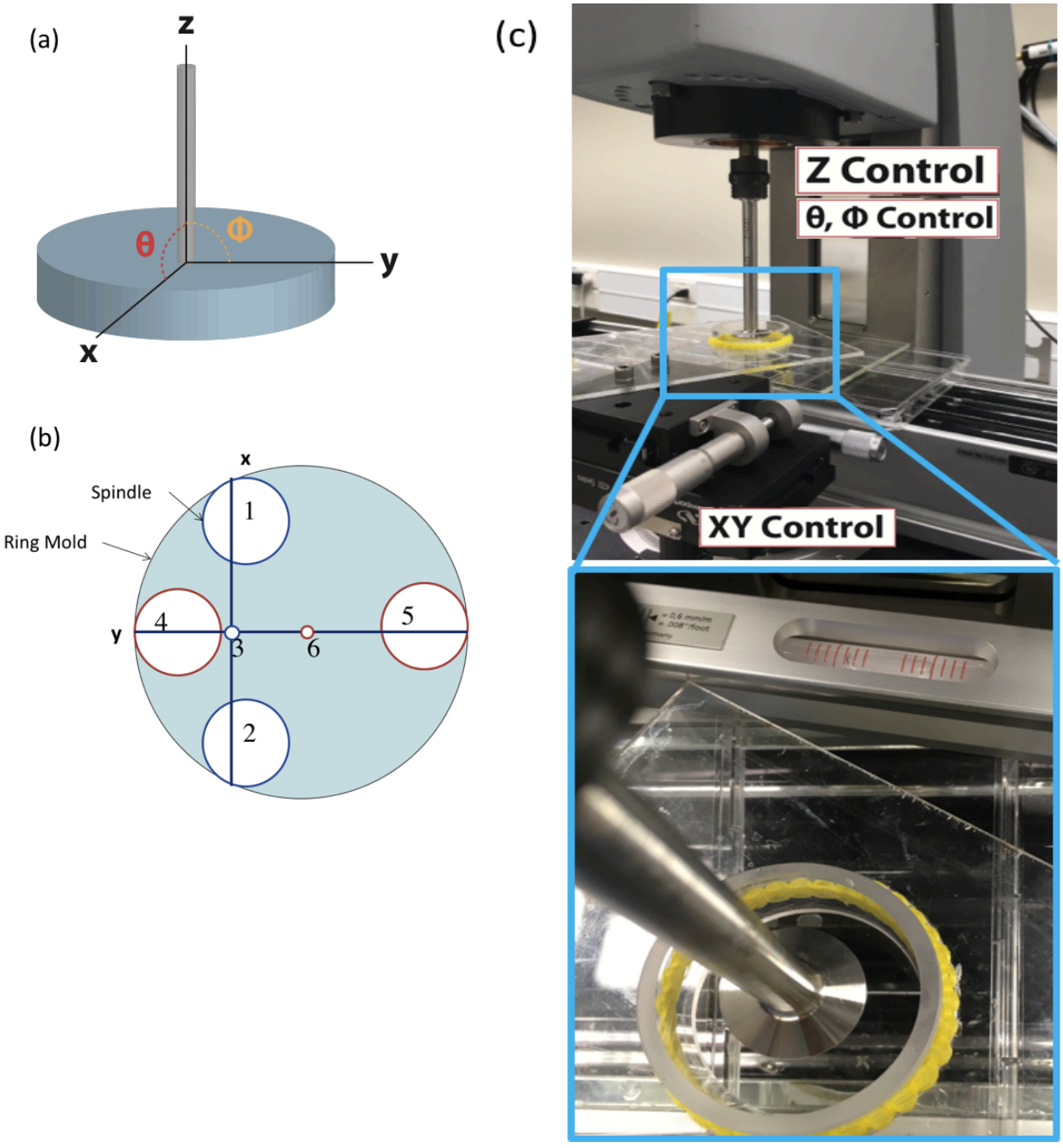

Figure 5-2 | Mechanically-Aligned Hydrogel Plate Tooling

(a) Schematic showing the five dimensions to control for the hydrogel plate production: spatial dimensions x, y, z and tilt angles θ and $\emptyset$. (b) Schematic illustrating the procedure to find the center of a circle so as to locate the spindle to the center of the glass ring mold. The outer large ring indicates the glass ring mold; the inner small rings indicates the spindle. The spindle starts

from position 1, where it touches the edge of the glass ring, moving by controlling a micrometer along the x axis to position 2, where it touches the ring again. Calculate the position of the middle of 1 and 2 and define it as position 3; starting from 3, along the y axis, move the spindle to position 4 and then position 5, the middle of 4 and 5 is defined as position 6, which is the center of the circle. (c) Photograph of the rheometer tooling. From top to bottom: z and tilt control provided by commercial rheometer, the glass ring mold, micrometer for x,y control. The zoomed-in image shows a level confirming that the bottom surface is level. This method was developed together with Megan Szakasits and Peng-Kai Kao.

5.3.5 Test solutions

A 4.0 wt.% polyethylene oxide (PEO) (Mn = 1,000,000) (Polyscience, Inc.) is used to compare the accuracy of the hydrogel tooling with standard stainless steel tooling for rheometry. PEO powder is dissolved in deionized (DI) water and rolled for three days before use. Gellan gum (Phytagel^{TM}, Bioreagent, plant cell culture tested, powder, Sigma-Aldrich) solution (0.75 wt.% with 250mM NaCl in deionized (DI) water) is made and used to run transient creep tests.

To demonstrate an application of the hydrogel fixture, a polystyrene colloidal gel is produced. The colloidal suspension is 1.5 wt.% carboxylate-modified polystyrene colloids of $1\mu m$ in diameter (ThermoFisher Scientific). It is prepared by washing the particles three times in DI water (twice at 5000G for 10min and once at 5000G for 15min) and resuspended in a mixture of H_2O (DI water) and D_2O (ThermoFisher Scientific) with a ratio of 3:7, to match the density of the particles. Magnesium chloride ($MgCl_2$) was used to aggregate the polystyrene colloidal solutions into gels. A commercial $MgCl_2$ solution (BioUltra, for molecular biology, Sigma-Aldrich) is diluted from 2.0M to 80mM, and then added to the colloidal suspension.

In the other application, we measure the rheology of fibrin network degradation via diffusion of plasmin. The fibrin network is formed from platelet-poor-plasma. New Zealand White rabbit

whole blood was collected into citrate tubes right after euthanasia. Within one hour, whole blood samples were centrifuged (3000g, 5min) to yield platelet-poor-plasma. Coagulation was initiated by adding calcium chloride (3mM final concentration). Plasmin aliquots were made by dissolving the lyophilized human plasmin (Plasmin, EACA- and Lysine-Free, Human Plasma, Millipore Sigma) in filtered deionized (DI) water (Milli-Q® Type 1 Ultrapure Water Systems, Millipore Sigma). A 0.33U/ml plasmin solution was made by diluting the plasmin aliquots with Hanks' Balanced Salt Solution (HBSS) (1X, without phenol red, with calcium, with magnesium).

5.3.6 Dosage of additive solutions

The aqueous pre-hydrogel solution in the glass ring mold has a curved surface at the top because of how the solution wets the glass ring. This interface yields a shallow bowl on top of the hydrogel plate after the photopolymerization. For a hydrogel plate of 53 mm in diameter, the maximum volume of liquid this shallow bowl can reliably hold is ~ 2 ml. This depression is used as a reservoir to contain additive solutions to be dosed to the specimen. That is, the additive solution is spread evenly on top of the hydrogel plate in the shallow bowl to initiate additive delivery through the hydrogel plate below in the application examples. For the corresponding control experiments, the reservoir is filled with DI water.

Hydrogel is synthesized with the same composition has been proven to be permeable; it has been used as a membrane in literature [16]. We conducted an experiment to measure the rate of $MgCl_2$ diffusion through a hydrogel plate 4mm in thickness. The hydrogel plate is supported in a 400ml glass beaker, which is filled with..DI water until its surface touches the bottom of hydrogel plate. An 80mM $MgCl_2$ solution of 0.8ml is carefully spread on the top surface of the hydrogel plate.

An Orion Star™ A212 Conductivity Benchtop Meter with an Orion™ DuraProbe™ 4-Electrode Conductivity Cell (Thermo Fisher Scientific, Waltham, MA, USA) is used to measure the conductivity of the water beneath the hydrogel plate. This measurement indicates the quantity of salt ions that have diffused through the hydrogel plate into the water beneath. A stir bar rotates at 300rpm during the measurement. The beaker is covered with plastic wrap to prevent the evaporation.

To show the permeability of plasmin through the hydrogel plate, an enzyme-linked immunosorbent assay (ELISA) is performed. Human PLG / Plasmin / Plasminogen ELISA Kit (Sandwich ELISA) (LifeSpan BioSciences, Inc.) is used in this study according to the manufacturer's instructions. A standard curve (Figure 5-3) is generated to convert optical density at 450nm measured by an EnSpire Multimode Plate Reader (PerkinElmer) to plasmin concentration. Hydrogel plates of 4mm in thickness are supported in a petri dish (60mm in diameter, 15mm in height, polystyrene, Falcon, Corning). DI water (22ml) is poured into the petri dish so that the water surface touches the bottom of the hydrogel plate. The 0.33U/ml plasmin solution (1ml) is loaded on top of the hydrogel. After 2.5 hours, ~300μl of the liquid beneath the bottom surface of the hydrogel plate is sampled. This liquid is tested with ELISA and the final concentration is determined from the standard curve (Figure 5-3).

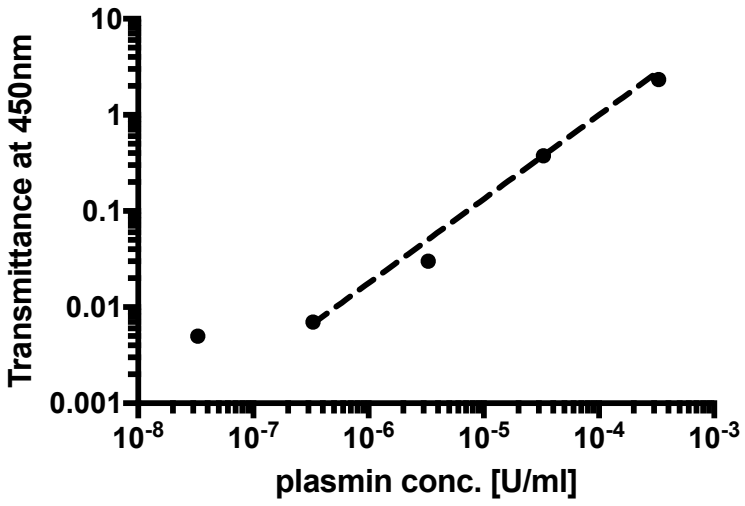

Figure 5-3 | Standard curve of plasmin concentration measured by ELISA

The relationship between the transmittance and the plasmin concentration (with 3.3×10^{-8} excluded) is regressed: Plasmin conc. $= 1\times10^{-4} * transmittance^{1.143}$, the dotted line indicates. Transmittance readings of four replicates in the experiment of plasmin diffusing through hydrogel were 0.182, 0.052, 0.089 and 0.079.

5.3.7 Rheometry

Three different types of rheometers (AR-G2, TA Instruments; Discovery HR-2, TA Instruments; MCR 702 rheometer, Anton Paar) are used to test the performance of hydrogel plates generated by the two methods. The tests include small amplitude oscillatory shear as a function of frequency and creep tests in the linear regime. For kinetic tests, small amplitude oscillatory shear was performed at a frequency $\omega = 0.1$ Hz with a strain amplitude in the linear regime. Experiments were performed in a humid environment. As necessary, sample desiccation was prevented by coating sample edges with a thin layer of mineral oil.

5.3.8 Hydrogel Cone Generation

To create a hydrogel cone, a bottom mold complementary to the cone shape is designed in OpenSCAD (Marius Kintel, Clifford Wolf) and generated by three-dimensional (3D) printing (3D Systems, Viper Stereo-Lithography): 54mm in diameter, 2° in cone angle, $60\mu m$ in truncate gap. Accura 60 – a transparent, polycarbonate-like plastic – is used as the 3D printing material because of its favorable UV transmittance. To generate the hydrogel cone fixture, the 3D-printed bottom mold replaces the flat petri dish or glass slide in the procedure described earlier. For evaluation, we take photos and detect the edge of the cone in Python 3.6.4 as shown in Figure 7(b). The beveled side of the cone is fitted with a line by linear regression and the R-square value is calculated. The conical surface is also detected and fitted with a line. The angle of the cone is then calculated to be the angle of between the two lines.

5.4 Results:

5.4.1 Hydrogel Plate Performance

In Figure 5-4a, we compare the small amplitude oscillatory shear of a 4.0 wt% PEO solution, as characterized using the hydrogel plate geometry, as generated by visual alignment (c.f. Methods), and a commercial stainless steel plate. The measurement gap is 500 μm the strain amplitude of 0.30 is within the linear regime of this material. The values of G' and G'' measured with the hydrogel plate agree well with that measured with the stainless steel tooling. Averaging over the whole curve, the mean relative error between the two fixtures is 17% for G' and 10% for G''.

In Figure 5-4b, the measured creep response is reported. It is characteristic of a viscoelastic liquid. The agreement between the results for the two hydrogen and stainless steel plates is very good. At the start of the creep test, oscillations in the compliance, also known as inertio-elastic

"ringing," are observed. This response results from the coupling of instrument inertia and sample elasticity [17]. The instrument inertia calibration before every experiment for both the hydrogel plate and the stainless steel plate is done following the manufacturer protocol, which measures the acceleration at a constant torque [18]. The overlap of the curves measured by the hydrogel plate and the commercial plate shows that the effect of the hydrogel plate instrument inertia is the same as from the stainless steel fixture. It also shows the precision of the hydrogel plate in measuring transient rheological response.

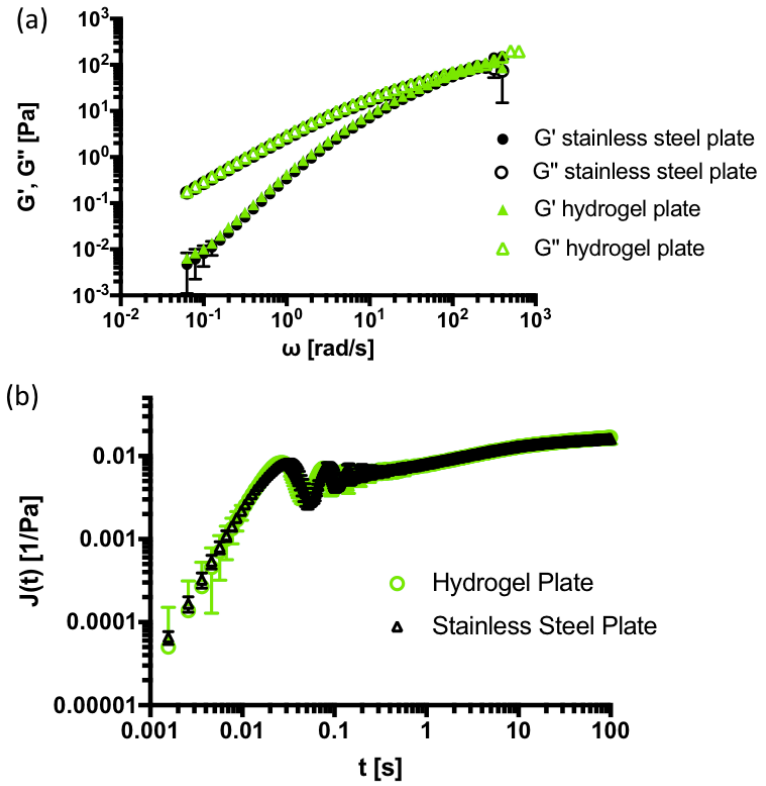

Figure 5-4 | Rheometric tests comparing a stainless steel plate (60mm in diameter) and a hydrogel plate (53mm in diameter), as produced by the visual alignment method

(a) Linear viscoelastic response of a 4.0 wt.% PEO solution at $\gamma = 0.3$. (b) Transient creep tests of 0.75 wt.% gellan gum solution at fixed stress τ_0= 10Pa and gap = 500μm.

We compare the rheometry measurements of a 4wt.% PEO solution using a commercial glass plate (Anton Paar) and a hydrogel plate centered by mechanical alignment. Both the small-amplitude oscillatory shear rheology results (Figure 5-5a) and the transient creep test results (Figure 5-5b) show excellent agreement between the performance of the hydrogel plate and the glass plate. In this case the mean relative error is 8.6% for G' and 7.9% for G".

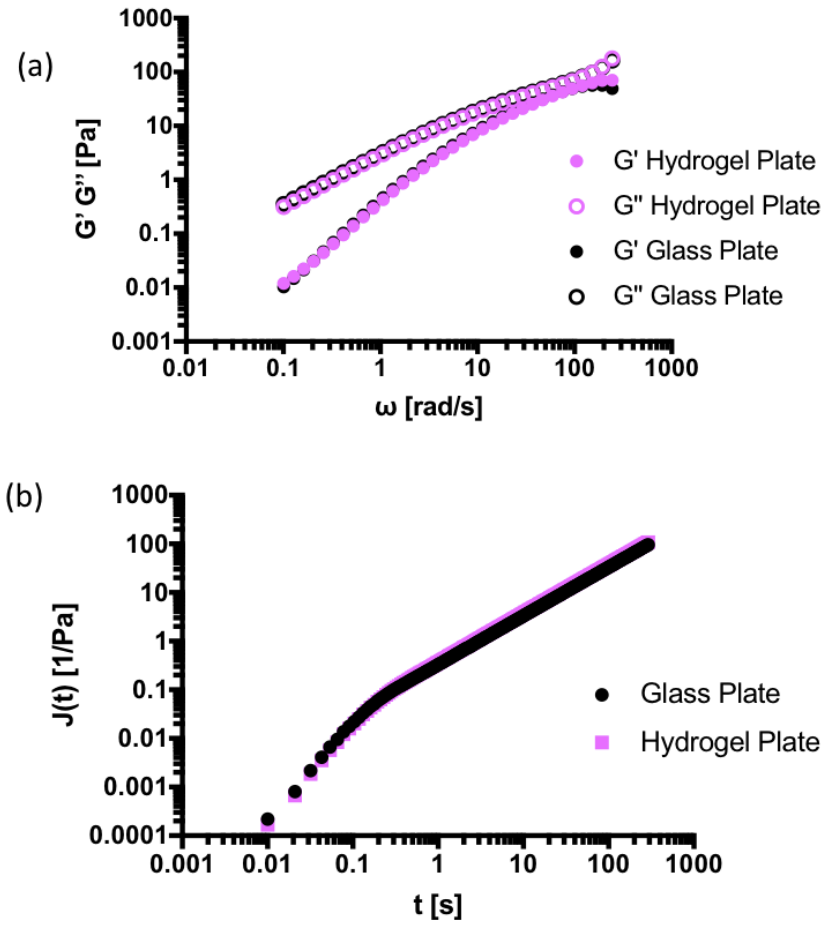

Figure 5-5 | Rheometric tests of a 4 wt.% PEO solution comparing a glass plate (43mm in diameter from Anton Paar) and a mechanically aligned hydrogel plate (43mm in diameter)

(a) Frequency sweeps at fixed $\gamma = 0.3$. (b) Transient creep tests, at fixed stress τ_0= 10Pa, gap = 500μm.

5.4.2 Applications

Here we report two example applications of the porous hydrogel tooling for rheological measurements. In the first application, we deliver salt ions through the hydrogel plate to a colloidal suspension while measuring its change in G' during the colloidal gelation.

We first show the permeability of $MgCl_2$ through the hydrogel plate by loading the $MgCl_2$ solution on top of the hydrogel plate and measuring the conductivity change over time in the water beneath the hydrogel. The transport of salt ions through the hydrogel plate is driven by the concentration gradient since the salt concentration on top of the hydrogel plate is high and the concentration in the water beneath the hydrogel plate is initially zero. As shown in Figure 5-6a and 5b, initially there is no significant change in the conductivity of the water beneath the hydrogel. After about two hours, there is a sudden increase. The conductivity continues to increase, until it slows down and approaches a plateau. The two-hour lag time before significant increase in conductivity is consistent with diffusion through the hydrogel. Specifically, an ion of diffusivity $3.3\times10^{-11}\ mm^2/min$ requires 120 min to traverse the 4 mm thickness of the hydrogel.

In Figure 5-6, we show how the diffusion of salt ions triggers a colloidal gelation process as characterized by measurement of the elastic modulus, G'. Without salt ions, G' of the colloidal suspension is essentially noise, with an average value of $0.04 \pm 0.03Pa$. When the salt ions diffuse into the colloidal suspension with a profile shown in Figure 5b, the G' value of the colloidal suspension remains as noise with an average value of $0.08 \pm 0.04Pa$ for $101 \pm 17\ min$ before the start of the gelation, which we define as time zero. The G' value then

increases from around $0.08 \pm 0.04Pa$ to $1.5 \pm 0.8Pa$ 6000 seconds after time zero. This result indicates the successful delivery of salt ions through the hydrogel rheometry tooling.

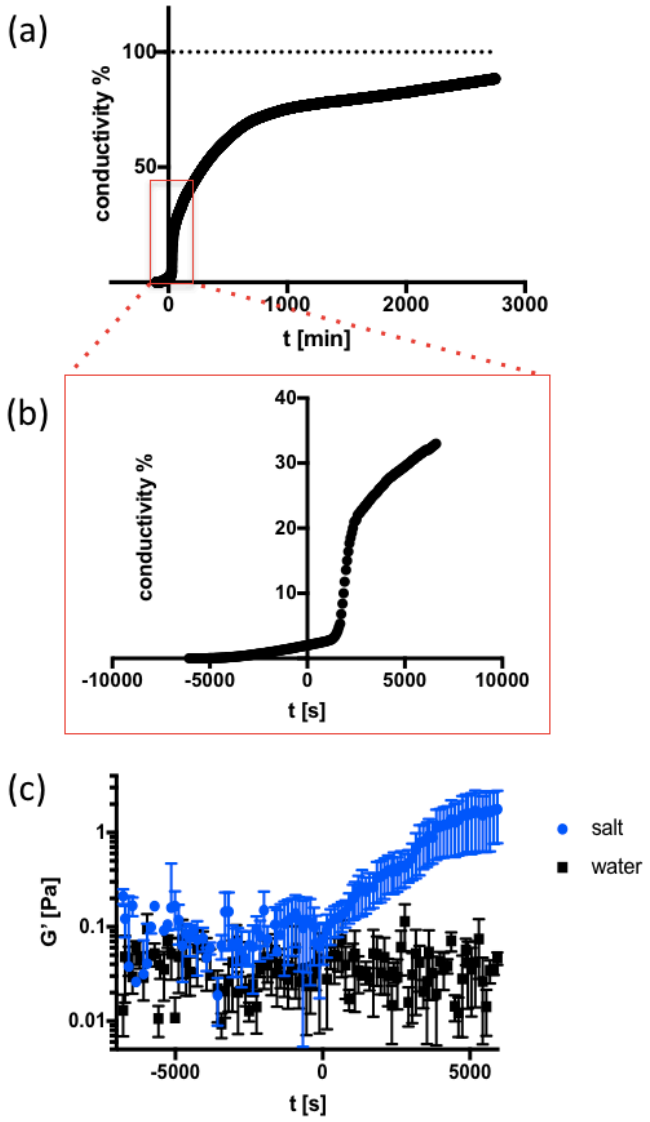

Figure 5-6 | Colloidal gelation triggered by salt diffusion through porous hydrogel rheometer plate

(a) The change of conductivity over time in the water beneath the hydrogel plate with 0.8ml 80mM MgCl2 solution loaded on top of the hydrogel fixture. The conductivity is normalized with the maximum conductivity when all the loaded salt solution is mixed in the water. (b) Detail of change of conductivity in the first four hours. (c) The time-dependent linear elastic modulus, G', at fixed strain = 0.003, for $1\mu m$ colloidal polystyrene suspension loaded beneath the hydrogel plate and 0.8ml 80mM MgCl2 (blue points) or 0.8ml DI water (black points) loaded on top.

Time zero is defined as the start of the colloidal gelation and is taken as the point in which the change in G' value (moving average of five points) is continuously increasing. Error bars indicate standard error of the mean of three replicates; the increase in modulus indicates gelation.

In the other application, we deliver a fibrinolytic enzyme – plasmin – through the hydrogel to a fibrin network and measure the linear elastic modulus during fibrin network degradation. Under the conditions of this experiment, plasmin concentration in the sample under the hydrogel plate after 2.5 hours is determined to be $(1.4 \pm 0.9)\times10^{-4}$ U/ml. As showed in Figure 5-7, without plasmin, the G' value initially increases rapidly when the fibrinogen in the plasma solution polymerizes into a fibrin network triggered by the calcium chloride. G' then reaches a plateau of $66 \pm 4Pa$. When plasmin is loaded on top of the hydrogel plate, the G' value also initially increases due to fibrin network formation; after around two hours, the G' value starts to decrease and reaches a lower plateau ($G'\sim16 \pm 10Pa$) at around three hours. The decrease in elastic modulus confirms the delivery of plasmin through the hydrogel fixture.

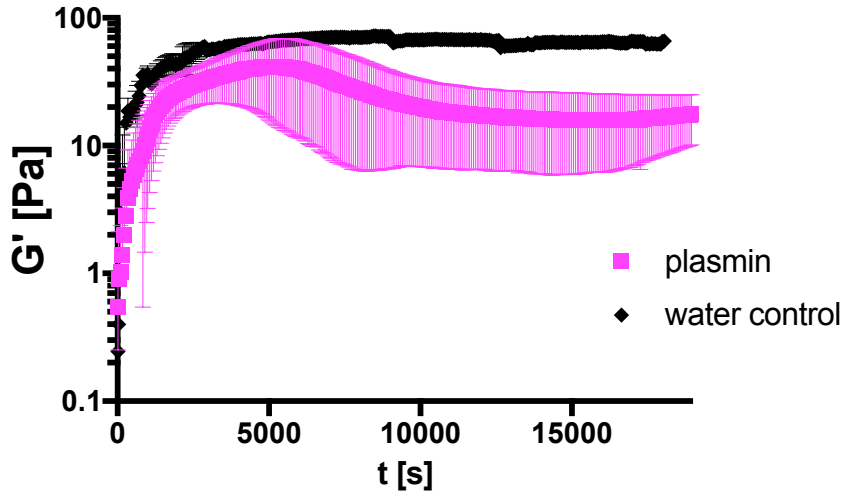

Figure 5-7 | The linear elastic modulus of a fibrin network degraded by plasmin via diffusion through the hydrogel membrane

The change of the elastic modulus, G', over time with platelet-poor-plasma loaded beneath the hydrogel plate (initiated at time 0 with calcium chloride) and 1ml 0.33U/ml plasmin solution or 1ml DI water loaded on top. Error bars indicate standard deviation of three replicates.

5.4.3 Hydrogel Cone and Plate Fixture

Figure 5-8 shows the hydrogel cone produced using a 3D printed mold (c.f. Methods). The edge of the cone is detected by image analysis in Figure 7(b). We fit the the edges to lines by linear regression ($R^2 = 0.9 \pm 0.04$, n=3) and calculate the cone angle (2.5 ± 0.5, n=3) (c.f. Methods). Figure 7(c) shows its performance for rheological characterization is also shown. The G' and G'' values measured by the hydrogel cone match well with those measured with a stainless steel cone. The frequency range of characterization is three decades.

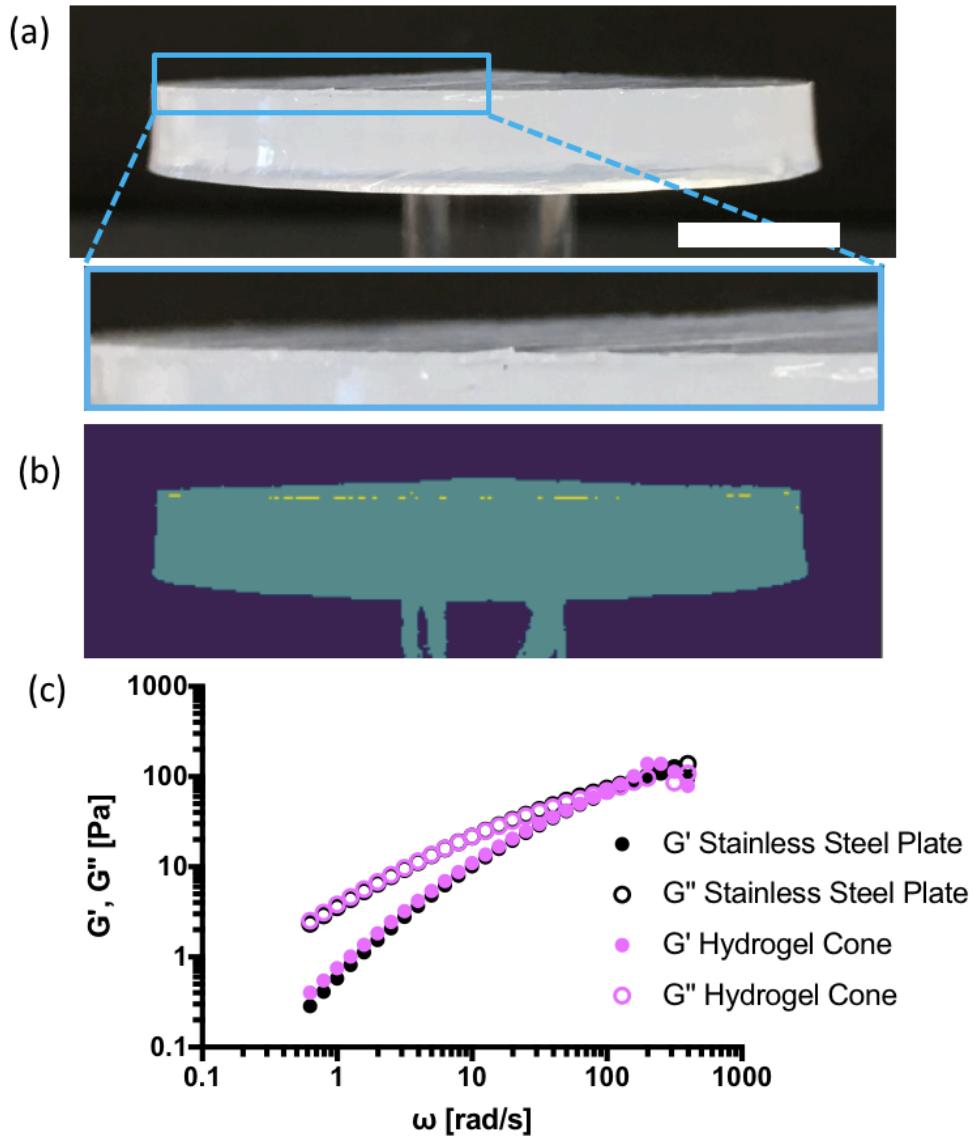

Figure 5-8 | Hydrogel cone and plate geometry

(a) An image of a hydrogel cone generated with the 3D-printed bottom mold. The red lines indicate the cone angle. Scale bar = 10 cm. The cone angle is measured to be 2°. (b) The edge of the cone plate detected by image analysis in Python. (c) A comparison of frequency sweeps of a 4.0 wt.% PEO solution measured with a steel cone and a hydrogel cone, produced using the visual alignment method.

5.5 Discussion:

In this study, we report the development of hydrogel geometries for rheometry that allow the delivery of additives across the rheometer fixture and into the sample during measurements. We first showed that the performance of the hydrogel plate geometry is as good as both glass and stainless steel plates in oscillatory viscoelasticity and transient rheology (creep) measurements. We then offered two examples of applications in which salt ions were delivered to a colloidal suspension so as to gel it and plasmin was delivered to a fibrin network so as to degrade it. The kinetic response of the rheology to these changes could be directly monitored because of the *in situ* delivery. We finally report that the same approach can be used to produce a permeable hydrogel cone and plate geometry, with the assistance of 3D printing. Overall, the hydrogel rheometer tooling opens up a wide range of possibilities for *in situ* delivery of additives during rheometry measurements in both scientific and industrial settings. Here we consider limitations of the method as well as potential future work that might promote additional applications of it.

One limitation of the hydrogel fixture is that it is sensitive to changes in ambient humidity, because of its high water content. Upon desiccation, the fixture becomes brittle, and it becomes more prone to cracking. Therefore, when working with the hydrogel tooling, it is important to control its aqueous content by soaking the hydrogel in water, using a humidifier, or applying a solvent trap. Fortunately, solvent traps and other devices to control humidity are increasingly standard features of rheometers. To illustrate the effects of desiccation, we repeated the conductivity measurement shown in Figure 5-6a and 5b with a hydrogel plate of the same thickness and diameter that had cracked due to desiccation. The result is shown in Figure 5-9. The conductivity begins to increase rapidly about 20 minutes after the salt solution is loaded on top of the hydrogel plate as opposed to two hours with a crack free hydrogel plate.

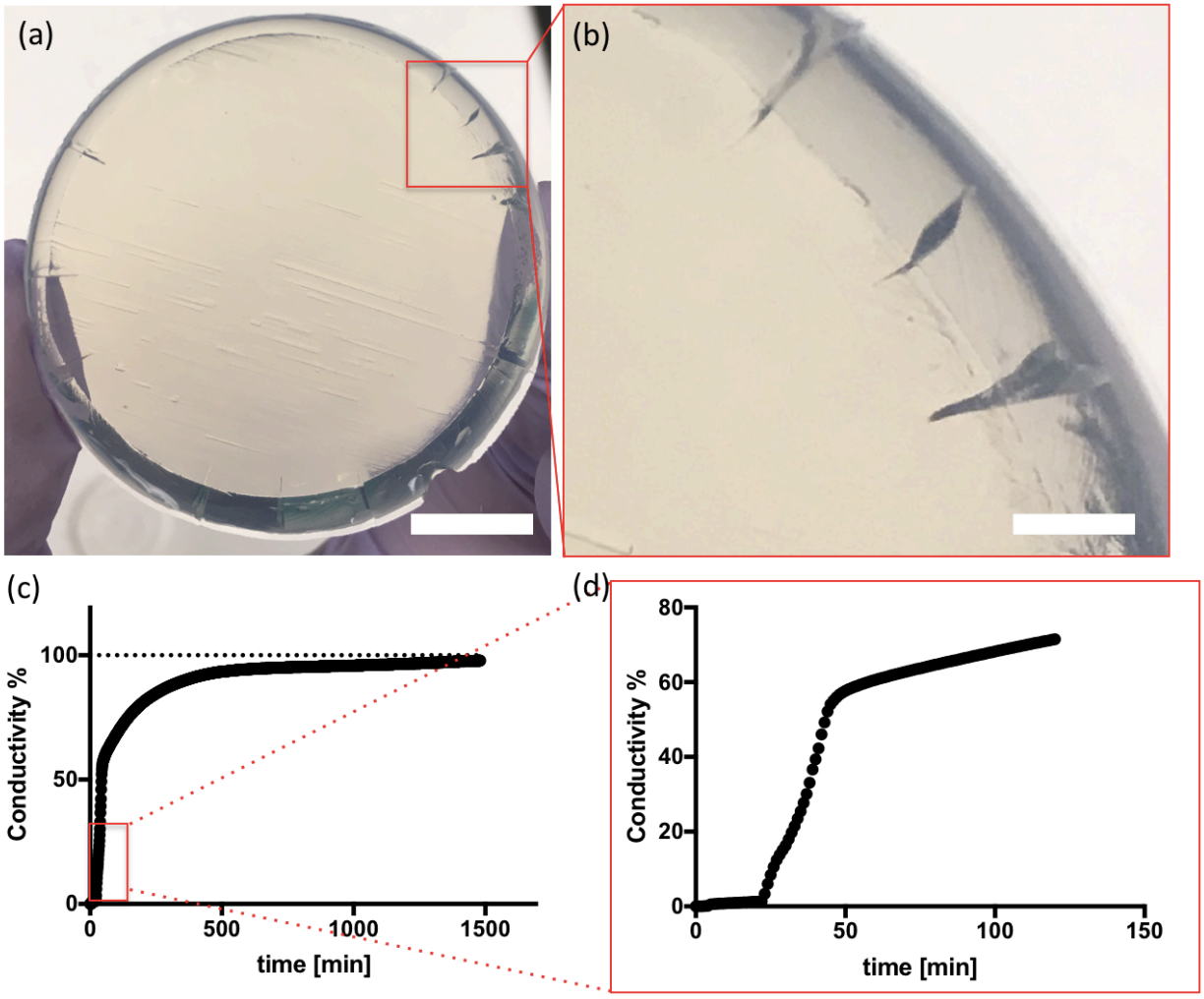

Figure 5-9 | The transient conductivity profile over time for a hydrogel plate with visible cracking, presented as comparison to the intact fixture of Figure 5-6

(a) Visible cracking of the hydrogel, scale bar = 10 cm; (b) zoomed-in image of the cracks, scale bar = 2 cm; (c) the change of conductivity over time a 400 ml reservoir beneath the hydrogel plate with 0.8ml 80mM $MgCl_2$ solution loaded on top of the cracked hydrogel plate shown in (a). The conductivity is normalized by the maximum conductivity. (b) The change of conductivity in the first two hours; to be compared to Figure 5-6a and 5-6b. The lag time before an obvious increases in conductivity is significantly shorter than a non-cracked hydrogel plate in Figure 5-6a,b.

A consequence of inadvertent fixture desiccation is thus that the delivery of the additive through the hydrogel will be compromised (or uncontrolled) due to heterogonous channels inside the

plate. Although sometimes the consequences of desiccation are cracks that are clearly visible, we should also concern ourselves with the possibility that the cracks might be microscopic. Dessication-induced cracking at the interface between the hydrogel of the fixture and the stainless steel spindle that is used to attach the fixture to the rheometer drive shaft is of particular concern.

Although the ambient humidity was carefully controlled and no cracks were observed in all the fixtures used here, we performed some auxiliary experiments to check for fixture micro-cracking. First, we soaked a hydrogel fixture for three hours in a food coloring solution and did not observe any micro-cracking due to enhanced coloration of the dye. Second, we observed a $5.3\times5.3\,mm^2$ section of a hydrogel plate fixture under 10X magnification, and also did not observe any micro-cracks. These additional results are shown in Figure 5-10.

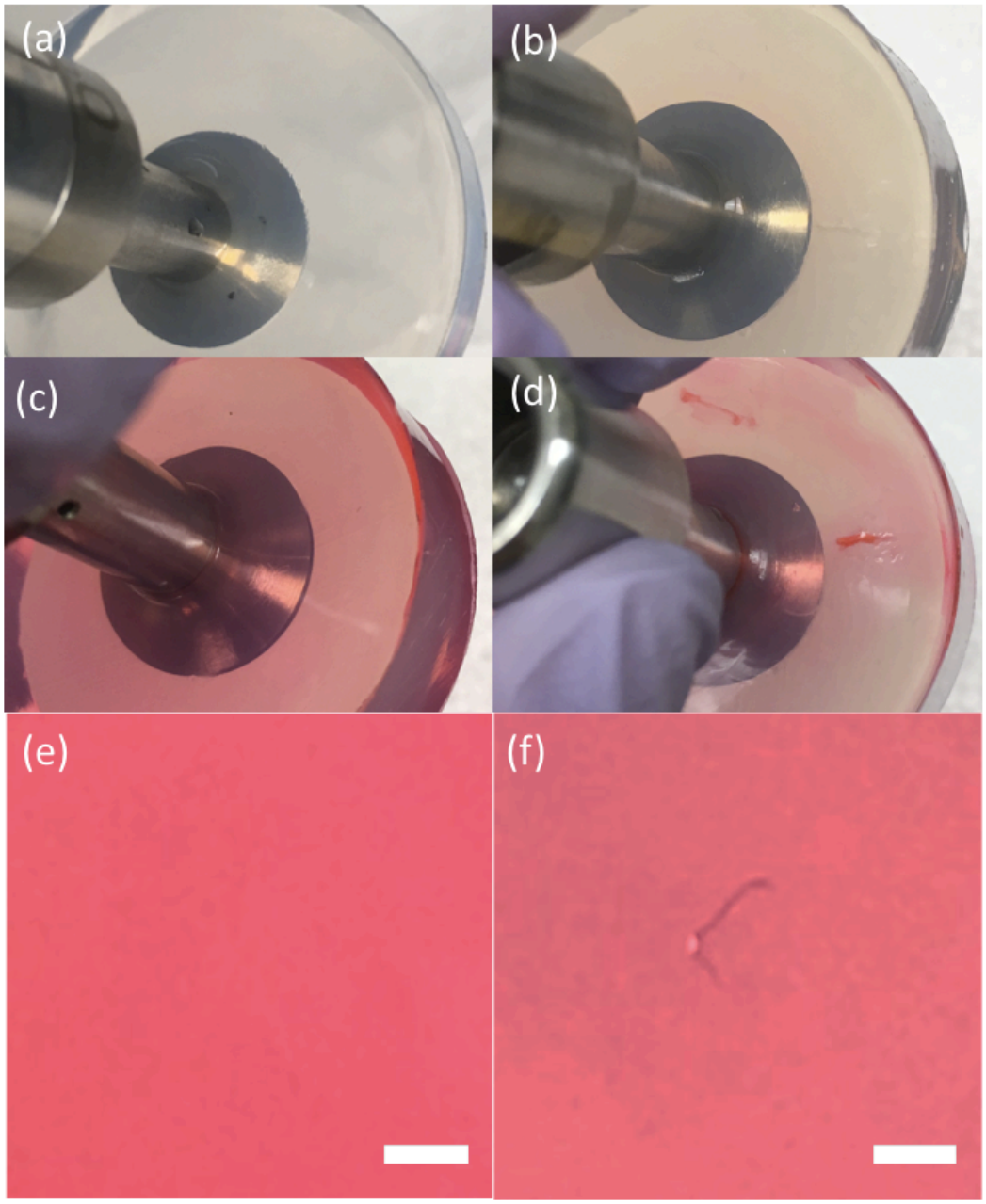

Figure 5-10 | Microcrack visualization

(a) Hydrogel plate (43mm in diameter) fixture produced under the experimental conditions in which humidity is properly controlled for three hours and (c) soaked in a food coloring solution for another three hours; no visible cracks or channels are detected; (b) fixture with artificially produced cracks by a blade and (d) dyed with food coloring to show that cracks become easier to see when dyed. A $5.3\times5.3\ mm^2$ section of a hydrogel plate fixture (e) with no visible cracks

detected and (f) with artificially cracked produced by a blade dyed with food coloring under 10X magnification. A Scale bar = 1mm.

Another limitation of the porous hydrogel tooling is the potential for vertical heterogeneity in the sample as a consequence of the time that it takes for the additive to diffuse through the sample itself. That is, since the additive diffuses through the hydrogel to the top surface of the sample, it may trigger change in the specimen at different times in planes perpendicular to the direction of diffusion. Thus, the real-time variation in mechanical properties measured this way is the change in the sample surface rather than an ensemble average of the whole sample. As an estimate of the significance of this effect, consider the time for a small species (e.g., Na+ and Cl- ions) to diffuse through the typical gap dimensions (e.g., 500 microns) of a parallel plate rheometry experiment. The characteristic time for diffusion across this distance is about 30 seconds for an aqueous solution. Therefore, kinetic effects on a specimen will be a convolution of the properties of the different axial slices for time scales less than this duration.

A potential limitation of the permeability of the hydrogel tooling is the existence of an osmotic pressure gradient across the hydrogel fixture, particular for delivery of salt solutions. A gradient of osmotic pressure may drive mass flux that would cause a change in the measured normal force over time. In Figure 5-11, we show that a 4 wt.% PEO solution has a gradual change in normal force during a steady shear test measured by hydrogel plate with salt solution loaded on top, as compared to that measured by a stainless steel plate and a hydrogel plate with water loaded on top. It suggests that there could be some effect of the osmotic pressure gradient across the membrane, which may influence the measured normal force.

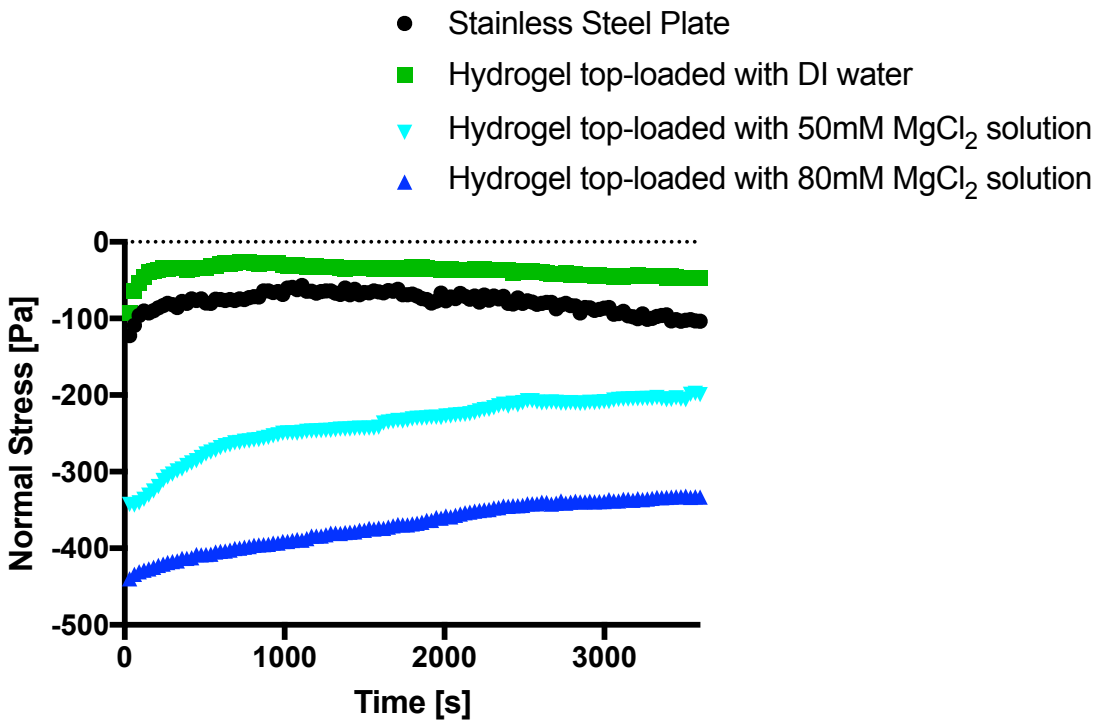

Figure 5-11 | Effect of osmotic pressure during the diffusion of salt ions.

Normal Stress over time during a steady shear test (shear rate = 0.1 s-1) of a 4 wt.% PEO solution measured with a stainless steel plate (20mm in diameter), hydrogel plate (53mm in diameter) with 1ml water and 1ml 80mM MgCl2 solution on top of the plate.

Because of its finite thickness, there is a lag between when the additive solution is first applied on top of the fixture, and when it first affects conditions of the specimen. We offer the following procedures to control this lag in delivery of the additive: 1) A simple way to speed up the delivery rate is to pre-soak the hydrogel plate in the additive solution to be delivered. In Figure 5-12, we pre-soak the hydrogel plate in an 80mM $MgCl_2$ solution overnight and repeat the experiment of Figure 5-6a and 5-6b. The pre-soaking leads to a faster initial delivery rate; 2) One could also control the thickness of the hydrogel plate to reduce initial lag times. In this study, the minimum thickness of the hydrogel plate is 4 mm. This thickness was needed so that the plate fully covered the spindle, which in the present case is a stainless steel cone with small

diameter. 3) Another way to address diffusion times across the hydrogel membrane would be to control the hydrogel pore size through variation of the concentration and the molecular weight of the PEGDA to vary the pore size of the hydrogel [19]. The concentration and type of the photoinitiator as well as the UV exposure time all play a role in controlling the pore size. 4) One could also vary the material to control the fixture permeability. To be selected as a porous rheometry tooling, a material would need to be rigid and permeable to an extent that allows the desired additive to traverse the fixture.

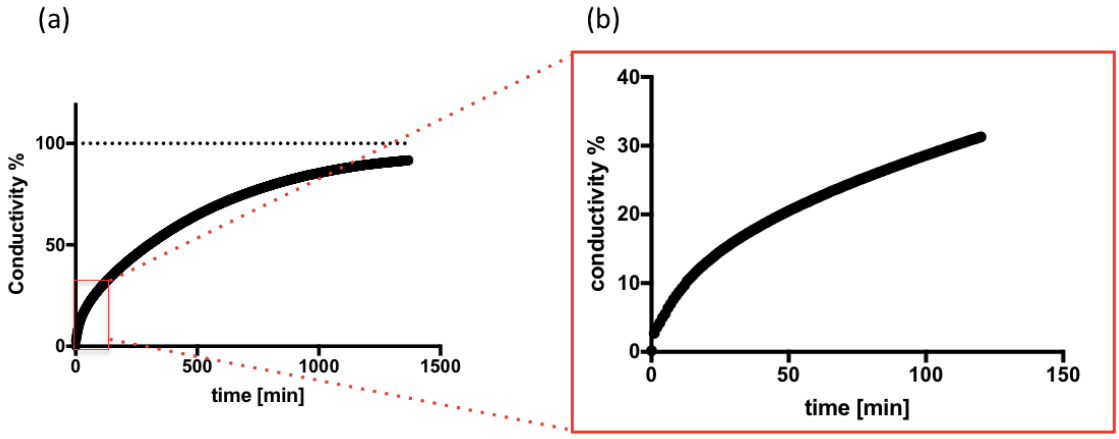

Figure 5-12 | The transient conductivity profile over time for hydrogel plate pre-soaked in the additive solution (80mM MgCl2) overnight

(a) The change of conductivity over time in the water beneath the hydrogel plate when 0.8ml 80mM $MgCl_2$ solution is then top-loaded. (c.f. Methods). The conductivity is normalized by the maximum conductivity. (b) The change of conductivity in the first two hours can be compared to Figure 5-6a and 5-6b in the main text. As opposed to the ~2 hours lag time before an obvious increases in conductivity in Figure 5-6a,b, the conductivity increases immediately at time zero when the hydrogel plate touches the DI water beneath.

5.6 Acknowledgement:

We acknowledge Dr. Timothy F. Scott for his early help with the development of the hydrogel plate. We acknowledge Toby Donajkowski and the Mechanical Engineering Undergraduate Additive Manufacturing Lab for the help with the 3D printing. We acknowledge the Chen Lab at the University of Michigan for the support of rabbit bood. This work was supported by NIH NIGMS (5R01GM081702) and NSF (CBET 1702418).

5.7 Reference

1. Zaccarelli E. Colloidal gels: equilibrium and non-equilibrium routes. *Journal of Physics: Condensed Matter* **19**, 323101 (2007).

2. Savage R. Effects of rheology modifiers on the flow curves of idealised and food suspensions. *Food Hydrocolloids* **14**, 209-215 (2000).

3. Moreno G, Valencia C, de Paz MV, Franco JM, Gallegos C. Use of Reactive Diisocyanate-Terminated Polymers as Rheology Modifiers of Lubricating Greases. *Industrial & Engineering Chemistry Research* **45**, 4001-4010 (2006).

4. Adams AA, Solomon MJ, Larson RG, Xia X. Concentration, salt and temperature dependence of strain hardening of step shear in CTAB/NaSal surfactant solutions. *Journal of Rheology* **61**, 967-977 (2017).

5. Kane KK. Fibrinolysis--a review. *Annals of clinical and laboratory science* **14**, 443-449 (1984).

6. Ma TM, VanEpps JS, Solomon MJ. Structure, Mechanics, and Instability of Fibrin Clot Infected with Staphylococcus epidermidis. *Biophysical Journal* **113**, 2100-2109.

7. Chapin JC, Hajjar KA. Fibrinolysis and the control of blood coagulation. *Blood reviews* **29**, 17-24 (2015).

8. Pavlovsky L, Younger JG, Solomon MJ. In situ rheology of Staphylococcus epidermidis bacterial biofilms. *Soft matter* **9**, 122-131 (2013).

9. Boyer F, Guazzelli É, Pouliquen O. Unifying suspension and granular rheology. *Physical Review Letters* **107**, 188301 (2011).

10. Schultz KM, Kyburz KA, Anseth KS. Measuring dynamic cell–material interactions and remodeling during 3D human mesenchymal stem cell migration in hydrogels. *Proceedings of the National Academy of Sciences* **112**, E3757-E3764 (2015).

11. Sato J, Breedveld V. Transient rheology of solvent-responsive complex fluids by integrating microrheology and microfluidics. *Journal of Rheology* **50**, 1-19 (2006).

12. Bikos DA, Mason TG. Customizable tool geometries by additive manufacturing for mechanical rheometry of soft matter. *Journal of Rheology* **60**, 1257-1267 (2016).

13. Hollister SJ. Porous scaffold design for tissue engineering. *Nature materials* **4**, 518 (2005).

14. Hassanzadeh P*, et al.* Ultrastrong and flexible hybrid hydrogels based on solution self-assembly of chitin nanofibers in gelatin methacryloyl (GelMA). *Journal of Materials Chemistry B* **4**, 2539-2543 (2016).

15. Hockaday L*, et al.* Rapid 3D printing of anatomically accurate and mechanically heterogeneous aortic valve hydrogel scaffolds. *Biofabrication* **4**, 035005 (2012).

16. Solomon M, Szakasits M, Zhang W. Dynamics of fractal cluster colloidal gels with embedded active Janus particles. In: *APS Meeting Abstracts* (ed^(eds) (2016).

17. Ewoldt RH, McKinley GH. Creep ringing in rheometry or how to deal with oft-discarded data in step stress tests! *Rheol Bull* **76**, (2007).

18. Franck AP. Importance of inertia correction for controlled stress rheometers A2 - Keunings, P. MoldenaersR *in Theoretical and Applied Rheology 1992, Elsevier: Amsterdam p 982-984*.

19. Cruise GM, Scharp DS, Hubbell JA. Characterization of permeability and network structure of interfacially photopolymerized poly (ethylene glycol) diacrylate hydrogels. *Biomaterials* **19**, 1287-1294 (1998).

Chapter 6: Conclusions and Future Work

The overall goal of this dissertation is to determine the impact of bacteria on the mechanics, structure and instability of a fibrin network in two limits of a spectrum of possibilities: In one limit, the role of bacterial cell growth is minimized by direct introduction of the physiologically relevant concentration of bacterial cells and then study of the effect of these cells on fibrin network formation. In the second limit, the role of fibrin network formation kinetics is minimized by pre-assembly of a fibrin network in which bacterial cells are then introduced and allowed to proliferate. The molecular mechanisms are also explored to aid in the understanding of the characterized phenomena.

In Chapter 2, we built an *in vitro* new model for medical device infection – that of a fibrin network infected with the common blood borne pathogen *Staphylococcus epidermidis*. We find that *S.epidermidis* influences a fibrin network mechanically and structurally on both microscopic and macroscopic scales. *S.epidermidis* present during clot formation produces a visibly disorganized microstructure that increases clot stiffness and triggers mechanical instability over time.

This work provides insight into clot heterogeneity shows that *S. epidermidis* can rupture a fibrin clot. The resultant embolization of the infected clot can contribute to the systemic dissemination

of the pathogen. This work has drawn attention on the role of host proteins on medical device infection in addition to bacterial biofilms. It inspired the research in the rest of my dissertation.

In Chapter 3, we explained a potential molecular mechanism that leads to the phenomena noticed in Chapter 2. We noticed that stationary-phase (biofilm-like) *S. epidermidis* has a more robust effect on fibrin formation kinetics, mechanics and structure than exponential-phase (planktonic) ones. We continued to find that stationary-phase *S. epidermidis* has an increased adhesion to fibrinogen. Furthermore, the gene expression for SdrG – the protein that adheres *S. epidermidis* cells to fibrinogen was significantly increased in the stationary phase. We therefore implied that bacterial interaction with fibrinogen could be a factor that determines bacterial effect on fibrin.

This work shows how the bacterial interaction with fibrin on a molecular scale could impact the formation, mechanics and structure of a host fibrin network. It also contributes to the current understanding of the growth phase dependent regulation of bacterial virulent factors and the correlation between bacterial infection and thrombosis.

In Chapter 4, the role of fibrin network formation kinetics is minimized by pre-assembly of a fibrin network in which bacterial cells are then introduced and allowed to proliferate into a biofilm. Under this scenario, we extended our study on infected fibrin by investigating a specific protein – *IcaB,* a cell surface-attached protein that has a key role in staphylococcal biofilm formation and immune evasion. It deacetylates and introduces positive charge to polysaccharide intercellular adhesin (PIA) molecules; these charges facilitate adhesion of bacterial cells within a biofilm cluster. We find that an *icaB* deletion mutant ($\Delta icaB$) degrades fibrin networks to a higher degree than the wild-type, both structurally and mechanically. Indeed, the $\Delta icaB$ produced more *sspA*, a protease that putatively degrades fibrin. We further demonstrate that the

$\Delta icaB$ cells, which are more mobile and diffusive than the wild type cells, co-localize with the fibrin fibers. This co-localization is correlated with fibrin network degradation.

This work suggests a pivotal role for *icaB* in modulating staphylococcal bacterial-fibrin interactions and resulting fibrin mechanical structure. This dynamic could be relevant to a potential molecular mechanism for infection-induced thromboembolism.

In our study of infected fibrin, we noticed some limitations in the mechanics characterization using rheometers, e.g. the challenge of delivering additives *in situ*. This inspired us to develop a rheometer tooling comprised of a porous hydrogel in Chapter 5. The tooling allows additives to be dosed through a rheometer plate or cone, and the consequent effect of these additives on a material's mechanical response measured. We demonstrated that the tooling can be used to study the kinetics of material property variation due to the diffusion of molecular additives into the soft material though the hydrogel plate.

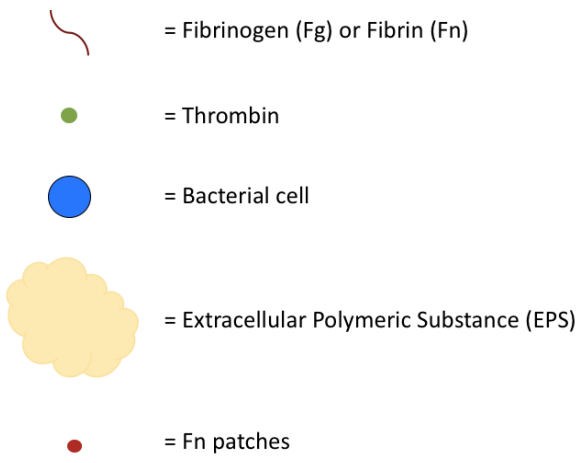

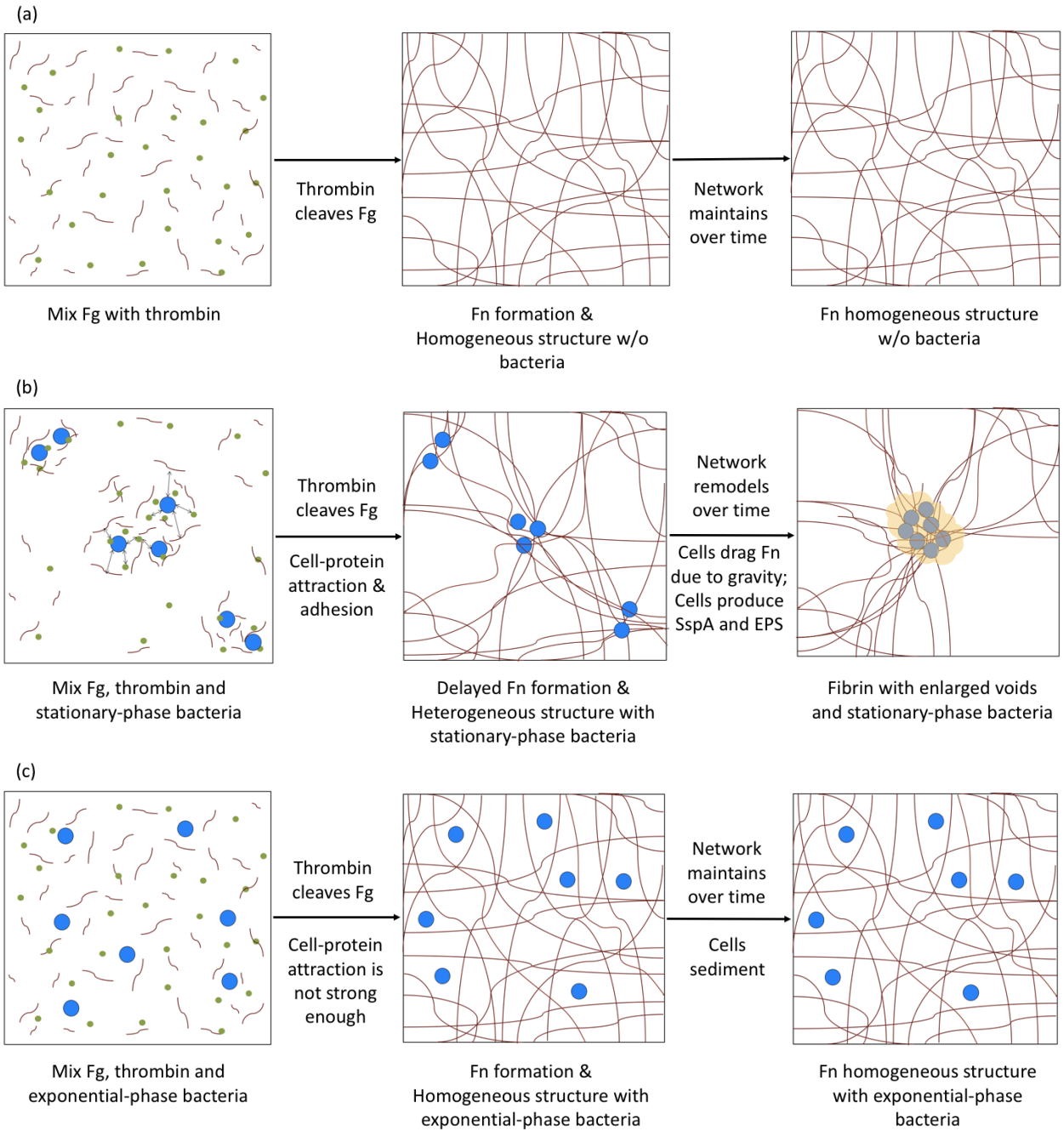
(a)
Thrombin cleaves Fg
Network maintains over time
Mix Fg with thrombin
Fn formation & Homogeneous structure w/o bacteria
Fn homogeneous structure w/o bacteria
(b)
Thrombin cleaves Fg
Cell-protein attraction & adhesion
Network remodels over time
Cells drag Fn due to gravity; Cells produce SspA and EPS
Mix Fg, thrombin and stationary-phase bacteria
Delayed Fn formation & Heterogeneous structure with stationary-phase bacteria
Fibrin with enlarged voids and stationary-phase bacteria
(c)
Thrombin cleaves Fg
Cell-protein attraction is not strong enough
Network maintains over time
Cells sediment
Mix Fg, thrombin and exponential-phase bacteria
Fn formation & Homogeneous structure with exponential-phase bacteria
Fn homogeneous structure with exponential-phase bacteria

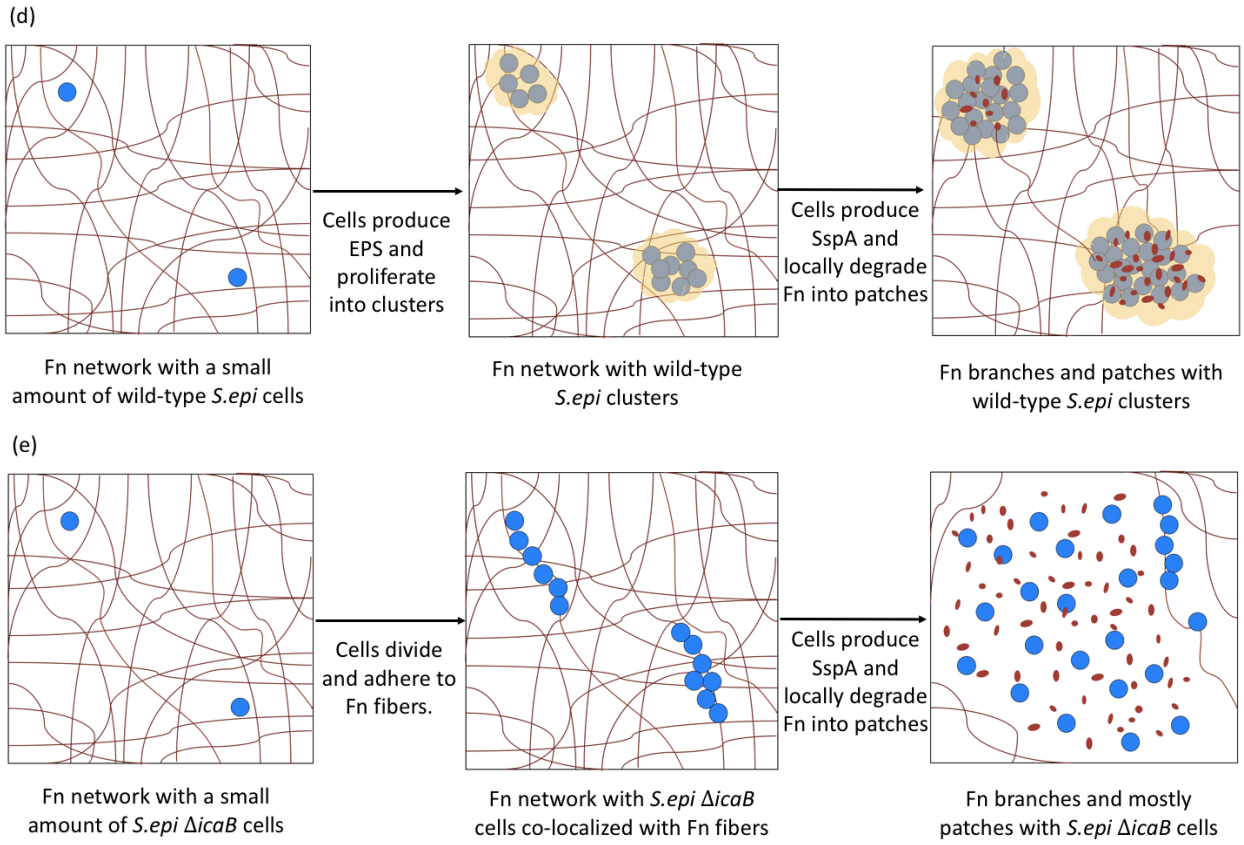

Figure 6-1 | Mechanistic sketches

Mechanistic sketches of (a) fibrin formation; (b) fibrin formation at the presence of exponential-phase bacterial cells; (c) fibrin formation at the presence of stationary-phase bacterial cells; (d) pre-assembled fibrin network with proliferating *S.epi* 1457 wild-type bacteria biofilms; (e) pre-assembled fibrin network with proliferating *S.epi* 1457 Δ*icaB* bacteria biofilms

Figure 6-11 summarizes the mechanism we propose that may lead to the observed phenomena in this dissertation. Once we mix thrombin into fibrinogen solution, thrombin cleaves fibrinogen and triggers the polymerization of fibrin. The presence of stationary-phase bacterial cells in this process introduces cell-protein attraction and adhesion which can arise from both specific and non-specific interactions as explained in the previous chapters. As described in chapter 2, the reduced fibrin formation kinetics can arise from the adhesion of thrombin to cell surfaces, which leads to a drop of thrombin concentration. Alternatively, fibrinogen adherence on cell surfaces

may also contribute to the delayed fibrin formation and the two step clotting process as shown in Figure 2-7: the first clotting step could be the polymerization of the less concentrated free-floating fibrinogen and the second clotting process happens presumably when the fibrin oligomer coated bacterial cells join the network. This may also explain that the bacterial cells, starting from free floating, adhere onto fibrin fibers over time.

The formation of a heterogeneous fibrin network can arise from the heterogeneous distribution of fibrinogen caused by cell-fibrinogen attraction. Alternatively, the large pore size population may be formed with the free-floating less concentrated fibrinogen and the small pore size population may be formed with the localized fibrin oligomers adhered on cell surfaces. The presence of exponential-phase bacterial cells does not generate a significant impact on fibrin structure nor mechanics. This indicates that there could be a threshold below which cell-protein attraction and adhesion may not always influence fibrin formation.

In the long term, we observed enlarged voids and increase structural heterogeneity in fibrin formed at the presence of stationary-phase bacterial cells. Mechanically, bacterial cells may apply a force on the fibrin network due to gravity. Chemically, bacteria may produce SspA that putatively degrade fibrin. This phenomenon does not apply to exponential-phase bacteria either because 1) not as many bacteria are adhered on fibrin fibers and 2) they do not produce SspA as much as stationary-phase cells as shown in Figure 3-3.

Figure 6-1 (d, e) explained the proposed mechanisms of the other scenario where bacteria are proliferating in a pre-assembled fibrin network. An *S.epidermidis* wild-type cell grows into a

biofilm cluster whose location depends on the initial bacterial cell location and is independent of fibrin fibers. The bacterial cells produce SspA that locally degrades fibrin around the cells. On the other hand, a $\Delta icaB$ cell,without de-acetylated PIA molecules attaching to its surface, divides into cells that are diffusive so that they have chances to bump into fibrin fibers. Once they bump into a fibrin fiber, they are likely to adhere to it due to its negative charges. Therefore, the $\Delta icaB$ cells co-localize with the fibrin fibers. Moreover, they express a higher amount of SspA (Figure 4-8). Both the co-localization and the increased expression of SspA contribute to the observed higher degree of fibrin degradation.

One of the questions encouraged by the study of fibrin formation at the presence of bacteria is the theoretical mechanisms that lead to the two step clotting process and the formation of the heterogeneous fibrin structure. In Figure 6-1 we propose some hypothesis that may be tested by mathematical simulations together with experimental characterizations of the involved forces. Another question this study inspires is the general relationship between fibrin structural and fibrin mechanical properties. In chapter 2, we propose a mathematical model that associate the heterogeneous fibrin structure to the different fibrin stiffness. Alternative explanations may also stand. For example, the additional mass of bacteria and the change in fibrin fiber bundles by the cells may both have a contribution to the change in the mechanical properties of an infected fibrin network.

In the future, we would also like to expand the study of infected fibrin to a more physiological conditions. An example would be an infected whole blood clot in a flow. An experimental model we would like to propose is to have a whole blood clot, infected or not, attached to a microfluidic

device that allows flows and the collection and size measurement of potential emboli. With this model, we may study how embolic events could be influenced by the presence of bacteria, flow rate, types of flow, etc. Potential limitations of this model may include the control of blood clot sizes and the attachment of clots to device wall.

Overall, this dissertation has contributed to the understanding of medical device infections and infection-induced thromboembolism. It opens up discussion of the interaction mechanisms between bacteria and embolism with potential implications for treating septic thromboembolism. The infected clot model could also be used to study other situations – such as chronic wound healing and scar formation – in which bacteria and clot co-present in the human body.